MATHEMATICAL MODELING OF ELECTRON BEAM COLD HEARTH CASTING OF TITANIUM ALLOY INGOTS

by

XUANHE ZHAO

B.Eng., Tianjin University, Tianjin, China, 2003

A THESIS SUBMITTED IN PARTIAL FULFILLMENT OF THE REQUIREMENTS FOR THE DEGREE OF

MASTER OF APPLIED SCIENCE

in

THE FACULTY OF GRADUATE STUDIES
(Metals and Materials Engineering)

THE UNIVERSITY OF BRITISH COLUMBIA

July 2006

ABSTRACT

The electron beam cold hearth remelting (EBCHR) process is used extensively for the refining of titanium alloys and casting of ingots. The main challenges associated with the final phase of the casting process are the formation of macroscopic shrinkage voids and evaporative losses of alloying elements in the top portion of the ingots. The purpose of the current work is to better understand the casting process and to give a theoretical foundation for addressing the issues of shrinkage void formation and evaporative losses.

To this end, a mathematical model has been developed to describe the EBCHR casting of a Ti-6Al-4V ingot. The model characterizes the mass, momentum, and heat transports together with their interactions, by solving the coupled thermal-fluid flow fields inside the ingot. The formation of shrinkage voids is predicted using the Niyama criterion calculated with the results of the model. Industrial experiments have been conducted to provide data for formulation of the model's boundary conditions and validation of its predictions. An overall heat balance analysis has been conducted on the domain used in the model at steady state. The results indicate that the primary energy input to the ingot is from the enthalpy of the inlet titanium, which accounts for approximately 65% of the total heat. The electron beams account for the balance or approximately 35%. The major energy losses from the domain are from the bottom and from the top surface, 24% and 31% respectively, and the mould, 29%, with the balance lost to the below mould environment, 16%.

The model has also been used to examine the effects of ramping the casting speed near the end of the casting process and adjusting the beam power and pattern during the final stage of casting. Casting speed appears to be effective in raising the

location of the final void, and thus may be effective in reducing size of the cropped prior to rolling. The latter appears to be effective in reducing the surface area of the liquid pool during the final solidification and therefore may be useful in reducing the evaporation losses. Judicious use of the two in combination may yield an optimum termination strategy.

TABLE OF CONTENTS

LIST OF TABLES

LIST OF FIGURES

ACKNOWLEDGEMENTS

I would like to express my deep appreciation to Prof. S.L. Cockcroft and Dr. D. Maijer for their input and welcome advice. "The process of modeling is like building a card house". It is their directions that make me add each card properly, efficiently, and on a solid foundation. I would like to thank Dr. J. Zhu for the helpful discussions.

The research was done in collaboration with TIMET Corp. in Morgantown, Pennsylvania, USA. I would like to thank them for the experimental data they provided.

Mr. M. Di Ciano's help on inverse analysis of the experimental data is acknowledged. I also appreciate Mr. M. Lane's discussion on computational fluid dynamics.

Finally, I thank my parents and my wife for their constant love and support; words alone cannot fully express my heartfelt appreciation for the active role they played and continue to play in my life.

CHAPTER 1. INTRODUCTION

1.1. Titanium Alloys and Their Applications

Titanium was discovered in 1790 but not purified until the early 1900s [1]. As a chemical species, titanium is very abundant. It is the fourth most prevalent metallic element in the earth's crust (exceeded only by Al, Fe, and Mg). Some of the basic characteristics of titanium are listed in Table 1.1 together with those of some other common structural metallic materials - Fe, Ni, and Al [2]. In general, the strength of titanium and its alloys is comparable to that of Fe-based and Ni-based alloys and is significantly higher than aluminum-based alloys. In terms of density, titanium and its alloys are approximately 50% less dense than Fe- and Ni-based alloys however it is approximately 50% denser than aluminum alloys [3]. From the stand-point of corrosion, it offers perhaps the best corrosion resistance in comparison to Al-, Fe- and Ni-based alloys [3]. The one downfall that has significantly limited extensive commercialization is cost. However, despite its relatively high cost, the advantages offered by titanium over competing materials has led to it its extensive use in several industries including aerospace, chemical processing and sporting goods. It is also used extensively as armor in military applications.

1.2. Titanium Sponge Production

In its most basic purified form, metallic titanium is called sponge because it is porous and has a sponge-like appearance - refer to Figure 1.1. The starting ore for the production of titanium is either rutile (TiO_2) or ilmenite ($FeTiO_3$). The extraction of metallic titanium from these ores occurs via the following five stages or operations [2]:

1. Chlorination of the ore to produce $TiCl_4$. The basic chlorination reactions are as follows:

$$TiO_2 + 2Cl_2 + C \rightarrow TiCl_4 + CO_2 \quad (1.1)$$

$$TiO_2 + 2Cl_2 + 2C \rightarrow TiCl_4 + 2CO \quad (1.2)$$

2. Distillation of the $TiCl_4$ to purify it.
3. Reduction of the $TiCl_4$ to produce metallic titanium. This process is referred to as the Kroll process and involves the reaction (reduction) of purified $TiCl_4$ with metallic Mg in two steps as follows:

$$TiCl_4 + 2Mg \rightarrow TiCl_2 + 2MgCl_2 \quad (1.3)$$

$$TiCl_2 + Mg \rightarrow Ti + MgCl_2 \quad (1.4)$$

4. Purification of the metallic titanium (the sponge) to remove by-products (Mg, $MgCl_2$ et al) of the reduction process.
5. Crushing and sizing of the metallic titanium to create a suitable product for subsequent consolidation processes (melting, alloying if appropriate and casting).

1.3. Melting (Consolidation) Technology for Titanium Production

Following the Kroll process it is necessary to melt the sponge and cast it in order to consolidate it into a primary ingot prior to further downstream processing. Alloying, if necessary, may also be completed during the primary consolidation process.

Molten titanium is very reactive requiring special techniques to produce ingots of both commercial purity (CP) titanium and the various titanium alloys. There are two commonly used melting processes: vacuum arc remelting (VAR) and cold hearth melting (CHM) using either electron beam or gas plasma as the heat source.

1.3.1. The Vacuum Arc Remelting Process

Vacuum arc remelting (VAR) is the most commonly used process for consolidating titanium. In preparation for the VAR process, titanium sponge and the required alloy elements are blended together and mechanically compacted at room temperature into blocks. The compacted blocks are welded together in an inert gas

chamber to create a first melt electrode or "stick". The stick is then melted in a VAR furnace to produce an ingot of slightly larger diameter. The ingot is then inverted and remelted using a larger ingot crucible to form a larger ingot. Titanium for use in rotary components (rotor grade) is typically triple melted so the ingot is once again inverted and remelted a third time.

The VAR process is reported to offer superior microstructure and chemical homogeneity over the cold hearth remelting processes and hence is the preferred route for producing high quality ingots such as rotor grade material for aerospace engine applications[2]. Unfortunately, it is not suitable for consolidation of scrap feedstock, which because of the high cost and limited supply of titanium sponge and limited supply, is an important source of titanium metal. One issue stems from the inability of the process to handle high density/high melting point inclusions such as tool-bit chips from machining process scrap.

1.3.2. Cold Hearth Remelting Processes

As previously described there are two types of cold hearth melting processes in use today. In the plasma arc remelting process, one or more plasma torches are used as the heat source to melt the feedstock, which may be in the form of compacted, or non-compacted, sponge or scrap. Once molten the liquid metal is then cast into primary ingots, either as rounds or slabs. The melting and casting processes are carried out under a reduced pressure argon atmosphere to avoid oxidation of the titanium.

The other cold hearth remelting process is the Electron Beam Cold Hearth Remelting (EBCHR) process. In this process, one or more high powered electron beam guns are used to heat and melt the feedstock. As in the case of the plasma-based process, a variety of feedstocks can be accommodated including consolidated or

non-consolidated sponge and scrap. Once molten the liquid metal is cast into either rounds or slabs depending on the application. In contrast to the plasma based process, the EBCHR process operates under a vacuum, which is a requirement of the electron beam gun. (This also serves to avoid oxidation of the titanium.)

Both of the cold hearth consolidation processes can remove high density inclusions and hence can treat scrap. The EBCHR process is reported to be superior to the plasma-based process in terms of its ability to also handle low density inclusions such as oxides and nitrides present in scrap from machining/cutting operations. In the case of the production of rotating quality material, ingots produced via either of the cold hearth consolidation methods require subsequent VAR processing in order to ensure chemical and microstructural homogeneity.

As the current research is focused on the EBCHR process, the rest of the introduction and much of the literature review will focus on it.

1.3.3. The EBCHR Process

A schematic of the electron beam cold hearth remelting process is shown in Figure 1.2. In the EBCHR process, titanium sponge and scrap are introduced into a furnace where they are melted by passing an electron beam over them. The molten titanium, while continuing to receive energy from an electron beam, then flows over a water-cooled copper hearth. A layer of solid titanium, called the "skull", forms in contact with the hearth, such that the molten titanium only contacts the solid titanium.

In the cold hearth, the high density inclusions sink to the bottom of the liquid pool and are then trapped in the skull, removing them from the ingot. The low density inclusions float to the surface of the liquid pool and are volatilized by a combination of the high energy density of the electron beam and the presence of the vacuum environment.

The molten titanium finally flows into a water-cooled copper mould, where it is partially solidified and an ingot is withdrawn. In the figure shown, the ingot is rectangular, but as previously described round shapes can also be directly cast. The casting process is semi-continuous owing to the need to maintain a vacuum environment within the casting section. Consequently, the process exhibits three distinct phases of operation: 1) start-up; 2) steady state operation; and 3) final transient stage. The length of the cast depends on customer requirements with the maximum size limited by the casting infrastructure – i.e. the length of the vacuum chamber.

In comparison to the VAR process, the EBCHR method has several advantages for titanium ingot production. The advantages of EBCHR result from the presence of a high vacuum, a relatively large amount of molten titanium at a reasonably high temperature, and the ability to separately conduct the purification and solidification processes. The potential advantages of EBCHR process are described as follows [2]:

1. It permits the residence time of the titanium in the molten state to be controlled independently of the volume of molten metal solidifying. In principle, this creates the opportunity for refining the alloys through dissolution of any nitrogen or oxygen rich defects without incurring a large, deep molten pool as would be the case in the VAR process (the deep liquid pool results in solidification conditions conducive to excessive solute segregation).
2. It permits gravity separation of high density inclusions such as tungsten-carbide tool bits or tungsten welding electrode tips that are introduced along with the revert (scrap). The high density inclusions become trapped in the mushy zone of the skull and are not transferred to the ingot. This is in complete contrast to the VAR process, where all the material in the electrode ends up in the ingot.

3. It allows direct casting of non-axisymmetric shapes, such as slabs and bars. These cast products are much better suited for conversion to flat mill products (plate, sheet, and strip) than large round ingots. Consequently, the conversion losses are lower and products made this way can be more cost competitive.
4. In contrast to the physical environment in the VAR furnace chamber, the cold hearth furnace is more conductive to the use of online sensors. Consequently, this process is more amenable to real-time process control and detection of process variations during the melting process.

Despite these advantages there are a number of challenges that remain before the EBCHR process can fully replace the VAR process. A few of them have been highlighted below:

1. The EBCHR is conducted in a high vacuum, and the depth of the melt pool in the cold hearth is typically very shallow (i.e., of the order of 25mm for titanium alloys [4, 5]). This can lead to excessive reduction in the content of low melting-point, high vapor-pressure elements, such as aluminum and chromium from the molten titanium alloy. Thus, it can be a challenge to control the chemical composition of the final product ingot.
2. The elements evaporated in the EBCHR process generally condense inside the vacuum chamber. If the condensation drops back to the liquid pool of the ingot, it may cause a "drop-in" defect inside the ingot. The Al-rich "drop-in" defects have been observed in ingots produced via EBCHR
3. The liquid mixing inside the ingot of EBCHR is generally inferior to VAR process. The poor mixing results in a lack of chemical homogeneity in the final ingot produced via EBCHR.

Another challenge associated with the operation of the EBCHR process relates to

the final stages of the casting process, which is the subject of this thesis. Because, the density of titanium increases ~3%, as it transitions from liquid to solid [6], there is an opportunity for macroscopic void formation if there is inadequate feeding during the last stages of the casting process.

In the EBCHR furnace currently used at TIMET's Morgantown Pennsylvania operation, electron beam energy continues to be added after the feeding has been terminated at the end of the casting process in order to reduce the formation of shrinkage voids. This method is not 100% successful in eliminating shrinkage voids and the ingot is cropped (a section is removed from the top) representing a loss in productivity. In addition, the extra energy input in this method also potentially causes excessive evaporation of alloy elements, varying the chemical composition of the final ingot. To this end, an optimization strategy which balances void reduction with evaporative losses is needed.

In order to better understand the EBCHR process, and to give a theoretical foundation for its optimization, a mathematical model has been developed to describe both steady state operation and the final transient stage of the process. Once validated, the model can be used to examine different scenarios for optimizing the process from the standpoint of void formation and chemistry control during the final transient stage of the process.

Table 1.1 - Some important characteristics of titanium and titanium alloys as compared to other structural metallic materials based on Fe, Ni, and Al [2]

	Ti	Fe	Ni	Al
Melting Temperature (°C)	1670	1538	1455	660
Allotropic Transformation (°C)	$\beta \xrightarrow{882} \alpha$	$\gamma \xrightarrow{912} \alpha$	-	-
Crystal Structure	bcc → hex	fcc → bcc	fcc	fcc
Young's Modulus E (GPa)	115	215	200	72
Yield Stress Level (MPa)	1000	1000	1000	500
Density (kg m^{-3})	4500	7900	8900	2700
Comparative Corrosion Resistance	Very High	Low	Medium	High
Comparative Reactivity with Oxygen	Very High	Low	Low	High
Comparative Price of Metal	Very High	Low	High	Medium

Figure 1.1 - Photo showing titanium sponge.

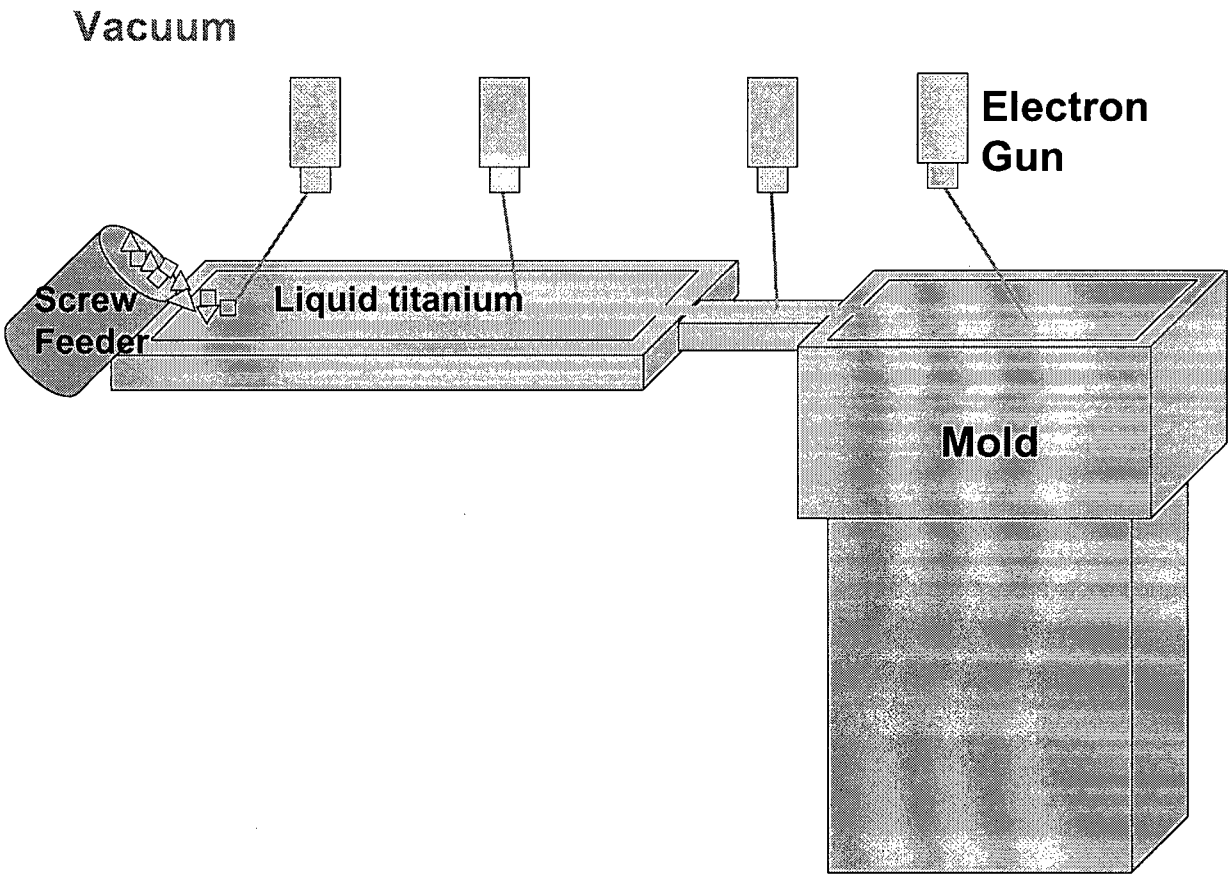

Figure 1.2 - Schematic plot of the EBCHR process.

CHAPTER 2. LITERATURE REVIEW

The EBCHR furnace may be described as two process units connected in series. Process 1 – the hearth - is responsible for the melting and refining operation (removal of low and high density inclusions). Process 2 – the mould/caster - is responsible for the removal of heat and the solidification operation. The power input to the two can be controlled independently; however there is a link between the melting rate and the casting rate. Previous investigators[7] have identified the challenges associated with conducting experimentally-based studies on production EBCHR casters. Factors such as the high temperature, the high solubility of most metals in liquid titanium, the vacuum environment, depth of the liquid pool, and non-transparency of the melt all contribute to making direct measurements difficult. When combined with the potential loss in productivity associated with conducting trial-and-error experiments on production furnaces, there is a significant advantage to be gained by using computer-based tools to examine the effect of parameter changes on process conditions. As a result, a significant amount of the research appearing in the literature has been focused on the development of mathematical models. In general, studies on the EBCHR process have focused either on the hearth or ingot solidification owing to their separation in function.

2.1. Research on the Cold Hearth

The research on the cold hearth in the EBCHR process is generally focused on addressing two issues: (1) the removal of the high density inclusions (HDI) and low density inclusions (LDI), and (2) controlling chemistry changes caused by evaporation of low melting-point, high vapor-pressure alloying elements.

2.1.1. Removal of HDI and LDI

Early in the 1980s, Entrekin studied the removal of HDI by feeding tungsten

carbide tool bits into the cold hearth [8]. Ultrasonic and radiographic inspection showed that almost all the bits were trapped in the solidified skull in the cold hearth [8]. The ability of the EBCHR process to remove HDI was further demonstrated in several experiments using inclusions ranging in size from 0.5 in (13 mm) to 0.0075 in (0.2 mm) [9]. Herbertson [10] analyzed the relationships between HDI size, sink time and liquid metal residence time by simple physical considerations using Stoke's law. Jarrett [11] conducted experiments in a small-scale electron beam furnace to study the removal of both HDI and LDI. A model was developed to characterize the effectiveness of the removal processes [11]. Mitchell reviewed the removal of inclusions and the elimination of defects via different technologies, including the EBCHR process [12, 13]. He concluded that the EBCHR is presently the melting system of choice for the production of high-quality titanium alloys from melt stock that includes revert [13].

2.1.2. Evaporation of Elements

Isawa et al [14] studied aluminum evaporation behavior in titanium alloys in a 250 kW EBCHR furnace, and proposed five sites from which aluminum could evaporate:

(1) the feed stock,

(2) metal drops falling from the feed stock,

(3) the hearth pool,

(4) metal drops from the hearth, and

(5) the ingot

The hearth pool was found to be the main site for evaporation due to its large reaction area (surface area exposed to the vacuum) and the metal's relatively long

residence time [14]. Another notable result was that the yield of volatile elements increased with the rate of casting [14]. This agrees well with earlier propositions by Mitchell et al [15] and Tripp et al [16]. Nakamura et al [17] investigated the effect of the beam oscillation rate on aluminum and titanium evaporation from Ti-6Al-4V in the hearth of a 30 kW EB furnace. It was found that the evaporative loss of both Ti and Al could be suppressed by the increasing the beam oscillation rate to ~1.0Hz. They further proposed that the optimum beam oscillation rate could be considered to be in the range of 1.0-10.0 Hz. Ritchie et al [18-20] examined the relationship between the x-ray emissions and the chemical composition of the liquid surface, in order to study the evaporative losses during EBCHR.

Aluminum losses in the EBCHR process during production of Ti-6Al-4V have been modeled mathematically in a number of studies using the Langmuir equation [21-23], which assumes interface-reaction-controlled kinetics and that there is no reflection of the evaporating atoms back to the surfaces by collisions in the ambient atmosphere. The Langmuir equation is:

$$J_{Al} = X_{Al} P^0_{Al} \gamma_{Al} \sqrt{\frac{M_{Al}}{2\pi RT}} \qquad (2.1)$$

where J_{Al} is the weight flux of aluminum through the evaporating surface, X_{Al} is the mole fraction of aluminum, P^0_{Al} the vapor pressure of pure aluminum at absolute temperature T, γ_{Al} is the activity coefficient of aluminum in the liquid melt, M_{Al} is the molar mass of aluminum, and R is the gas constant. Fukumoto et al [24] and Ritchie et al [25]'s experiments confirmed that the evaporation of aluminum could be estimated by the Langmuir equation. Ivanchenko et al [26], Akhonin et al [27], and Semiatin et al [28] developed diffusion models for the prediction of melt losses during EBCHR of alpha/beta titanium alloys. The Langmuir equation was implemented in

their models through the boundary condition definitions [26-28].

J. Bellot et al [5] developed a three-dimensional model of the cold hearth in EBCHR process. The model considered the transport of momentum, heat, and solute, together with their interactions. Both the removal of HDI and LDI and the evaporation of aluminum were predicted using the model. The model results indicated that:

(1) The melt flow is conducted in a thin film of liquid representing on average only 15% - 20% of the total melt depth in the hearth.

(2) Particles whose density is very different from that of the liquid either settle rapidly or rise to the surface of the cold hearth. Particles with densities similar to the liquid (less than ±3%) remain in the liquid stream.

(3) An increase in the scanning frequency of the electron beam from 0.5 to 11 Hz resulted in a 10% decrease in the aluminum loss in the case of Ti-6Al-4V.

2.2. Research on Ingot Casting

Within EBCHR casting processes, heat is input to the top surface of the ingot via an electron beam pattern and through the sensible heat of the incoming metal during casting. Heat is transferred within the ingot via diffusion and advection in the liquid, via diffusion within the solid. Heat leaves the ingot from the surfaces of the casting via contact conduction and/or radiation depending on the surface in question and its location within the furnace. The existing body of work on mathematical modeling of ingot solidification in the EBCHR process can be divided into two groups: (1) diffusion only thermal models and (2) coupled thermal/fluid flow models that describe both the flow and temperature fields.

2.2.1. Thermal Models

Early work on describing the heat transfer in the ingot of an EBCHR process generally used the modified-parameter approach [29-32]. Fluid flow within the ingot

was approximated using an empirically increased thermal conductivity in the liquid to account for the enhanced transport of heat by advection. The degree to which the thermal conductivity was enhanced was determined via a trial-and-error process with comparing to experimental results. The modified-parameter models suffered from a number of shortcomings including:

(1) The incoming liquid is typically uniformly added to the top surface of the ingot. This deviates significantly from the real casting process, in which the liquid is poured into the mould on one side, thus the transport of heat associated with the inlet stream and its impact on process symmetry cannot be accurately described..

(2) The development of recirculating flows associated with buoyancy forces cannot be approximated.

(3) The evaporation rate is difficult to accurately predict in the absence of fluid flow because of concentration gradients that develop.

Thus, depending on the objectives of the study a thermal-only model can be inadequate to capture key process phenomena.

2.2.2. Coupled Thermal Fluid Models

Jardy et al [33] coupled the thermal and fluid flow fields in an ingot with a fixed molten pool. This approach requires an *apriori* knowledge of the shape of the sump and consequently is restricted in its ability to explore the full effect of changes to the process parameters. Lesnoj et al [7] developed a coupled thermal fluid flow model of an axisymetric ingot in the EBCHR process. The processes of heat-mass exchange and hydrodynamics associated with solidification of the ingot were dicussed. Shyy et al [34] incorporated turbulent flow into models of titanium alloy ingots produced in EBCHR. However, the necessity of including a turbulence model is questionable, due

to the low casting speeds as will be discussed in later chapters.

There has been no work focused on predicting void formation during the final stages of the EBCHR casting. The previous work is none-the-less helpful in providing data and describing the techniques needed to develop a model to predict void formation.

CHAPTER 3. SCOPE AND OBJECTIVES

3.1. Objectives of the Research Program

The purpose of the current research is to develop a coupled thermal-fluid model that describes ingot casting in the EBCHR process at TIMET's operation in Morgantown Pennsylvania. The model will be developed to describe Ti-6Al-4V alloy solidification during steady state operation and in the final transient stage. To the extent possible, the results from the mathematical model will be compared to industrial measurements in order to validate the assumptions made in its formulation. Using the model, various combinations of casting speed and power input (amount and distribution) will be explored in an attempt to optimize the final transient stage from the standpoint of minimizing the impact of void formation and alloy evaporation on production losses.

3.2. Scope of the Research Program

The mathematical model developed in the program is based on the commercial computational fluid dynamics (CFD) program ANSYS-CFX 10.0. The equations governing conservation of energy, mass and momentum have been solved in order to predict the thermal and fluid-flow fields during both steady state and final transient solidification. The model uses a fixed, single domain approach with material advection through the domain (when casting) and accounts for the power input to the top surface via the electron beam pattern, radiation losses from the top surface, conduction and radiation to the mould, and radiation to the walls of the furnace below the mould. The flow induced by the input pour stream has been included as has the effect of buoyancy due to the temperature-dependent density. The Darcy force term has been implemented in the model to approximate the resistance to flow within the semi-solid interdendritic region. The latent heat of solidification and the β/α transition

have also been accounted for while solving the energy equation.

A sensitivity analysis was conducted using the model including both model control/formulation parameters and process parameters. The effects of different process parameters on ingot sump depth have been examined. The model has been validated against the top surface temperature distribution, which has been estimated using an optical method, against thermocouple data obtained from the top surface of the ingot during cooling, against the sump profile that has been delineated using a variety of tracers added to the liquid metal, and finally against the distribution of voids found in the top portion of an ingot. The final phase of the research work focused on the development of an optimization strategy in order to minimize void formation while at the same time avoiding excessive loss of aluminum.

CHAPTER 4. INDUSTRIAL MEASUREMENTS

As discussed in the previous chapter, the objective of this program is to develop a coupled thermal-fluid flow model of ingots produced in the EBCHR process. Industrial measurements from an EBCHR furnace are essential in the development of the model for two reasons: (1) to provide data to help formulate key process boundary conditions and (2) to provide data against which the model can be validated. For this purpose, industrial trials were conducted by TIMET Corp. at their Morgantown, Pennsylvania operations.

4.1. Experimental Program for Boundary Condition Characterization

In the EBCHR process, the liquid titanium is poured into a water-cooled copper mould and is continuously withdrawn from the bottom of the mould. Sufficient heat is extracted from within the mould via a combination of contact conduction and radiation to produce a solid shell capable of withstanding the metallostatic pressure. Below the mould the ingot passes through a gating/air lock system into a water-cooled canister (the 'can') which is also under a vacuum (at the end of a typical casting, after the ingot has cooled sufficiently, the gate between the furnace and the 'can' is closed allowing the 'can' to be opened to the atmosphere to facilitate removal of the ingot without interrupting the melting process). After the ingot passes through the mould, it is further cooled by radiation to both the air lock hardware and the 'can' walls. In addition, the top surface of the ingot also experiences heat loss via radiation to the walls of the furnace which are water cooled.

To aid in the tasks of understanding the heat transfer conditions governing this process and for formulating boundary conditions for the model, a variety of measurements have been made on the industrial process.

4.1.1. Mould Temperature Measurements

The copper mould used in the EBCHR process is cooled by water flowing through pipes within the mould wall. The water pipes are configured such that their axes are parallel to the casting direction, as shown in Figure 4.1 (a). Thermocouples were embedded in the mould at different heights in a region between two pipes, as shown in Figure 4.1 (b) and (c). The data from the thermocouples was analyzed using an inverse technique in order to estimate the temperature at the surface of the mould. This information has been used in formulating the in-mould boundary conditions, which are presented latter in section 5.8.

4.1.2. Chamber Wall Temperature Measurements

Below the mould, thermocouples were attached to the chamber walls facing both the narrow and rolling faces of the ingot. Figure 4.2 shows schematically where the thermocouples were placed in relation to the mould. Because of the limited domain size used in model formulation (refer to section 5.5), it was necessary to characterize the wall temperature distribution to a distance of only 1.5 m below the top surface of the ingot.

4.2. Experimental Measurements for Model Validation

The predictions of the ingot model have been validated in four ways: (1) by comparison to the temperature distribution on the top surface of the ingot, (2) by comparison to temperature measurements on the top surface of the ingot taken with a thermocouple during cooling; (3) by comparison to the sump depth of the ingot under steady state casting conditions, and (4) by comparison of the position of shrinkage voids formed in top of the ingot during the final transient stage of solidification.

4.2.1. Temperature Distribution on Ingot Top Surface

All physical objects at temperatures above absolute zero emit a characteristic electromagnetic radiation spectrum, which is dependent on the temperature of the

material [35, 36]. Hence, the radiation spectrum of a body can be used to determine its temperature providing sufficient information is available on the radiation characteristics of the material.

At TIMET's Morgantown facility, a video camera, mounted to a viewport on the furnace, is used to capture images of the top surface of the ingot throughout the casting process. The camera is a CIDTEC 3710D Monochrome Video Camera produced by Thermo Electron Corporation. The optics used to acquire the image consist of a neutral density filter, a near infrared filter (800-1100 nanometers), leaded glass, Suprasil (a type of Pyrex) glass, and a fixed focal length lens. A video-cassette recorder (VCR) is used to record the images of the ingot's top surface with a frequency of 24 frames per second. Because the radiation characteristics of liquid Ti-6Al-4V are not fully known and the transmission characteristics of the viewport optics are not known, the image obtained with the camera cannot be used to quantitatively determine the top surface temperature distribution. However, the information contained within the image is suitable for qualitatively estimating the temperature distribution – i.e. identifying hot and cold zones on the ingot top surface.

Some example frames from the video are shown in Figure 4.3. The bright regions in the example frames (a line in Figure 4.3 (a) and an ellipse in Figure 4.3 (b)) are sections of the electron beam pattern that have just been traced. These areas appear this way because the electron beam immediately increases the temperature along the path by some increment above the nominal metal temperature. Thus, the information obtained from the camera can also be used to confirm the electron beam pattern applied to the top surface.

The video image frames have been processed using the following procedure to extract qualitative temperature information:

1. The images were cropped to remove the mould from the image and leave only the ingot top surface.
2. The brightness of each pixel on the cropped video image is transformed into a value of grayscale (intensity), in the range of 0 - 255, with the brighter (hotter) pixels corresponding to a higher grayscale value, as illustrated in Figure 4.4.
3. In industrial practice, the electron beam(s) scan over the ingot top in a repeating pattern which is programmed by the operator. In the furnace used in this study, the pattern has a period of ~1s, which corresponds to approximately 24 video frames. In order to avoid bias caused by the beam pattern intensity, an average value for 24 frames is calculated for the grayscale of each pixel. In this way, an average grayscale image is generated for the ingot top surface.
4. Each of the grayscales calculated in step 3 is assigned to a color to indicate its temperature and allow comparison to the color temperature contours generated by the model. The assignment is done such that the lower grayscale values (lower temperatures) are assigned cooler colors (blue) and the higher grayscale (higher temperatures) are assigned warmer colors or reds. Moreover, the grayscale values are in linear relationship with the colors. *Note: It is important to point out that no attempt was made to calibrate the camera grayscale to the temperature and hence the colors do not represent absolute temperatures only differences in temperature.*

For the purpose of validation of the model, the temperature distribution on the top surface was captured using the video camera during both steady state operation and during the transient termination stage of the casting process.

4.2.2. Temperature Distribution at Discrete Locations on Ingot Top Surface

In order to quantitatively validate the model, the absolute value of temperature

occurring during casting is needed. For this purpose, two thermocouples were brought into contact with the ingot's top surface, after it was fully solidified during the transient final stage of the casting process. The top surface locations where the thermocouples were placed are illustrated in Figure 4.5. Two different thermocouple configurations were used: 1) in the first test, the tip of thermocouple, thermocouple #1, was covered by a high temperature insulating sleeve to prevent electrical contact with the slab, which had previously been determined to be a source of noise in the signal recorded by the data acquisition equipment; 2) whereas in the second test, the tip of the thermocouple, thermocouple # 2, was bare wire and the data acquisition system was grounded to the furnace in order to reduce signal noise. In both cases, the time was referenced to the end of steady state casting and the start of the transient cool-down period.

4.2.3. Sump Depth and Profile at Steady State

In order to estimate the sump depth and sump profile (depth and profile of the liquid pool) various additions were made to an ingot at the end of steady state casting. To determine the depth of the liquid pool samples of tungsten were added. Tungsten was chosen because it has a higher density than Ti and has a limited solubility in Ti. Once added the tungsten samples sink through the liquid coming to rest within the mushy zone at a location with a solid fraction less than 1. Following solidification the ingot can be sectioned and examined to determine the location of the tungsten.

The liquid pool profile was marked by adding copper which is soluble in Ti but also tends to sink. Following solidification, the ingot was sectioned and the interior surface etched to determine the final position of the copper-rich Ti in the liquid pool and thus approximately delineate the sump profile.

4.2.4. Positions of Shrinkage Voids

As discussed in Chapter 1, shrinkage voids can form in the top portion of the ingot during the final stages of solidification. The ingot marked with tungsten and

copper additions was sectioned along the plane bisecting its narrow faces. The shrinkage voids were clearly visible without polishing or etching.

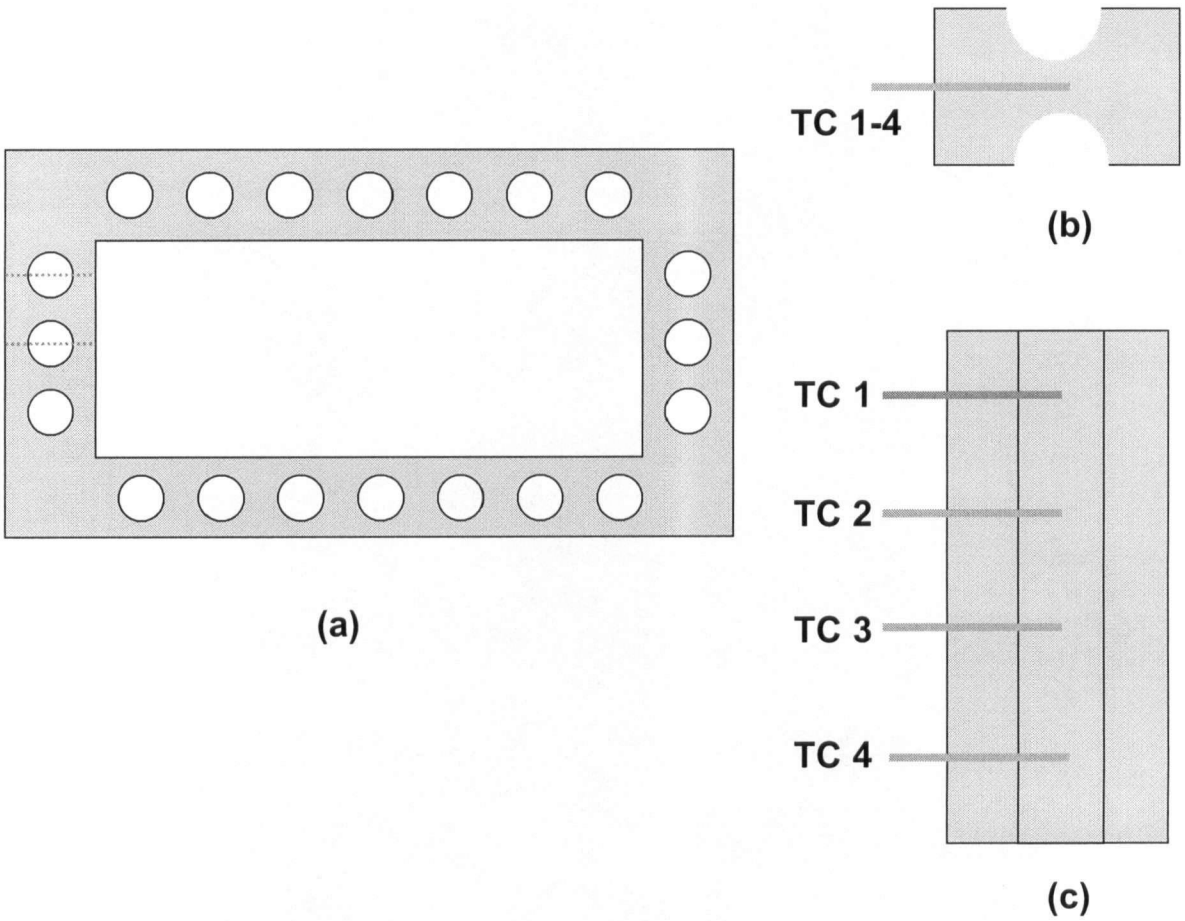

Figure 4.1 - Schematic plots of the water-cooled copper mould in the EBCHR process (a), and the locations of thermocouples embedded in the mould (b and c).

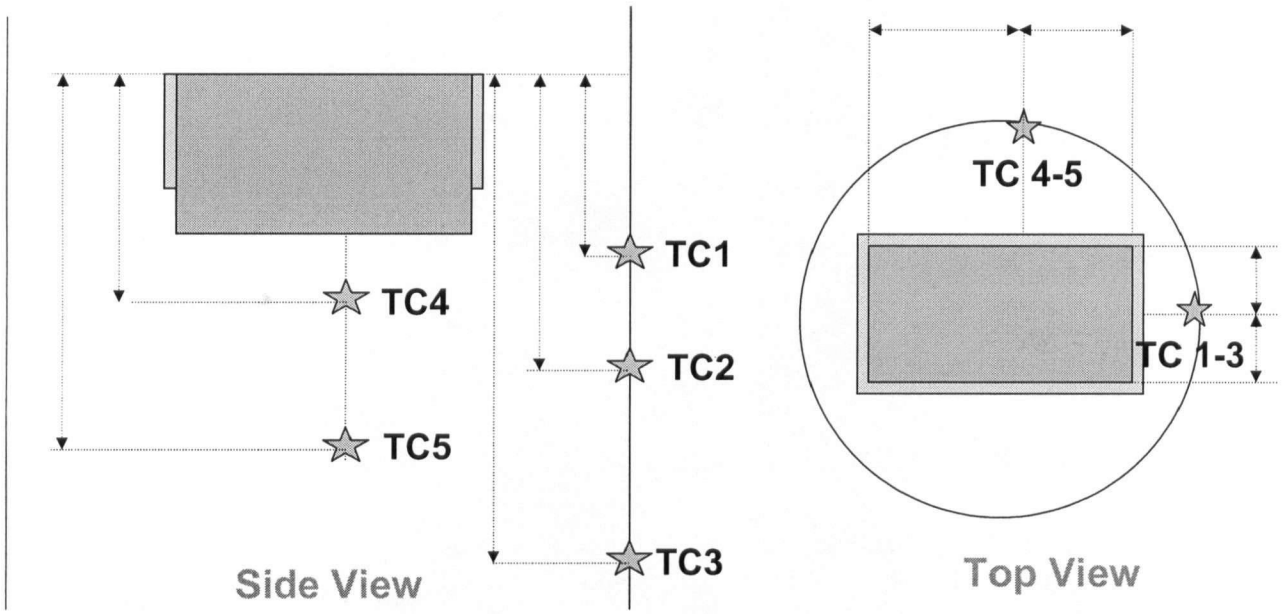

Figure 4.2 - Schematic plots of thermocouples attached to the chamber wall of the EBCHR facility.

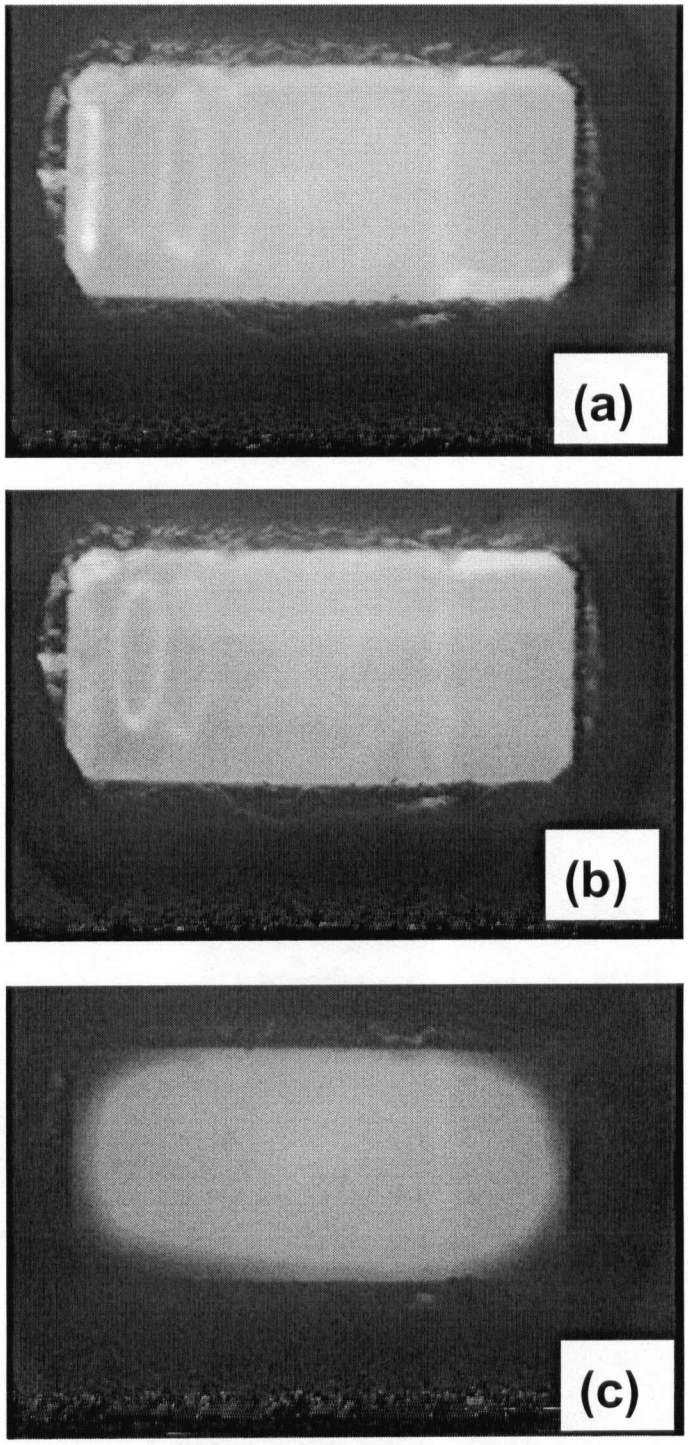

Figure 4.3 - Photos showing the top surface of an ingot during EBCHR.

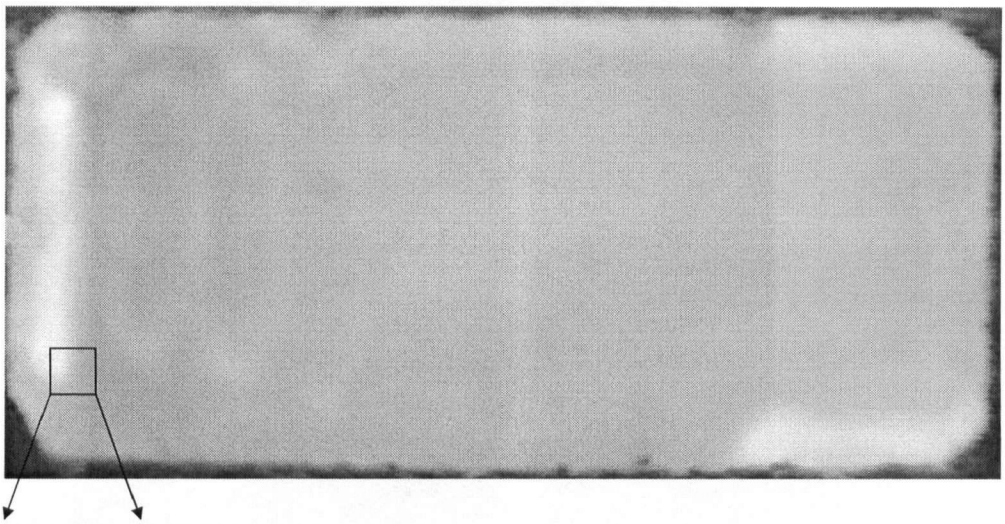

201	195	90	81
199	197	95	80
198	190	89	75
170	120	80	70

Figure 4.4 - Transforming the brightness of each pixel into grayscale.

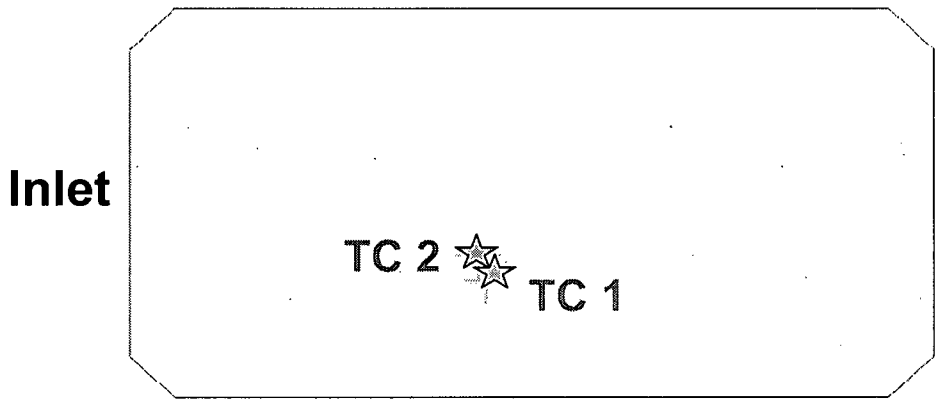

Figure 4.5 - Schematic plots of thermocouples locations on the top surface of the ingot.

CHAPTER 5. MATHEMATICAL MODEL DEVELOPMENT

As the objective of the model is to predict the location of void formation during the final transient stage of the casting process it is necessary that the evolving thermal field and in particular the progress of the solidification front (liquidus and solidus isotherms) be predicted with the model. To achieve this goal the model must be able to quantify the position of the liquidus and solidus isotherms at the end of steady state operation and then follow their evolution with time during the final transient stage of the casting process, ending with the ingot fully solidified. Thus, two models are required: the first to predict the steady state temperature distribution; and the second to predict the evolution of temperature in the ingot with time during the final transient stage of the casting process. The latter model will use the temperature distribution in the ingot at the end of steady state operation as an initial condition. Fluid flow was expected to play a significant role in determining the steady state temperature distribution. Consequently, a coupled thermal-fluid flow model was developed using the commercial software package ANSYS-CFX 10.0.

5.1. Governing Equations

The governing equations for the thermal-fluid flow model are based on conservation of mass, momentum, and energy.

Continuity Equation

The mass conservation equation in vector form is:

$$\frac{\partial \rho}{\partial t} + \nabla \cdot (\rho \mathbf{u}) = 0 \tag{5.1}$$

where ρ is the density, t is time, and $\mathbf{u}$ is the vector of fluid velocity.

Momentum Equation

The momentum equation in vector form is:

$$\rho(\frac{\partial \mathbf{u}}{\partial t} + \mathbf{u} \cdot \nabla \mathbf{u}) = -\nabla p + \nabla \cdot (\mu\ (\nabla \mathbf{u} + (\nabla \mathbf{u})^T)) + \rho_{ref}\, \mathbf{g} + \mathbf{S}_M \tag{5.2}$$

where p is the static pressure, μ is the dynamic viscosity, ρ_{ref} is the reference density which is taken to be the density of titanium in the solid state, **g** is gravitational acceleration, and $\mathbf{S}_M$ is the momentum source term. In the present problem, several momentum source terms have been defined and are described below in sections 5.2 and 5.3.

Energy Equation

The energy equation in vector form is:

$$\rho C_p(\frac{\partial T}{\partial t} + \mathbf{u} \cdot \nabla T) = \nabla \cdot (k \nabla T) \tag{5.3}$$

where T is the temperature, C_p is the specific heat, and k is the thermal conductivity.

These three equations (Eqs. (5.1) – (5.3)) are solved subject to the definition of initial and boundary conditions with the additional features described below included. *Note: in both the steady state and transient stage of the model the transient form of these equations was solved.*

5.2. Implementation of Buoyancy

As the density for liquid titanium is temperature dependent and there are significant temperature gradients present in the liquid pool, the effect of buoyancy was potentially important and was included in the model formulation. A source term to provide the effect of buoyancy was added to the momentum equation as follows:

$$\mathbf{S}_{M,buoy} = (\rho - \rho_{ref})\mathbf{g} \tag{5.4}$$

5.3. Implementation of Darcy Force

In order to limit the velocity of the solid to the ingot withdrawal rate and to include the resistance of porous flow through the interdendritic regions, a momentum

source term has been included in the momentum equation using Darcy's Law [37]:

$$\mathbf{S}_{\mathbf{M,Darcy}} = -\frac{\mu}{K}(\mathbf{u} - \mathbf{u}_{\mathbf{spe}}) \qquad (5.5)$$

where $\mathbf{u}_{\mathbf{spe}}$ is the specific velocity of the solid part or the ingot withdrawal rate when applicable, and K is the permeability of the mushy zone.

In the current model, the permeability has been calculated with the Kozeny-Carman equation[38]:

$$K = \frac{(1 - f_s)^3}{k s_0^2 f_s^{\,2}} \qquad (5.6)$$

where f_s is the fraction solid, s_0 is the solid/liquid interfacial area per unit volume of solid, and k is the Kozeny constant.

For simplicity, it is often assumed in numerical models of interdendritic liquid flow that k has a value of 5 and the s_0 remains constant [39]. The variation of permeability employed in the current model has been plot in Figure 5.1 as a function of fraction solid.

The momentum terms for buoyancy and Darcy forces are summed as follows and included in Eq. (5.2):

$$\mathbf{S}_{\mathbf{M}} = \mathbf{S}_{\mathbf{M,buoy}} + \mathbf{S}_{\mathbf{M,Darcy}} \qquad (5.7)$$

5.4. Implementation of Latent Heat

Latent heat is evolved during both solidification and the β to α solid state phase transformation which occurs in the Ti-6Al-4V alloy. The effective specific heat method was adopted in the present model where the specific heat is artificially increased to reflect the release of heat during the two phase transformations. Accordingly, the following two equations have been used [40]:

$$C_{p,eff} = C_p + C_{p,latent} \qquad (5.8)$$

where $C_{p,\,latent}$ is evaluated from the expression

$$C_{p,latent} = -L\frac{df}{dT} \tag{5.9}$$

During solidification, L is the corresponding latent heat released and f is the fraction solid. The same equation also characterizes the latent heat released during the β/α phase transformation where f is the fraction of α phase.

5.5. Calculation Domain – Steady State and Transient Stage Models

The final length of an ingot produced via the EBCHR process is typically ~10 m. For the purpose of computational efficiency, only a portion of the ingot was modeled using a fixed domain. The calculation domain used for the current 3-D thermal-fluid analysis, shown in Figure 5.2(a), is the top 1.524 m portion of the ingot. This length was selected by approximately doubling the liquid sump depth, which is typically approximately 0.8 m during steady state operation. A domain-length sensitivity assessment showed that a model with double the domain length (3.048 m) predicts the same temperature distribution in the top portion of the ingot. The ingot cross section is hexagonal (approximately rectangular with chamfered corners) with the dimensions indicated in Figure 5.2 (b).

In the steady state model, material is moved (advected) through this domain at a rate consistent with the casting speed. In the transient model, which is intended to describe the last stages of the casting process, material may or may not be moved through the domain dependent on whether ingot withdrawal is on-going at a reduced rate or has been suspended.

5.6. Finite Volume Mesh

The finite-volume mesh for the 3-D model, presented in Figure 5.3 (a), consists of two types of elements: eight-noded isoparametric brick elements and six-noded isoparametric prism elements. The elemental size used for generating the mesh for the

ingot ranges from a minimum of 0.010 m to maximum of 0.051 m in side length. A mesh sensitivity analysis has been conducted on the model by refining the mesh in the Z-direction, as shown in Figure 5.3 (b). The analysis showed that the predicted temperatures are not sensitive to mesh for the mesh resolution employed in the current study.

5.7. Materials Properties

The thermophysical properties of Ti-6Al-4V (Ti64) used in the model, based on the data published by Mills [6], are presented in Table 5.1.

The solidus and liquidus temperatures of Ti64 are 1940K and 1992K, respectively. The latent heats of solidification and the β/α phase transformation are 286000 J kg^{-1} and 48000 J kg^{-1}, respectively. Figures 5.4 and 5.5 show the evolution in fraction transformed with temperature, the evolution in rate of transformation with temperature, and the variation in $C_{p,\,latent}$ with temperature calculated according to Eq. (5.9) for the liquid-to-solid transformation and the β/α transformation, respectively.

The dynamic viscosity for liquid Ti64 is 0.003 Pa s. During the liquid to solid transformation, the dynamic viscosity of mushy Ti64 was ramped based on the increase of fraction solid to a maximum of 3 Pa s. The density below the solidus temperature was held constant to avoid altering the mass in the solid, since the volume of the computational domain does not vary with temperature.

5.8. Boundary and Initial Conditions

To mathematically describe the EBCHR casting process, the surface of the calculation domain has been divided into five regions which require the formulation of thermal and fluid flow boundary conditions. These are: 1) the inlet area, located on the top face, through which the liquid titanium is introduced into the domain; 2) the top surface of the ingot; 3) the ingot side wall within the mould; 4) the ingot side wall

below the mould; and 5) the bottom face of the domain.

Top Surface of the Domain -Inlet Area

The inlet condition is incorporated into the model as shown in Figure 5.2. The inlet area is assumed to be a square region with 0.0762 m sides. The inlet flow rate of liquid titanium can be varied. In the steady state model the inlet flow rate is set to TIMET's production flow rate. The inlet temperature and orientation of the momentum can also be specified. In the base case version of the model an inlet temperature of 2122 K, which is 130 K superheat, has been assumed based on discussions with TIMET personnel. In the actual process, the pour stream drops only a short distance (< 2.0cm), thus it is conceivable that the input stream retains some horizontal component of momentum. In an effort to include the horizontal momentum of the pour stream, the direction of the inlet flow steam is set to 10° from vertical.

Top Surface of the Domain – Electron Beam Pattern and Radiation

The top surface of the domain has several boundary conditions applied to it in order to describe the fluid flow and heat transport conditions present on the top surface of the ingot. In terms of fluid flow, the top surface (excluding the section defined as the inlet area) is treated as a free-slip wall in the model. Strictly speaking, there is a free surface between the liquid titanium and the vacuum environment in the chamber. However, the melt inlet flow rate is adjusted in order to maintain a near constant liquid surface level in the EBCHR process.

In terms of the heat transfer, electron beams from two guns input power to the ingot top surface in TIMET's furnace. The combined power (P_{EB}) applied during steady state operation is ~600 kW, assuming no losses.

The pattern traced with these guns is programmed into the gun pattern control

computer and is set to repeat with a period of approximately 1 s. An example gun pattern is shown on Figure 5.6 (a). The pattern consists of lines, ellipses, and circles which describe the path of the electron beams. The black dots on Figure 5.6 (a) represent the points on a hypothetical beam pattern where the beams dwell for a period of time – i.e. dwell time.

The pattern, which defines both location and dwell time is critical to determining the foot-print of power input to the process. As such, this information is proprietary to TIMET and has not been included in this thesis. However, this information has been used in development of the model.

Using the hypothetical beam pattern shown in Figure 5.6 (a) as an example, the power of electron beams is distributed across the top surface using a repeating pattern consisting of N points (impingement points). Defining the time for completion of a whole pattern as t_N, and the dwell time on the ith impingement point as t_i, the time-based power fraction for point *i* can be calculated as:

$$r_i = \frac{t_i}{t_N} \tag{5.10}$$

At the point where the beam spot dwells on the surface, it is assumed to impart its thermal energy with a Gaussian distribution with a standard deviation *s* [41, 42]. As there may be energy received at a point on the ingot surface from multiple overlapping beam spots, the heat flux at any point on ingot top surface from a single electron beam spot (or impingement point) is given as:

$$g(l_i) = f_{abs} \cdot P_{EB} \cdot r_i \frac{1}{s\sqrt{2\pi}} \exp\left(-\frac{l_i^2}{2s^2}\right) \tag{5.11}$$

where l_i is the distance from current location on the ingot surface to the beam spot and is given by

$$l_i = \sqrt{(x - x_i)^2 + (y - y_i)^2} \tag{5.12}$$

Note: this is the distance from any point on ingot surface (x, y) where the boundary condition is being evaluated (surface integration point) to the ith impingement point (x_i, y_i). At the beam impingement point, the kinetic energy of the electron beam is converted to thermal energy, with losses of 20-30% due to backscattering of the electrons [43]. In the current model, a factor of 0.7 has been chosen for Ti64's absorption of the electron beams - i.e. $f_{abs} = 0.7$.

For each location on the ingot top surface (surface integration point), the time-average heat flux q_{EB} (W m^{-2}) is calculated by summing the contribution of the *N* points from multiple electron beams using:

$$q_{EB} = f_{abs} \cdot P_{EB} \cdot \frac{1}{s\sqrt{2\pi}} \cdot \sum_{i=1}^{N} \frac{t_i}{t_N} \exp[-\frac{(x - x_i)^2 + (y - y_i)^2}{2s^2}] \tag{5.13}$$

In industrial practice, the electron beam pattern is developed by overlapping a series of standard paths such as ellipses, circles, or straight lines, as demonstrated in Figure 5.6 (a). An example of the resulting time averaged flux distribution employed in industry is shown in Figure 5.6 (b). The plot has been shown with normalized coordinate axes to avoid disclosure of TIMET intellectual property.

After the steady-state phase is complete, the electron beam may still scan over the ingot top surface for some time to avoid excess void formation. This process is referred industrially as a "hot top". The power and patterns of the electron beam in the "hot top" period are generally different from those employed during steady state operation. Hence, it is necessary to calculate a new time-averaged heat flux input for every beam pattern change in the process. The "hot top" heat flux distribution used in the model is shown in Figure 5.7. The total electron beam power input during "hot top" is 500 kW.

In addition to receiving heat from the electron beams, the top surface also looses heat via radiation to the furnace enclosure. In EBCHR modeling, the ingot, the roof and walls of vacuum chamber, and the copper mould are assumed to behave as gray bodies, whose emissivity are independent of temperature [5, 26]. The heat loss due to radiation from the liquid titanium surface to the furnace enclosure has been characterized using the following equation:

$$q_{rd} = \sigma\varepsilon(T_s^4 - T_{roof}^4) \tag{5.14}$$

in which ε is the effective emissivity, which is set equal to 0.4 [6], the Stefan-Boltzman constant σ is 5.670×10^{-8} $Wm^{-2}K^4$, and the furnace enclosure temperature T_{roof} is 773K. T_s is the ingot top surface temperature at the surface integration point being processed. In the context of the heat transfer analysis, the heat loss from the ingot due to evaporation is assumed to be negligible [26].

Side Surfaces of the Domain - Mould Cooling Region

The top 0.457 m of the domain is assumed to be within the water cooled copper mould, as shown on Figure 5.2. Within the mould, the heat flux from the sides of the ingot is calculated using the following relationship:

$$q_{mold} = h_{eff}(T_s - T_{mold}) \tag{5.15}$$

in which h_{eff} is the effective heat transfer coefficient and T_{mold} is the far-field or mould hot-face temperature.

The heat transfer coefficient associated with the mould cooling region has been varied as a function of ingot surface temperature to account for the varying transport mechanisms that exist within the mould [44]. At the meniscus, for $T_s > T_{liquids}$, h_{eff} is set equal to 1500 $Wm^{-2}K$ to reflect good contact conduction between the liquid metal of the casting and the mould. As the temperature drops and solidification occurs - e.g.

$T_{liquidus} > T_s > T_{solidus}$, h_{eff} is assumed to decrease linearly from 1500 to 1000 $Wm^{-2}K$, reflecting a gradual reduction in contact conduction associated with the formation of the as-cast surface. Once a solid skin has formed, the surface of the ingot separates from the mould wall (thereby forming a gap at the interface). Thus, over a small temperature range below the solidus - e.g. $T_{solidus} > T_s > T_{solidus} - 50K$, h_{eff} is assumed to decrease linearly from 1000 to 220 Wm^{-2} K. After the gap has formed ($T_s < T_{solidus} - 50K$), radiation heat transfer dominates, and h_{eff} is approximated as $\sigma\varepsilon(T_s^2 + T_{mold}^2)(T_s + T_{mold})$. The resulting variation in h_{eff} with temperature is shown plotted in Figure 5.8

The temperature at the mould surface, T_{mold}, has been estimated based on the temperatures obtained from within the mould using an inverse heat conduction analysis technique [45]. (The inverse analysis was conducted by Mr. Massimo Di Ciano, an M.A.Sc. Candidate at UBC.) The results from the inverse analysis (T_{mould}) are plotted together with the thermocouple temperature data in Figure 5.9. The temperatures from thermocouples are in the range of 40 - 70°C, while the temperature of the mould's inner surface ramps from ~350°C at the top of the mould to ~300°C at the bottom.

Side Surfaces of the Domain - Below-Mould Region

Below the mould, the side of the ingot is cooled via radiation to the side wall of the vacuum chamber. The boundary condition applied to the domain to approximate radiative heat loss in the below-mould region is:

$$q_{below} = \sigma\varepsilon(T_s^4 - T_{below}^4) \qquad (5.16)$$

in which T_{below} is the ambient temperature of chamber wall below the mould. The surface temperature of the region below the mould was measured using the procedure

described in section 4.1.2. A plot showing the variation in surface temperature with position below the mould is shown in Figure 5.10. Extrapolation of the thermocouple results indicates that: (1) Temperatures on the chamber wall below the mould are height dependent, and (2) at the same height, the wall facing the rolling face has a higher temperature than the one facing the narrow face. Without additional data to completely describe the variation of chamber wall temperatures and since the temperature differences between the rolling and narrow faces is comparatively small, the average value has been used as the effective ambient temperature below the mould.

Bottom Surface of the Domain - Outlet Face.

During casting conditions where ingot withdrawal is occurring, the solidified ingot moves out of the calculation domain through the bottom or outlet face. Under steady conditions, the outlet flow rate was set to balance the inlet flow rate. In the transient model, the outlet flow may be ramped down or set to zero depending on the conditions being examined.

The energy loss from the outlet face occurs in two ways: 1) through advection of hot material (enthalpy); and 2) through heat conduction to the lower extremities of the ingot that are cooler. The domain length sensitivity analysis mentioned earlier also showed that during steady state operation the energy loss due to heat conduction is negligible compared to the heat transferred by enthalpy transport (hot material advection). Therefore, in the steady state model the outlet face is assumed to be adiabatic with respect to conduction.

Because the withdrawal of the ingot is slowed or stopped in the last stages of the casting process the assumption of negligible conductive transport through the bottom

face of the domain may no longer be valid. Therefore, the heat conduction through the bottom face in the final transient-stage model was approximated as a heat flux given by

$$q_{bottom} = -k\frac{dT_{bottom}}{dz} \tag{5.17}$$

where $\frac{dT_{bottom}}{dz}$ is the temperature gradient normal to the bottom surface.

Initial conditions

As previously indicated both the 'steady-state' and final 'transient-stage' models are solved using the same set of basic equations which are formulated to solve a general set of transient problems. In the case of the steady state model, the model is initially assumed to have uniform thermal, velocity and pressure and fields, with T set equal to the temperature of inlet liquid, **u** set equal to 0 m s^{-1}, and p set equal to 0 Pa. The governing set of equations are then solved in time until the field variables cease to change (to within a tolerance) and a steady state condition is achieve. In the transient-stage model, the field variables output from the steady state solution is used as the initial condition. The governing equations are then solved in time in order to predict the evolution in the field variables that arise as a result of variations in both the casting speed (including setting it to zero) and electron beam power input and pattern.

Table 5.1 - Thermophysical properties of Ti-6Al-4V [6]

Temperature (K)	Density ($kg\ m^{-3}$)	Thermal Conductivity ($W\ m^{-1}\ K^{-1}$)	Specific Heat ($J\ kg^{-1}\ K^{-1}$)
2173	3750	34.6	831
2073	3818	34.6	831
1992(Liquidus)	3873	34.6	831
1940(Solidus)	4186	28.88	762.07
1923	4186	28.4	759
1873	4186	27	750
1773	4186	25.8	732
1673	4186	24.6	714
1573	4186	23.7	696
1473	4186	22.9	678
1373	4186	21	660
1278	4186	19.46	642.74
1268	4186	19.41	644.54
1173	4186	19.06	677.35
1073	4186	17.55	691.26
973	4186	15.47	684.03
873	4186	14.18	667.71

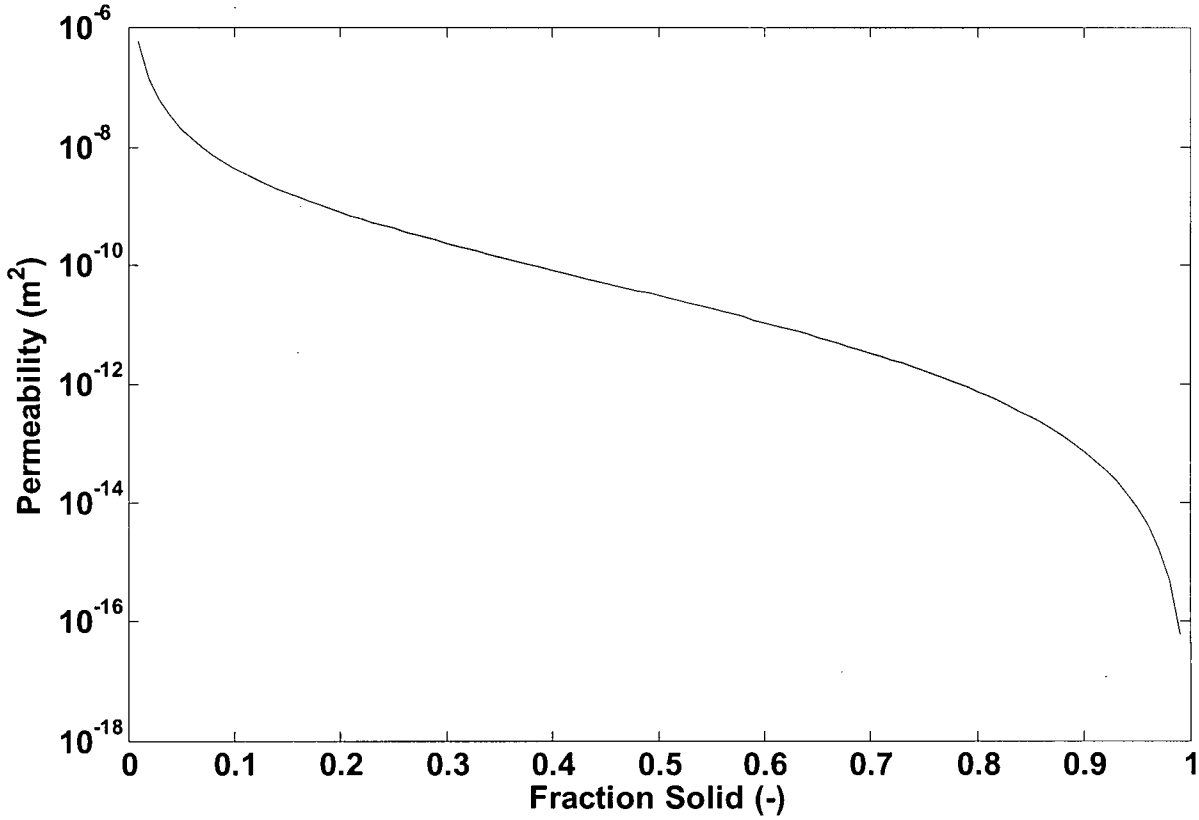

Figure 5.1 - Permeability as a function of fraction solid.

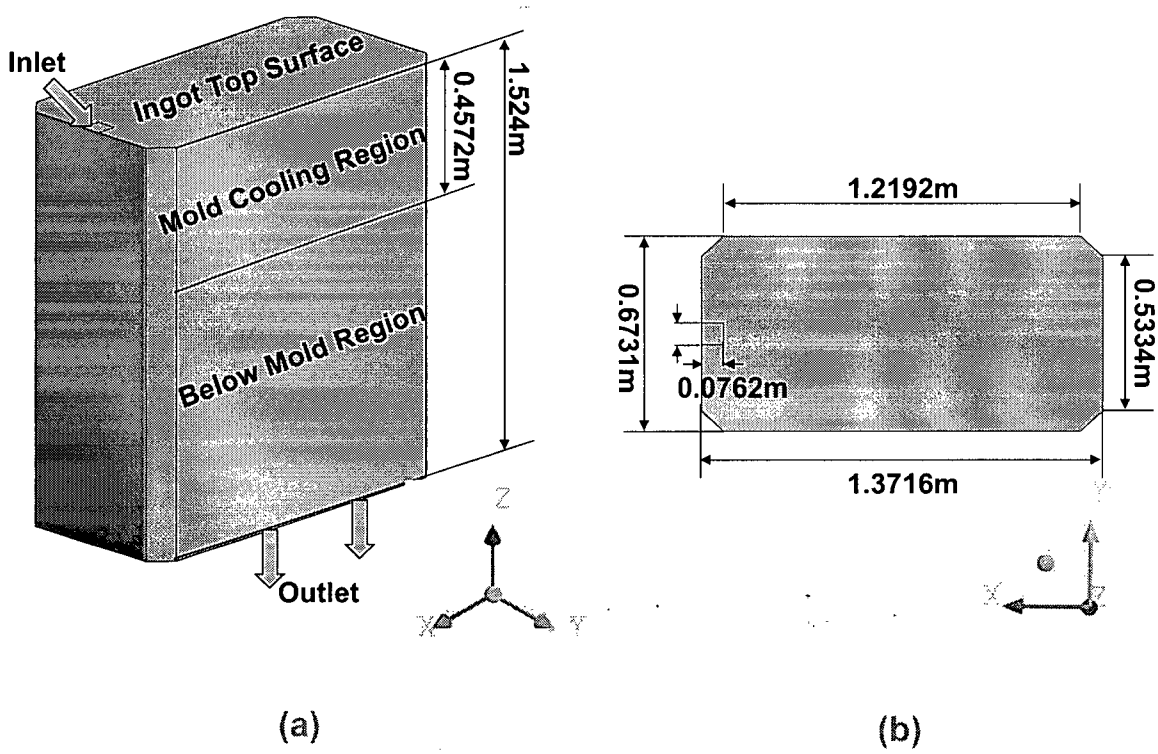

Figure 5.2 - Geometry of the ingot model in EBCHR. The various faces in the domain on which the boundary conditions are applied have also been indicated.

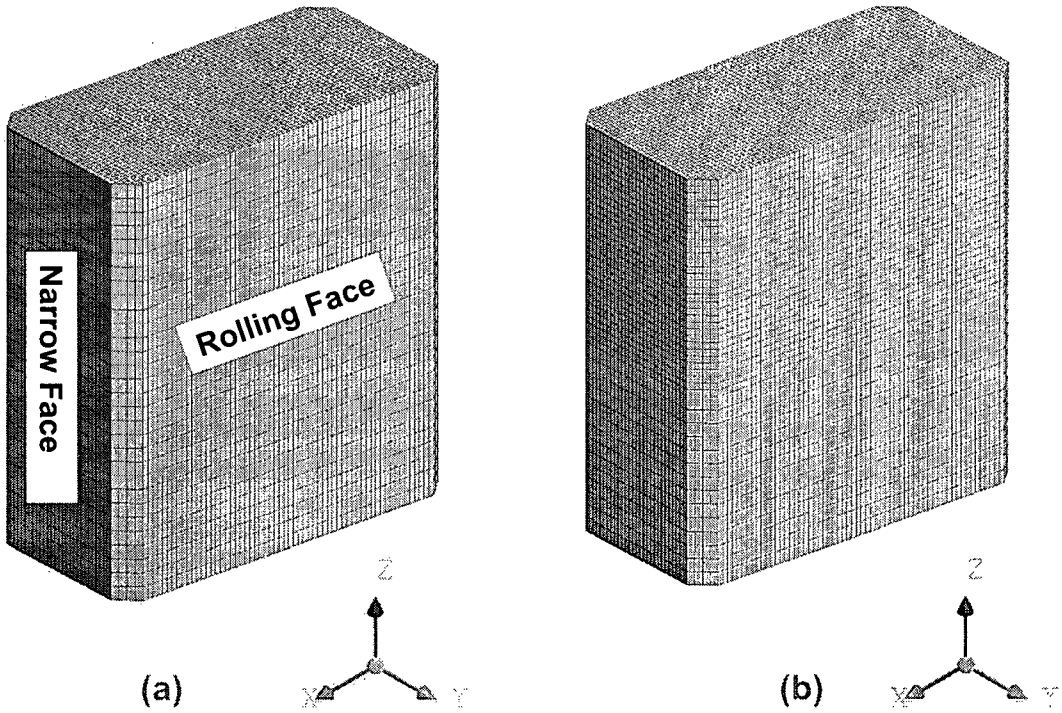

Figure 5.3 - The three-dimensional finite volume mesh for the ingot model: (a) the mesh of the ingot model and (b) a mesh refined in Z-direction for mesh-sensitivity analysis.

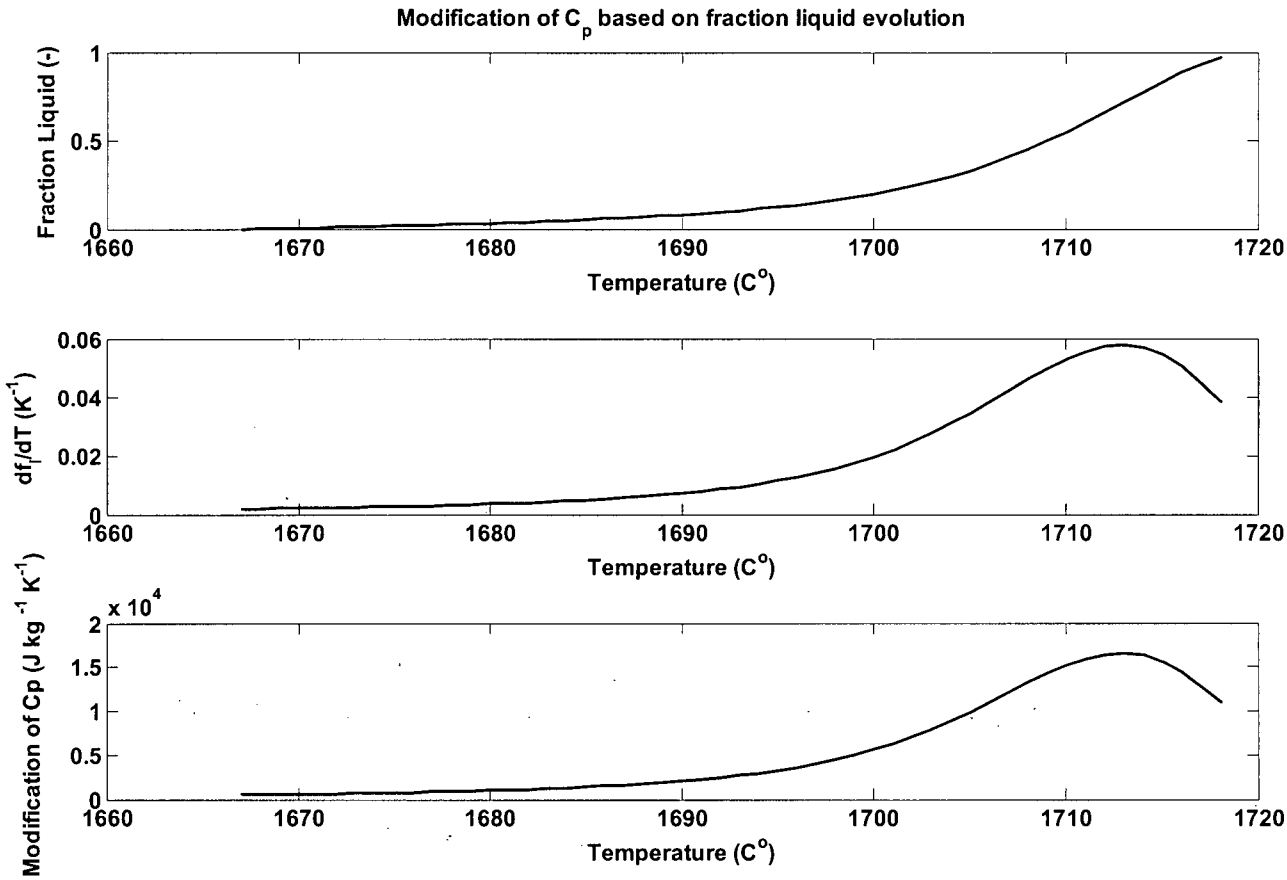

Figure 5.4 - Modification of the specific heat based on the fraction liquid evolution.

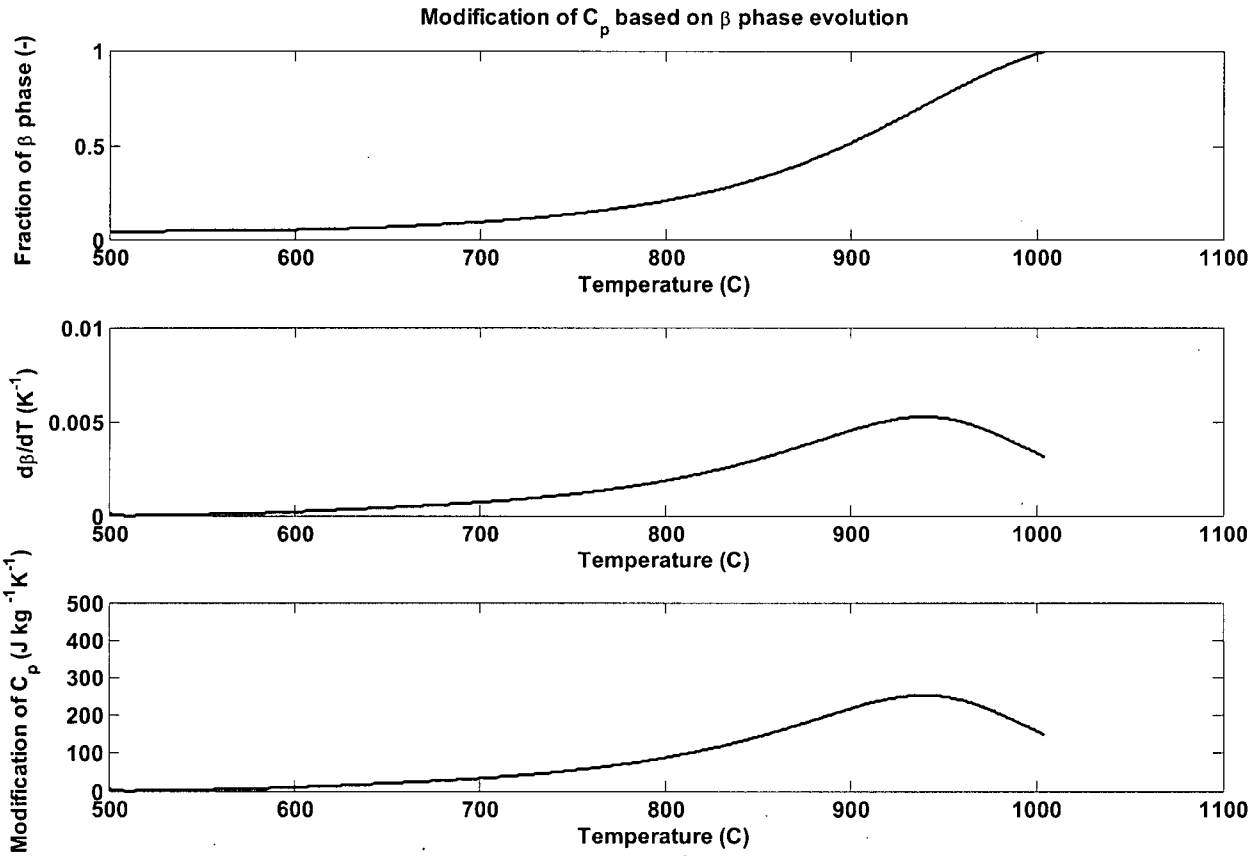

Figure 5.5 - Modification of the specific heat based on the β phase evolution.

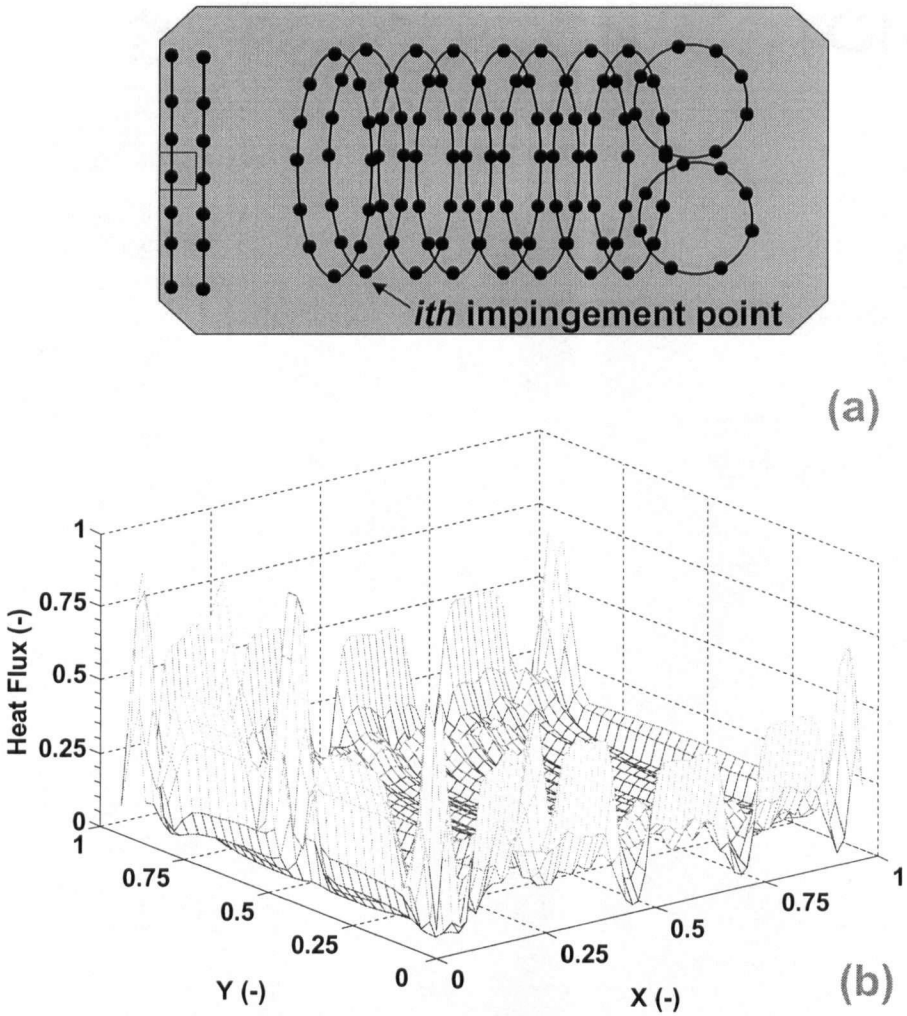

Figure 5.6 - Schematic illustration of an electron beam pattern with impingement points indicated (a), and the effective heat flux from electron beams and absorbed by the top surface of the steady-state model (b).

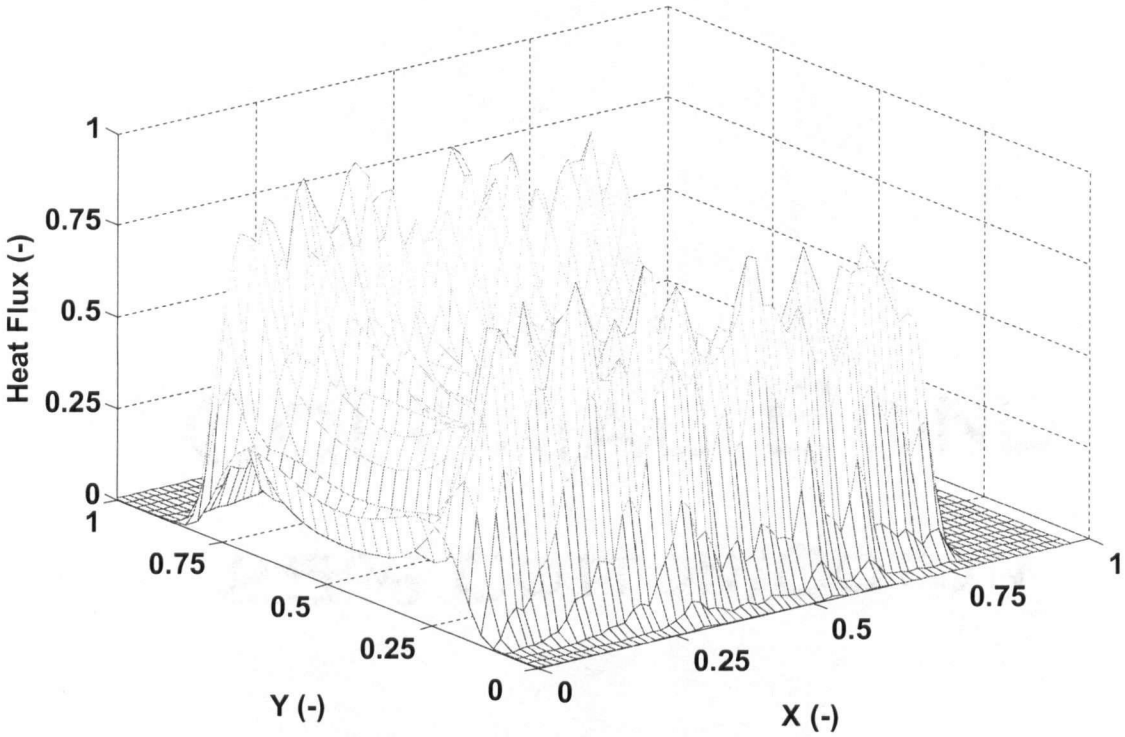

Figure 5.7 - The effective heat flux from electron beams and absorbed by the top surface of the transient-stage model.

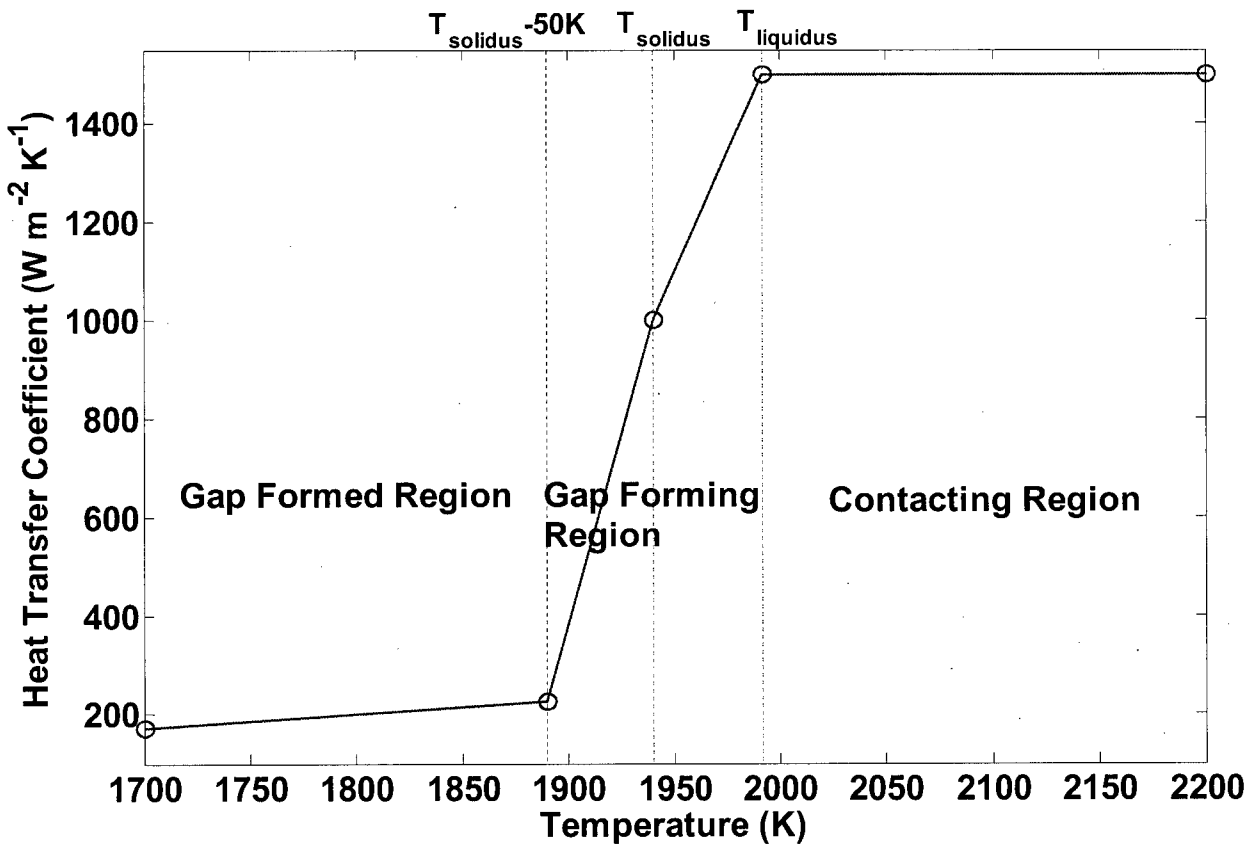

Figure 5.8 - The heat transfer coefficient for the mould cooling region.

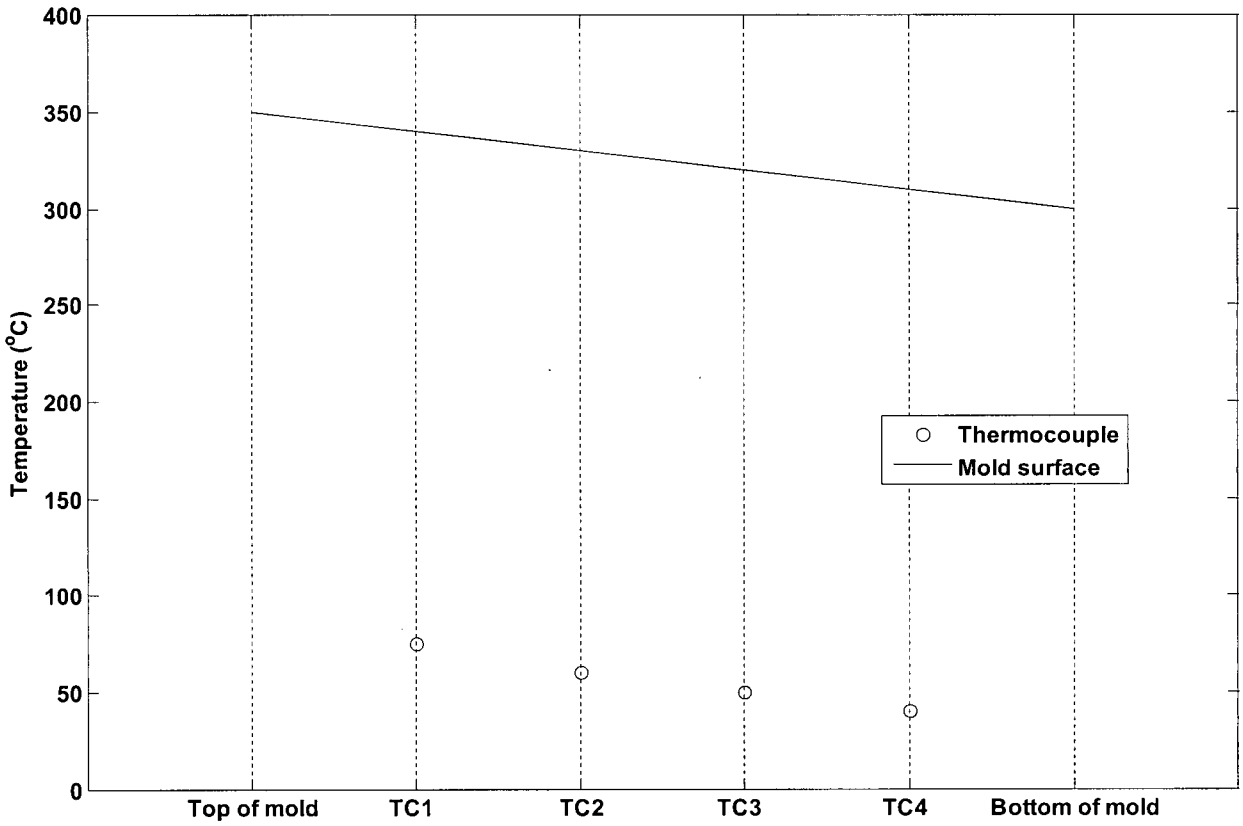

Figure 5.9 - Ambient temperature for the mould cooling region.

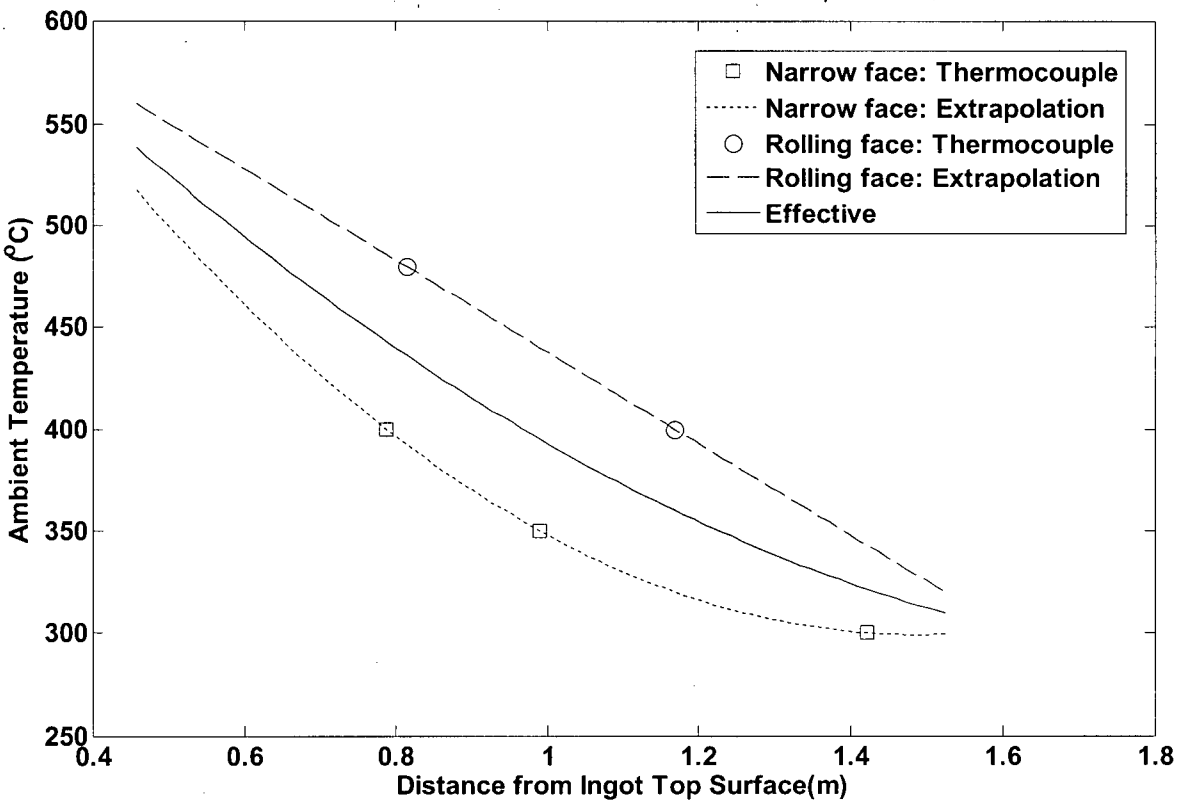

Figure 5.10 - Ambient temperature for the below-mould region.

CHAPTER 6. RESULTS AND DISCUSSION

6.1. Model Verification

In order to verify the applicability of the mathematical modeling software (CFX) and confirm that it is being used properly, it has been employed to solve a number of comparatively simple problems for which analytical solutions exist.

6.1.1. Three-Dimensional Transient Heat Conduction Problem

The first verification problem considers conduction in a solid slab with dimensions 2a x 2b x 2c in the X-, Y-, and Z-directions, respectively. The slab is cooled at its surface by a fluid, as shown in Figure 6.1. Given that the initial temperature of the slab is T_0, the convective heat transfer coefficient at the surface is h, and that the ambient temperature of the fluid is T_a. The temperature at time t, for an arbitrary point (x, y, z) in the slab can be calculated by superimposing the analytical solutions for one-dimensional heat conductance problems [46]:

$$\frac{T(x,y,z,t)-T_a}{(T_0-T_a)} = f(x,t)f(y,t)f(z,t) \tag{6.1}$$

where

$$f(x,t) = \sum_{n=1}^{\infty}\left\{\frac{2h_c\cos(\alpha_n x)}{\left[(h_c^2+\alpha_n^2)a+h_c\right]\cos(\alpha_n a)}\exp\left(-\kappa\alpha_n^2 t\right)\right\} \tag{6.2}$$

$$f(y,t) = \sum_{n=1}^{\infty}\left\{\frac{2h_c\cos(\beta_n y)}{\left[(h_c^2+\beta_n^2)b+h_c\right]\cos(\beta_n b)}\exp\left(-\kappa\beta_n^2 t\right)\right\} \tag{6.3}$$

$$f(z,t) = \sum_{n=1}^{\infty}\left\{\frac{2h_c\cos(\gamma_n z)}{\left[(h_c^2+\gamma_n^2)c+h_c\right]\cos(\gamma_n c)}\exp\left(-\kappa\gamma_n^2 t\right)\right\} \tag{6.4}$$

$$h_c = \frac{h}{k} \tag{6.5}$$

$$\kappa = \frac{k}{\rho C_p} \tag{6.6}$$

$$\alpha_n \tan(\alpha_n a) = h_c \tag{6.7}$$

$$\beta_n \tan(\beta_n b) = h_c \tag{6.8}$$

$$\gamma_n \tan(\gamma_n c) = h_c \tag{6.9}$$

This problem has been solved analytically and numerically with CFX using the material properties given in Table 6.1. The temperature profiles obtained from the analytical solution and from CFX along a sample line at times corresponding to 3000s and 6000s are compared in Figure 6.2. As can be seen the results predicted with CFX are in good agreement with the results from the analytical (exact) solution to within a maximum deviation of less than 0.2 K. This demonstrates the accuracy of CFX for three-dimensional transient heat conduction problems.

6.1.2. Stefan Problem

In order to validate the latent heat calculation in the mathematical model, the classic Stefan problem was simulated with CFX and the results compared to an analytical solution [46].

In the classic Stefan problem, a semi-infinite region of liquid is initially at its freezing temperature T_f. At time t = 0, the temperature of the face at x = 0 is suddenly reduced to T_0 such that $T_0 < T_f$. This initiates the extraction of heat by conduction from the saturated liquid to the surface and the liquid begins to freeze. As the cooling continues, the interface (assumed sharp) between the solid and liquid phases penetrates deeper into the liquid region. The location of the interface at time t can be predicted via:

$$\sqrt{\pi}\ \lambda\ \mathrm{erf}(\lambda e^{\lambda^2}) = \mathrm{St} \qquad (6.10)$$

in which the Stefan number is:

$$\mathrm{St} = \frac{C_p(T_f - T_0)}{L} \qquad (6.\ 11)$$

and

$$\lambda = \frac{x_f}{2\sqrt{\kappa t}} \qquad (6.\ 12)$$

where x_f is the location of the interface at time t, and κ the thermal diffusivity.

Additionally, the one-dimensional transient temperature distribution in the problem can be calculated as:

$$\frac{T_f - T(x)}{T_f - T_0} = 1 - \frac{\mathrm{erf}(x/2\sqrt{\kappa t})}{\mathrm{erf}(x_f/2\sqrt{\kappa t})} \qquad (6.\ 13)$$

A one-dimensional model has been constructed to solve the Stefan problem. The domain length of the model is 5 m, in order to approximate the semi-infinite region. The material properties, boundary and initial conditions for the model of the Stefan example problem have been listed in Table 6.2. In the effective specific heat method, which has been adopted for use in CFX, a finite temperature interval is required for

evolution of the latent heat, whereas in the Stefan problem, the heat is released at a unique temperature (the melting point). To address this problem a small temperature range - i.e. 1897.9 - 1898K, has been used for CFX to approximate the prevailing conditions in the Stephan problem. Two different meshes with different element sizes have been used in the model (0.05m for a coarse mesh, and 0.001m for a fine mesh) to examine the sensitivity to mesh resolution.

The interface position predicted by the coarse-mesh model and the analytical result are plotted together as a function of time in Figure 6.3. For the purpose of comparison, the interface positions, based on $T_{liquids}$, $T_{solidus}$, and their average, have been plotted for the CFX predictions. As can be seen in Figure 6.3, the maximum deviation in the evolution of the position of the interface with time is less than 0.015m. The variation in temperature with position relative to the cold face obtained using the coarse-mesh model and analytical solution at 10000s is plotted in Figure 6.4. The deviation from the analytical results has also been plotted as a function of position. For the coarse-mesh model, the maximum deviation occurs at around the liquid solid interface, and it is approximately 10K.

The interface positions predicted by the fine-mesh model are plotted in Figure 6.5, together with the results from the analytical solution. As can be seen, the maximum deviation between the numerical and analytical results is less than 0.0025m. The variation in temperature with distance from the cold face at 10000 s obtained with the fine-mesh model and the analytical solution are plotted in Figure 6.6. The deviation between the two solutions with distance from the cold face has also been

plotted. For the fine-mesh model, the maximum deviation of less than 3K occurs in the solid.

Considering that the domain length is 5m and the phase transformation temperature is around 1898K, the results from the fine-mesh model are consistent with the analytical solution. Therefore, the mathematical model can simulate the effects of latent heat with satisfactory accuracy.

6.1.3. Laminar Flow through Parallel Planes

In order to verify the fluid flow capabilities of CFX, a problem involving laminar flow between two parallel plates has been simulated. The geometry of the model (1/2 domain assuming symmetry) is shown in Figure 6.7, and the material properties and boundary conditions are listed in Table 6.3. At steady state, the velocity in the model can be calculated analytically via Eq. (6.14) [47], as long as the pressure gradient in x direction $\frac{dp}{dx}$ is constant:

$$u_y = -\frac{1}{2\mu}\left(\frac{dp}{dx}\right)\left(b^2 - y^2\right) \qquad (6.14)$$

where μ is the dynamic viscosity, and b is the distance between the top and symmetry surface.

A sample line for evaluating results has been defined across the domain normal to the top surface – refer to Figure 6.7 for the location of sample line. The velocity along the sample line is compared with the analytical solution in Figure 6.8. As can be seen, the maximum deviation is less than 1.5×10^{-4} m s^{-1}. Considering the maximum velocity is 0.01 m s^{-1}, it may be concluded that the model accurately predicts the fluid velocities for this type of problem and that it is being run correctly.

6.2. Model Predictions and Validation

6.2.1. Steady State Model

The model has been run for the standard practice conditions used at TIMET for EBCHR production of sheet ingots. The stead-state results will be introduced prior to discussing model validation. Finally, the effect of different casting parameters will be presented for use in optimizing the EBCHR process. In Table 6.4, the input parameters for the steady-state model are summarized, including: model geometry, mesh, materials properties, boundary conditions, initial conditions, and model control parameters.

6.2.1.1. Results of the Steady State Model

Temperature Field

The temperature contours on the planes bisecting the ingot narrow and rolling faces are presented in Figure 6.9. The maximum temperature predicted in the model is 2122K, which is equal to the temperature of inlet liquid. This indicates that heat flux supplied via the electron beam to the ingot top surface does not further increase the temperature of the liquid. Referring to Figure 6.9, the predicted depth of the liquid pool is 0.656 m. The sump depth (defined as the maximum distance from the top surface to the solidus isotherm) is 0.82 m, and the maximum thickness of the mushy region is 0.165 m. It is also interesting to note that the temperature profile in Figure 6.9 (a) is slightly asymmetric due to the presence of the pour stream on the left-hand-side of the plane shown.

Figure 6.10 shows the contour plots of temperature on the rolling and narrow

faces of the ingot. As can be seen from Figure 6.10, the area of the ingot surface, which is fully or partially in contact with the mould ($T_s > T_{solidus} - 50K$, referring to Figure 5.8) is very small. In fact, this portion of the surface represents less than 0.7% of the side surface area of the ingot model. Although the heat transfer coefficient in the contact region is ~7 times higher, the dominant mechanism for cooling the ingot in EBCHR is radiation.

The temperature profiles along two sampling lines parallel to the casting direction at the center of the ingot and along the center of the rolling face are presented in Figure 6.11. The rolling face temperature exhibits a rapid decrease in the first 0.2 m of the mould, transitioning to a slower cooling rate in the bottom section of the mould and below, consistent with the transition from contact conduction to radiation cooling. It is interesting to note that at steady state, the maximum temperature exhibited by the rolling face is just below the solidus consistent with the formation of a solid film at the meniscus. In contrast, the central temperature profile exhibits limited cooling until well below the mould when solidification occurs. This limited variation in temperature with distance is related to the significant transport of heat by metal flow within the liquid. Within the mushy zone there is a rapid decrease in fluid flow, resulting in the development of a significant axial temperature gradient. Below the sump, the only transport mechanism is conduction and a significant temperature gradient develops.

Velocity Fields

The flow field has been examined on a plane bisecting the narrow faces of the

ingot. The magnitude of the flow is shown in Figure 6.12 (a) and the direction of the flow is shown in Figure 6.12 (b). In Figure 6.12 (b) the size of the vectors are proportional to their velocity. The profiles of the liquidus and solidus temperatures are plotted as red and green lines, respectively.

Referring to Figure 6.12, the resulting flow field is complex; however, there are several distinct features. For example, the shape of the solid shell has a significant effect on flow fields within the ingot as it tends to focus the inlet pour stream and redirect it horizontally. As a result, the largest flow velocities are in the horizontal direction in close proximity to the inlet area. The flow then moves across the surface of the ingot until it comes into contact with the solid shell on the opposite side and then is directed downward. The flow downward along the interface between the liquid sump and the mushy zone will also be influenced to some degree by gravity as the metal cools and becomes denser. Figure 6.12 (b) also shows some evidence of gravity driven flow adjacent to the mushy zone just below the metal inlet.

In another example, on the side of the ingot opposite the metal inlet, there is clearly a recirculating flow field or cell that is driven by the downward flow of material adjacent to the mushy zone. The material directed upward within this cell appears to penetrate into the horizontal flow regime on the top surface of the ingot near the centre causing some of the flow to be directed downward in the centre of the liquid pool.

Thermal Balance

A global thermal balance has been performed on the ingot model with the results

presented in Table 6.5. As can be seen, the inlet liquid titanium contributes 65.3% to the total power input, while the electron beam provides 34.7%. The largest loss is through the ingot side walls, i.e. the mould cooling and below-mould regions, which result in 44.7 %. The heat loss due to radiation from the ingot top and outlet are 31.1% and 24.2% respectively. The enthalpies for the inlet and outlet are calculated with a reference enthalpy at room temperature, 298 K. It is evident from this analysis that the electron beam input is almost balanced by the radiation loss across the top of the ingot.

6.2.1.2. Validation of the Steady State Model

A Ti64 alloy ingot was produced by TIMET using their standard EBCHR process for the purpose of investigating the sump depth and profile and the development of voids during the final transient stage of the process. The dimensions of the ingot, casting rate, inlet liquid superheat, electron-beam power, and ambient temperatures of the mould and chamber wall are consistent with the model described in Chapter 5. The sump depth and the temperature distribution on the ingot top surface at steady state were measured following the procedures described in Chapter 4 to provide data suitable for validation of the steady-state model.

Sump Profiles

The calculated and measured profiles of the melt pool in the ingot along the plane bisecting the narrows faces are compared in Figure 6.13. The measured sump depth as determined by the location of one of the tungsten samples falls within the mushy zone predicted by the model as would be expected. Both the experiment and

prediction give a sump depth (D_{sump}) of approximately 0.8m. The shaded regions on the sectioned ingot correspond to shape of the sump profile when marked by the addition of copper. Qualitatively, the shape of deepest sump profile marked in the experiment is similar to the predicted profile.

Surface Temperature Profiles

The measured and calculated temperature distributions on the top surface of the ingot are compared in Figure 6.14. The temperature distributions on both contours are similar to each other: On the inlet (left) side of the contour, there is a narrow high-temperature region, which results from the inlet of superheated liquid in combination with the electron beam pattern, which deposits a relatively large amount of energy in the pour spout area. Moving from left-to-right, radiation cooling becomes dominant, and produces a relatively cold region. In the large central region, the ingot surface is hot. The coldest regions in both the measured and predicted temperature distributions lie on the right side, due to decreased electron beam input and the mould cooling. It can be seen that the calculated and measured surface temperature profiles are in satisfactory qualitative agreement.

6.2.2. Transient Stage Model

As described above, the experimental ingot produced at TIMET was also used to investigate the formation of shrinkage voids during the final stages of the casting process. The process parameters used during production for the final stage of casting are considered TIMET intellectual property and as such have not been presented in this thesis. The model has been run for the conditions used at TIMET for the

transient-stage experiment, which includes the termination in metal feeding (ingot withdrawal) and use of a reduced power input and a change in the beam pattern for a period of time ("hot top" period). The evolution of the temperature field predicted by the transient-stage model is first introduced, and then the validity of the model is examined by comparing the model and experimental results. It should be noted that the initial condition for the transient-stage model is based on the results of a prior version of the steady-state model, which gives a similar temperature field as described in section 6.2.1.

6.2.2.1. Results of the Transient Stage Model

Evolution of Temperature Fields

The temperature contour on planes bisecting the ingot narrow and rolling faces have been used for the purpose of describing the final-stage transient model. The temperature contours on the sample planes at 0s, 300s, 900s, 1800s, and 3050s (final solidification) after the "hot top" period are shown in Figures 6.15 - 6.19.

In comparison to the steady state temperature distribution (refer to Figure 6.9) the temperature contours at the end of the "hot top" in Figure 6.15, show a significant reduction in the depth of the liquid pool associated with a termination of liquid feeding and a reduction in the electron beam power input. A significant portion of the top surface remains liquid. However, there is some thickening of the solid shell adjacent to the mould. The amount of electron beam energy input to the top surface during the "hot top" would appear to be sufficient to offset a significant portion of the radiation losses from the top surface, thus keeping the surface liquid. A dramatic

asymmetry has also developed in each direction due to the termination of incoming metal and asymmetries in the applied electron beam pattern.

Once the "hot top" period is terminated, there is no electron beam energy input to balance the heat extracted via radiation from the ingot top surface, where a solid shell rapidly forms. As shown in Figure 6.16, at 300s, the solid shell on the top surface has formed, and there is also a further significant reduction in the depth of the liquid pool and an increase in the solid shell thickness adjacent to the mould.

At 900s, the liquid pool inside the ingot transforms into mush, as shown in Figure 6.17, albeit most of it has a fraction solid less than 0.2. From 900s to 1800s, the volume of semi-solid material or mush further diminishes, as shown on Figure 6.18. By 3050s, Figure 6.19, the remaining mush has transformed into solid. The point of final solidification is predicted to occur 0.26 m below the ingot top surface.

The temperature profiles along the center line of the ingot at 0s, 150s, 200s, and 3050s after the "hot top" are given in Figure 6.20. At 0s, the sump depth of the ingot is around 0.61m. From 150s to 200s, the temperature on the ingot top surface drops to below the solidus temperature. The depth of the final solidification point, occurring at 3950s after the "hot top", is around 0.26m.

The temperature evolution at the center of the ingot on the top surface is shown in Figure 6.21. During the "hot top" period, the temperature is almost constant, confirming that the energy input from the electron gun virtually offsets radiation loss. Once the "hot top" has been terminated, the temperature drops sharply to the liquidus temperature. When the temperature reaches the solidification temperature range, the

rate of temperature decrease slows due to the evolution of the latent heat during solidification. It takes ~100s for the top surface to solidify following the "hot top". Once solidification is complete, the cooling rate becomes relatively high and then gradually decreases with increasing time.

6.2.2.2. Validation of the Transient Stage Model

Temperature on Ingot Top Surface

A series of comparisons between the predicted top surface temperature distributions and the measurements obtained with the near infrared filter/video camera image, following processing, are presented in Figures 6.22 - 6.24. Comparisons have been made at 300s, 900s, and 1800s, during the transient stage.

As shown in Figure 6.22, at 300s, the top surface has already begun to cool considerably, particularly in close proximity to the mould due to the termination of mass feeding, the reduction in electron beam power, and the change in the electron beam scanning pattern (from steady-state to "hot top" pattern). As can be seen, both the model and experimental results are in relatively good agreement. For example, both show two high temperature zones extending over approximately one third of the top face parallel to the two rolling faces, which are consistent with the "hot top" electron beam pattern.

Turning to Figure 6.23, by 900s, there is a further reduction in the area of the top surface that is at a high temperature in both the model and the measurement. The pattern is consistent with continued removal of heat from the mould. The degree of agreement between the model predictions and the measurements is quite good, with

the model slightly underestimating the extent of the cooled region in proximity to the mould.

By 1800s, the model results and the measurements show only a relatively small area in the middle of the casting still hot, as shown in Figure 6.24. The agreement between the model and measurement is good and the tendency to under predict mould cooling exhibited in the results for 900s is no longer obvious at 1800s.

From Figures 6.22 - 6.24, it is clear that the transient thermal model is able to qualitatively reproduce the cooling behavior on the top surface of the ingot.

Temperature Evolution at Discrete Locations on Ingot Top Surface

The temperature evolution during the transient stage was quantitatively measured with two thermocouples placed in contact with ingot top surface, as discussed in section 4.2.2. The temperature profiles from the thermocouples are plotted in Figure 6.25. Although the two thermocouples were placed close to each other as shown on Figure 4.5, the temperatures measured are different (thermocouple #1 reads a temperature approximately 180K lower than thermocouple #2 at the same time in the transient stage). This difference can be attributed to the insulating cover on the tip of thermocouple #1, which produced a resistance to heat transport, thus reducing the temperature measured at the thermocouple tip. Thus, despite some problems with noise, the bare-tipped thermocouple was taken to be the more accurate of the two.

The results comparing the two top surface thermocouple measurements to the model predictions are shown in Figure 6.25. It can be seen that the predicted temperatures are 200K hotter than measured by the second thermocouple. It is

interesting to note that in contrast to the absolute temperatures, which show a considerable discrepancy, the predicted cooling rates closely approximate the experiment results. The agreement in cooling rates would imply that the basic boundary conditions used to describe heat transport in the model are correct. The discrepancy in temperature, on the other hand, could be due to thermal contact resistance between the bare thermocouple wire and the ingot surface. In the procedure used to acquire the data, the thermocouple was placed at the end of a long tube introduced through one of the vacuum ports in the furnace. It is possible that the pressure exerted on the thermocouple tip using this procedure was relatively small; hence there may have been a considerable contact resistance resulting in erroneously low temperature measurements. Alternative options are being reviewed to obtain a better top surface temperature measurement.

Void Formation

In the transient final stage of the casting process, the feeding of liquid titanium stops, and the liquid pool inside the ingot transforms to solid. In the nominal process, a solid shell forms on the top surface of the ingot prior to complete solidification. Thus there is liquid encapsulation and the formation of shrinkage voids inside the ingot – i.e. mass feeding is no longer possible. During the experiment to examine void formation, the "hot top" period was increased from the nominal amount to 3300s. Correspondingly, the final transient stage model was modified and run with 3300s of "hot top". All of the other conditions, "hot top" beam power and beam pattern, were unchanged.

To aid in the prediction of shrinkage voids the Niyama number has been calculated based on the model predictions and compared with the actual locations where the voids formed in the experimental ingot. The Niyama number [48] is defined as:

$$\mathrm{Nym} = \frac{G}{\sqrt{R}} \tag{6.15}$$

where G is the temperature gradient, and R is the cooling rate. For each point in a casting, the Niyama number is evaluated at the end of solidification. Niyama et al define the end of solidification as the time when the temperature first reaches or drops below the solidus temperature [48]. Thus, the Niyama number is calculated on the iso-surface of the solidus temperature. A lower Niyama number indicates a higher possibility for the formation of shrinkage voids as it reflects a longer feeding distance (lower G) and faster solidification/feeding rate (higher R), both of which would tend to result in an increased tendency for voids to form.

The contours of Niyama number at 3900s (600s after the conclusion of the "hot top") and 4400s (250s before final solidification) are given in Figures 6.26 and 6.27, respectively. As shown in Figure 6.26, there is a band of material with low Niyama number predicted to occur approximately 75% of the way down in the pocket of mushy material at 3900s. Moreover, this band is biased toward the metal inlet end of the casting. At 4400s, the bands of material exhibiting low Niyama number appear on both ends of the pocket of mushy material.

The lowest Niyama number along the solidus contour on a sample plane bisecting the narrow faces of the ingot can be calculated and compared with the

location of shrinkage voids found in the ingot. The results are shown in Figure 6.28. The lowest Niyama point on each curve is marked as a small square. In comparison, the positions of shrinkage voids from the experiment are indicated as small circles. As shown on Figure 6.28, the calculated and measured shrinkage voids all lie on the inlet-side of the ingot. Moreover, there is fairly good agreement between the measured and calculated positions of the voids.

In the EBCHR production of titanium ingots, the top portion of the ingot is cropped to avoid any voids in the final products using a considerable safety margin. Therefore, an accurate prediction of the lowest void position is important to industrial production. From Figure 6.29, it is apparent that the lowest void point measured corresponds to the location of final solidification predicted by the model. Thus, the model could be used as an effective tool to predict the point of lowest void thus potentially reducing the crop size or scrap rate.

6.3. Process Sensitivity Analysis

6.3.1. Sensitivity Analysis – Model Parameters

The model has been run with the following parameters varied: (1) domain length, (2) mesh size, and (3) time step length. The results indicate that the EBCHR model was run with values for these parameters in a range that did not significantly influence the accuracy of the predictions.

6.3.2 Sensitivity Analysis – Process Parameters

In this section, the effect of varying casting rate, beam power, and superheat on sump depth has been evaluated. These parameters represent controllable process

variables in the industrial operation. The parameters were each varied from 75% to 150% of the nominal value while the other parameters were unchanged - i.e. the electron beam power was varied from 450 kW to 900 kW. The sump depth during steady state casting was chosen to indicate sensitivity since in the previous section it was found to have a significant effect on the extent and location of void formation during final solidification.

The effects of these casting parameters on the ingot sump depth are shown in Figure 6.30. The casting rate has the most significant effect on sump depth, followed by the electron beam power. In contrast, the effect of inlet superheat was found to be relatively small. In order to explain these effects, the thermal balances have been performed on models with 125% casting parameters, and the results are presented in Table 6.6. From the heat balances, it is evident that 65.3% of the total energy input comes from the sensible heat of the inlet metal, the balance or 34.7% comes from the electron beam power applied to the top surface. In terms of the total enthalpy associated with the metal feed, only ~8% is associated with the liquid superheat (temperature in excess of the liquidus). Thus, the model is relatively insensitive to changes in metal inlet superheat. Moreover, any changes imposed on the model that result in an increase in the liquid metal temperature (increase in liquid metal superheat or electron beam power) will tend to be offset to a certain extent by an increase in radiation losses from the top surface.

In addition, the variations of both casting rate and electron beam power have

linear relationships with sump depth variation, which are expressed in the following non-dimensional equations:

$$I_{sump,flow} = 1.143 \times I_{flow} \tag{6.16}$$

$$I_{sump,EB} = 0.420 \times I_{EB} \tag{6.17}$$

where I_{flow} and I_{EB} are the variation in casting rate and electron beam power; and $I_{sump,flow}$ and $I_{sump,EB}$ are their effects on the sump depths, respectively.

If the effects of casting rate and electron beam power are superimposed, Eq. (6.16) and (6.17) give:

$$I_{sump} = 1.1427 \times I_{flow} + 0.4198 \times I_{EB} \tag{6.18}$$

In order to validate Eq. (6.18), the model has been run for four additional cases with combinations of different casting parameters, in which the electron beam power is varied from its 75% or 125%, and the casting rate is varied from its 75% or 125%. The predicted sump depths are compared with those calculated using Eq. (6.18) in Figure 6.31. As can be seen, the sump depths calculated by the equation are close to those predicted by the CFD model, although, overall the equation tends to overestimate the sump depth.

6.4. Process Optimization

As discussed in the previous chapter, shrinkage voids may form on the top portion of the ingot during the final transient stage of the casting process. In order to prevent these defects in the final product, the top part of the ingot is usually cropped at a safe distance below where the lowest void is likely to form, based on past experience. If the position of the lowest void could be move upwards toward the top surface of the ingot less material would need to be removed and the productivity of the EBCHR process would be enhanced.

From the discussion in section 6.2.2, the lowest void in an experimental casting was found to occur approximately at the location of the last point predicted to solidify in the ingot with the model. In industrial practice, a longer "hot top" period in combination with a reduction in casting speed at the end of the casting process could be used to move the location of the final solidification point toward the top surface and avoid internal voids. This strategy is successful in casting commercial purity titanium. In the case of casting alloys, however, the strategy to avoid losses associated with voids is not straightforward as the longer "hot top" times will cause increased evaporation of high vapor pressure elements thus resulting in material that deviates from the chemical composition specifications. As a result, material may still have to be removed from the ingot top as it is off chemical specification even though few or no voids are present.

The objective of this section is to demonstrate how the model may be used to optimize the casting of Ti64 alloy ingots, where evaporation is a potential issue. Ultimately, the optimization approach that would be adopted should seek to strike a

balance between void formation (long "hot top" times and/or high "hot top" power input) and alloy chemistry control (no "hot top"). In the section below two approaches are examined separately, as a means of demonstrating the model's utility. It is important to point out that the results presented below do not represent optimal solutions and that the best strategy may well involve a combination of these.

6.4.1. Casting Rate Strategy

From section 6.3.2, it is evident that the casting rate has a significant effect on the sump depth of the ingot during steady state operation. Based on these results, the effect of ramping down the casting speed near the end of the casting process has been examined. As a first attempt, the casting speed has been set to ramp from the nominal steady state speed to 0 over a period of 1800s. Following this ramp, the nominal TIMET "hot top" strategy described in section 6.2.2 is applied in the model.

In Figure 6.32, the solidification curves for the model utilizing the withdrawal rate ramp are compared with those of the baseline transient-stage model described in section 6.2.2. The casting-rate ramp is predicted to decrease the sump depth at the end of the "hot top" by 0.13m, and the depth of the final solidification point by 0.05 - 0.06m. However, as part of an overall optimization strategy one would also have to consider the loss in productivity due to the lower casting speed associated with this approach. Thus, one would need to weigh the gain in material by reducing the amount cropped against the loss in production rate to ascertain whether this approach would result in a net increase in profit.

6.4.2. Electron Beam Strategy

From section 5.8, the baseline transient model has the electron beam scanning ~70% of its top surface during the "hot top" period, as shown in Figure 5.7. The approach to be tested involved reducing the area scanned by the electron beam while maintaining the same power density. The goal in this approach is to reduce the surface area that remains liquid during the "hot top" thereby reducing the area available for evaporation of volatile species.

In the approach tested, the electron beam pattern is adjusted so that the pattern scans ~44% of the top surface (centre portion) – refer to Figure 6.33. For simplicity, it is also assumed that the heat flux is uniform on the surface with a value of 700 kWm^{-2}. The net result is a reduction in the "hot top" power from 500 kW to 280 kW.

In Figure 6.34, the solidification curves of the reduced area/power model are compared with those of the baseline transient-stage model. From this figure it is evident that reduced area/power will result in a reduction in the surface that is liquid which will translate in to a reduction in evaporation losses. It is also apparent that this approach does not negatively affect the sump depth at the end of "hot top" or the depth of the final solidification point. Thus, the amount of material cropped should not be adversely affected.

Overall it would appear that some combination of a ramp in casting speed near the end of the process in combination with careful manipulation of the beam power/beam pattern could lead to an improvement in final void location in

combination with minimal evaporation losses.

Table 6.1 - The material properties, initial and boundary conditions for the three-dimensional transient heat conduction problem

Density	4540 [kg m^{-3}]
Specific heat (C_p)	721 [J kg^{-1} K^{-1}]
Conductivity (k)	27.62 [W m^{-1} K^{-1}]
Latent Heat (L)	0 [J kg^{-1}]
Initial Temperature (T_0)	1998 [K]
Ambient Temperature (T_a)	1073 [K]
Heat transfer coefficient (h)	300 [W m^{-2} K^{-1}]
Model Dimensions (a, b, c)	1.372, 0.674, 1.524 [m]

Table 6.2 - The material properties, initial and boundary conditions for the Stefan problem

Density	4540 [kg m^{-3}]
Specific heat (C_p)	721 [J kg^{-1} K^{-1}]
Conductivity (k)	27.62 [W m^{-1} K^{-1}]
Latent Heat (L)	307 860 [J kg^{-1}]
Liquidus Temperature ($T_{liquidus}$)	1898 [K]
Solidus Temperature ($T_{solidus}$)	1897.9 [K]
Initial Temperature (T_f)	1898 [K]
Temperature at one end (T_0)	1798 [K]

Table 6.3 - The material properties and boundary conditions for the laminar flow through parallel planes

Dynamic viscosity	0.003 [Pa s]
Inlet pressure	0.06 [Pa]
Outlet pressure	0 [Pa]
Top surface	No slip
Symmetry surface	Free slip

Table 6.4 - The input parameters for the steady state model

Geometry	Domain length	1.524m (Figure 5.2)
Mesh	Element size	0.01m - 0.051m (Figure 5.3)
Materials Properties	Density, Thermal conductivity, Specific heat	Temperature dependent (Table 5.1)
	Solidus and liquidus temperatures	1940K; 1992K,
	Latent heat for solidification and β/α	286000 J kg^{-1}; 48000 J kg^{-1}
	Dynamic viscosity	0.003 Pa s
Boundary conditions	Inlet face	TIMET's flow rate; Temperature 2122 K
	Top surface	Free slip wall; Electron beam input 600 kW, Radiation loss with ambient temperature 773 K.
	Mould cooling region	Free slip wall; Heat transfer coefficient (Figure 5.8), Ambient temperature (Figure 5.9)
	Below mould region	Free slip wall; Radiation loss with ambient temperature (Figure 5.10)
	Outlet face	TIMET's flow rate; Adiabatic
Initial conditions	Temperature	2122 K
	Pressure	0 Pa
	velocity	0 m s^{-1}
Control parameters	Time step	0.02s - 2s
	Convergence criterion	5e-5 for the maximum difference between two iterations.

Table 6.5 - Global thermal balance of the ingot model

		Power (kW)	Percentage (%)
Power	Inlet	727.5	65.3
Input	Electron Beam	387.2	34.7
Power	Outlet	-269.7	-24.2
Output	Top Radiation	-346.4	-31.1
	Mould Cooling	-324.1	-29.1
	Below Mould Cooling	-173.6	-15.6
Balance	Input-Output	0.9	0.1

Table 6.6 - Global thermal balance of the ingot models: baseline, 125% casting rate, 125% electron beam power, and 125% inlet superheat

		Power (kW)			
		Baseline	**125%Cast rate**	**125% EB**	**125%Superheat**
Power	Inlet	727.5	909.4	727.5	743.8
Input	Electron Beam	387.2	387.2	484.0	387.2
Power	Outlet	-269.7	- 384.0	-283.2	-273.2
Output	Top Radiation	-346.4	-353.0	-371.4	-350.8
	Mould Cooling	-324.1	-348.1	-368.3	-330.0
	Below Mould	-173.6	-210.4	-188.8	-176.0
Balance	Input-Output	0.9	1.1	-0.2	1.0

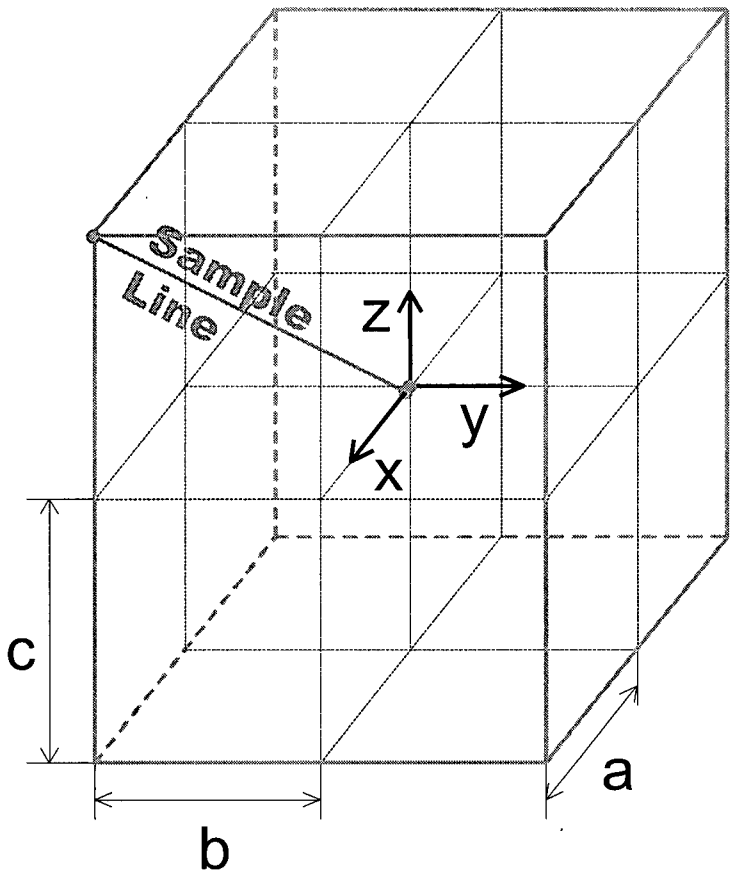

Figure 6.1- Geometry of the model for the three-dimensional transient heat conduction problem.

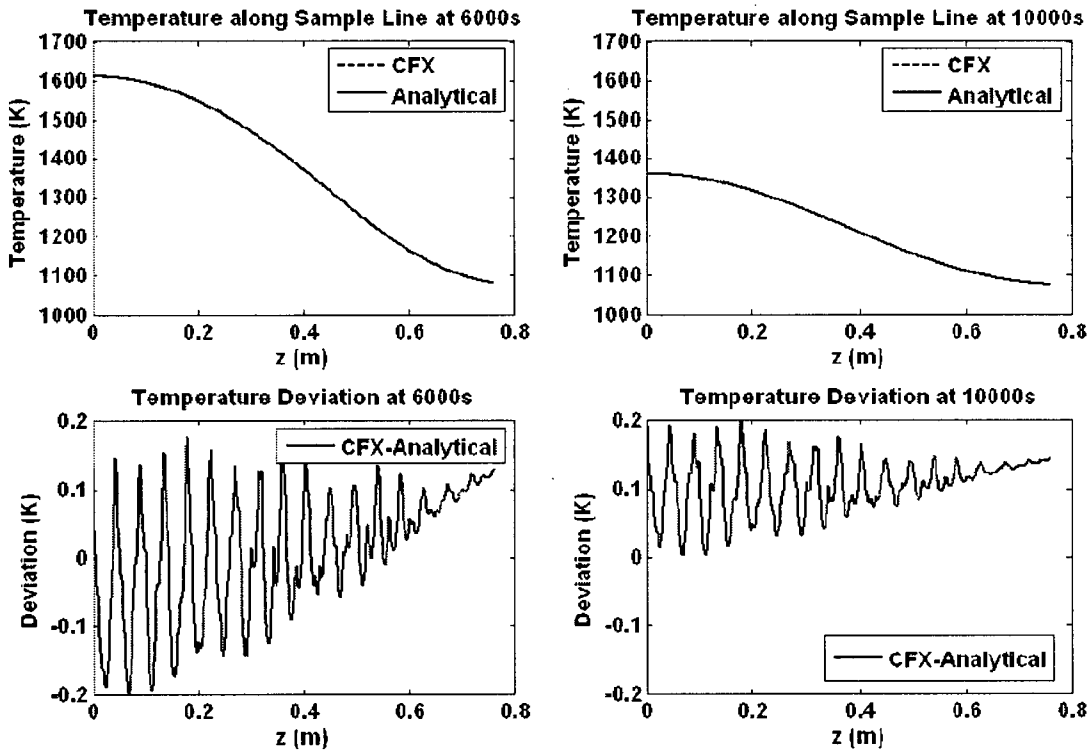

(a) (b)

Figure 6.2 - Comparison of the modeling and analytical results for the transient heat conduction problem at 6000s (a) and 10000s (b).

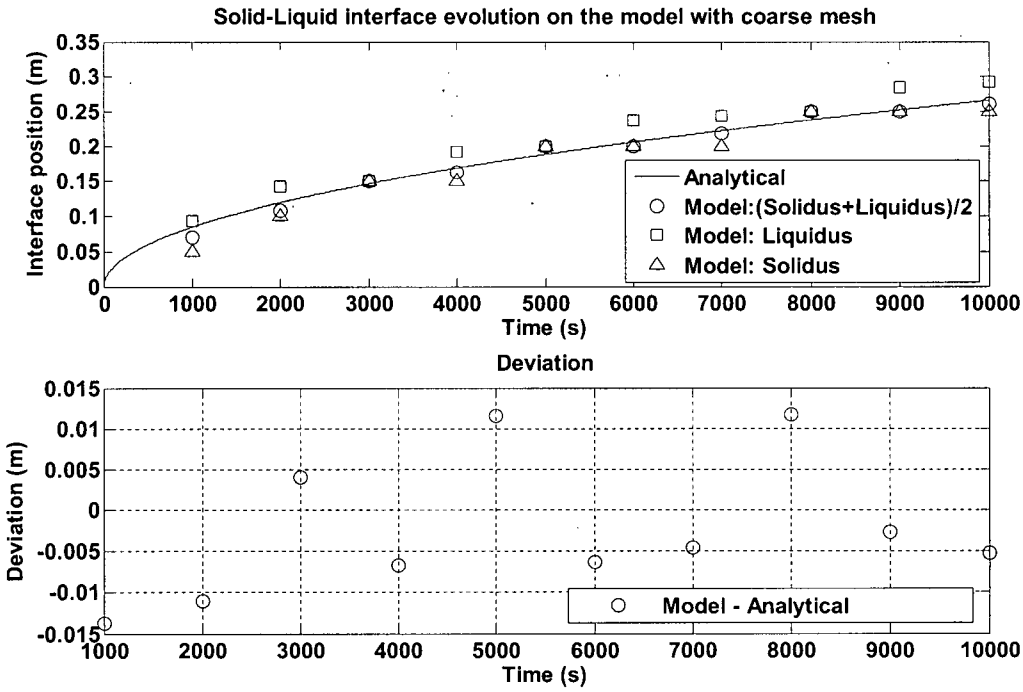

Figure 6.3 - The interface evolution for the Stefan problem given by the coarse-mesh model and analytical solution.

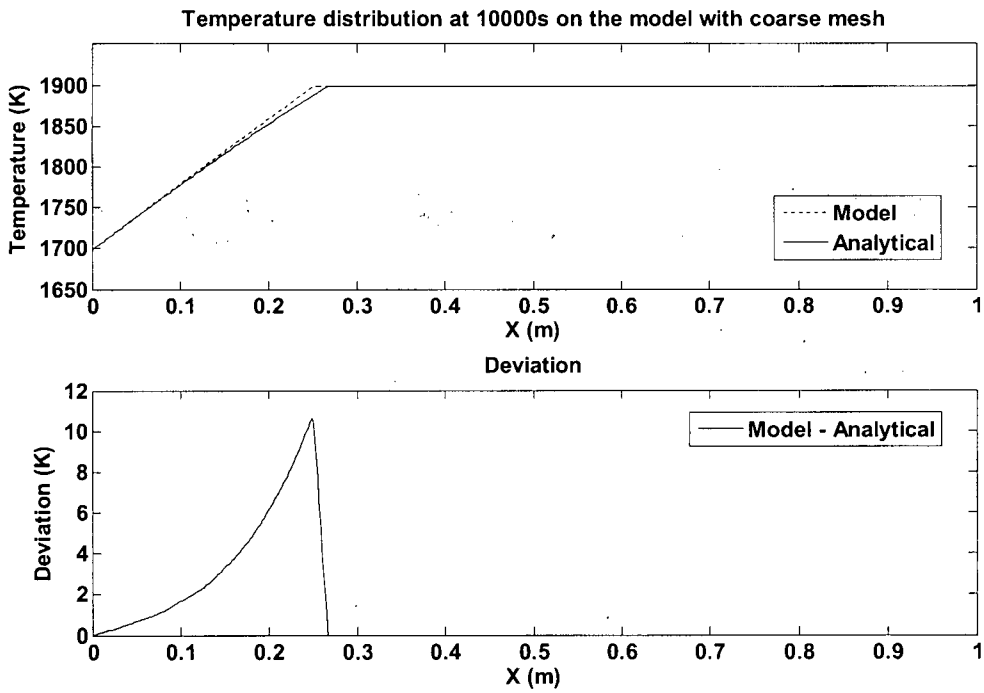

Figure 6.4 - The temperature distribution at 10000s for the Stefan problem given by the coarse-mesh model and analytical solution.

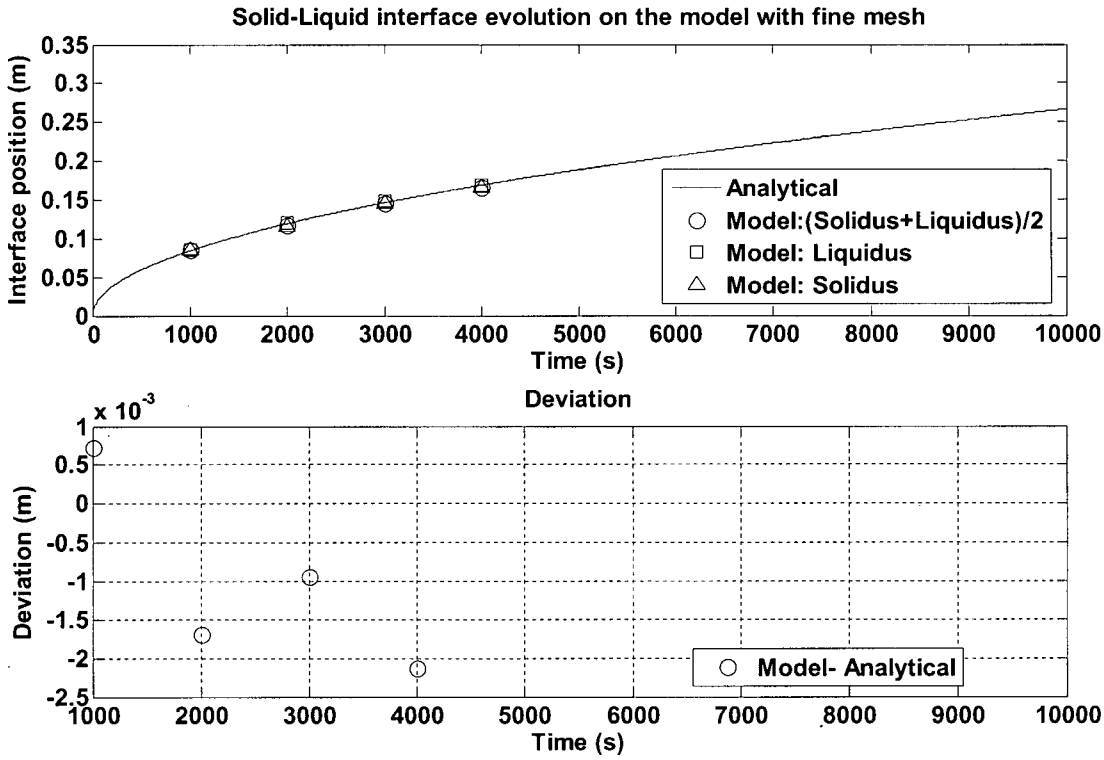

Figure 6.5 - The interface evolution for the Stefan problem given by the fine-mesh model and analytical solution.

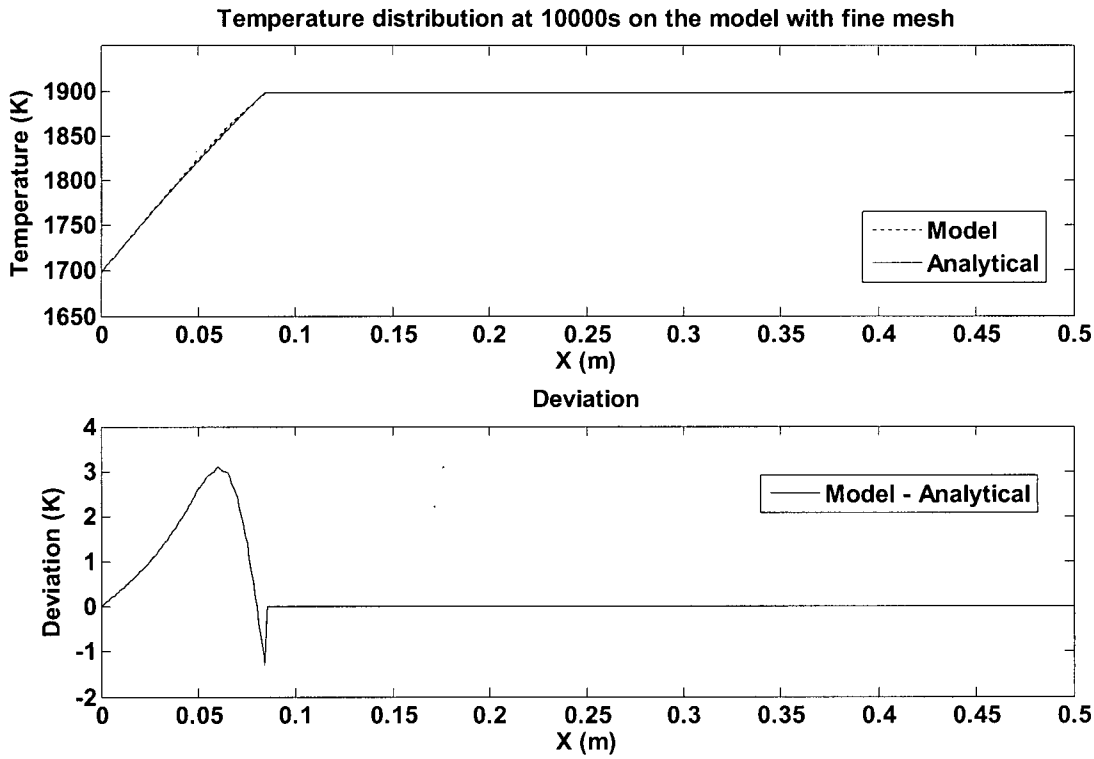

Figure 6.6 - The temperature distribution at 10000s for the Stefan problem given by the fine-mesh model and analytical solution.

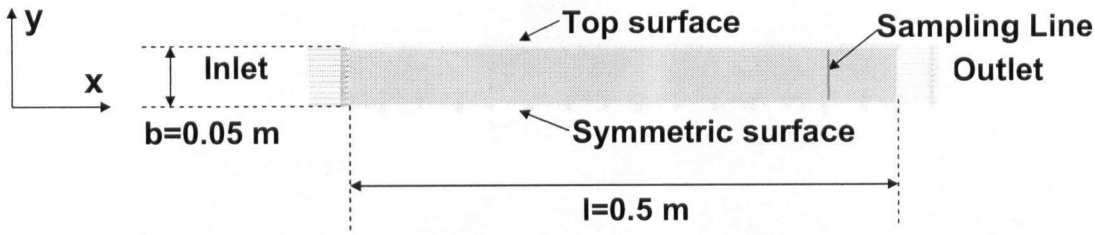

Figure 6.7 - Geometry of the model for the laminar flow between parallel plates.

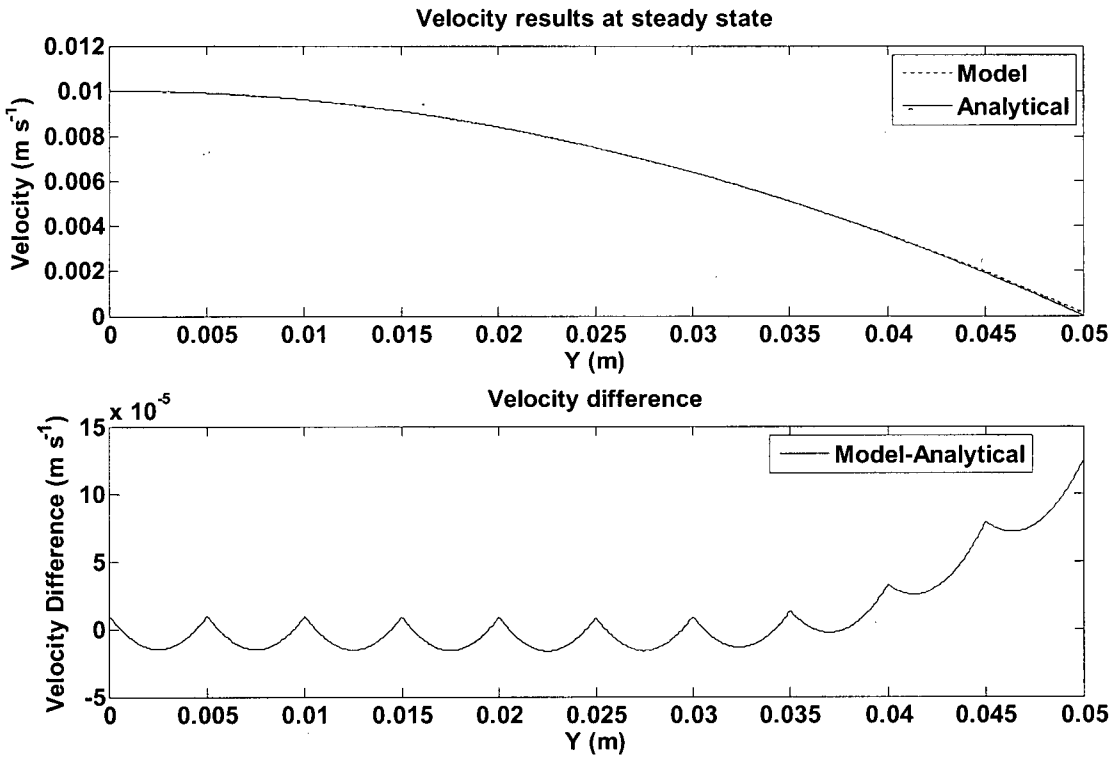

Figure 6.8 - Comparison of the modeling and analytical results for the laminar flow between two parallel plates at steady state.

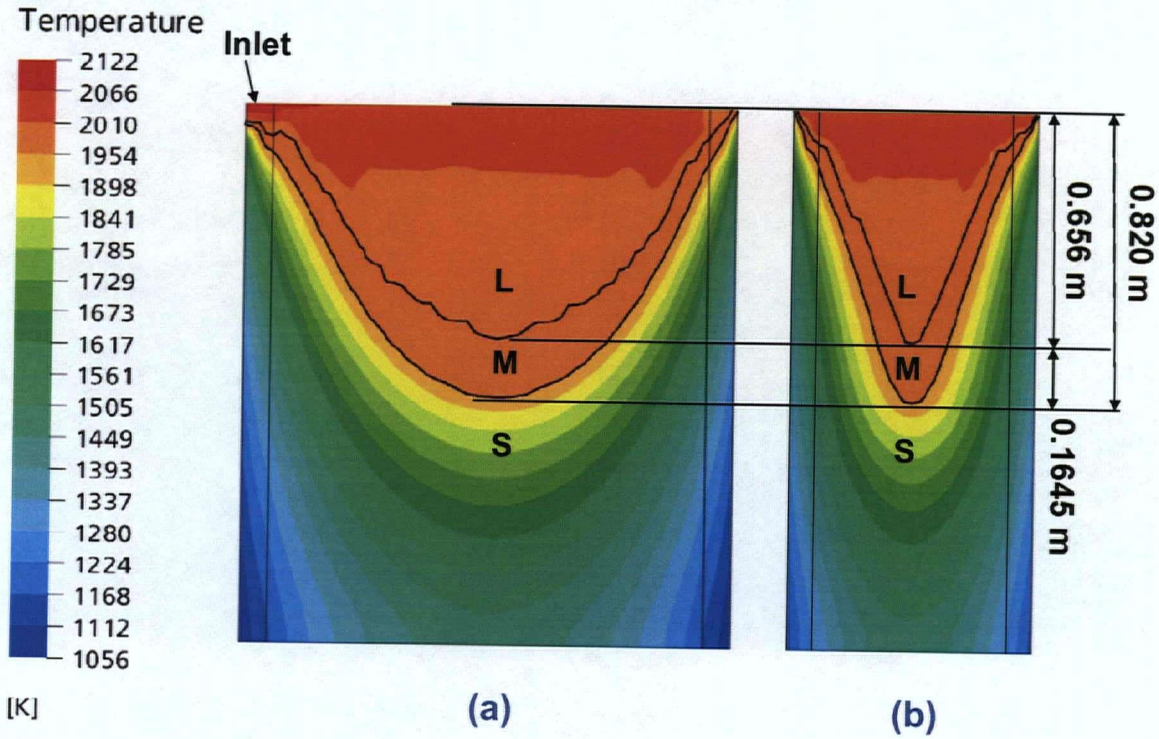

Figure 6.9 - The temperature contours on planes bisecting the narrow (a) and rolling (b) faces of the ingot model. The liquid, mushy, and solid regions are marked as L, M, and S, respectively.

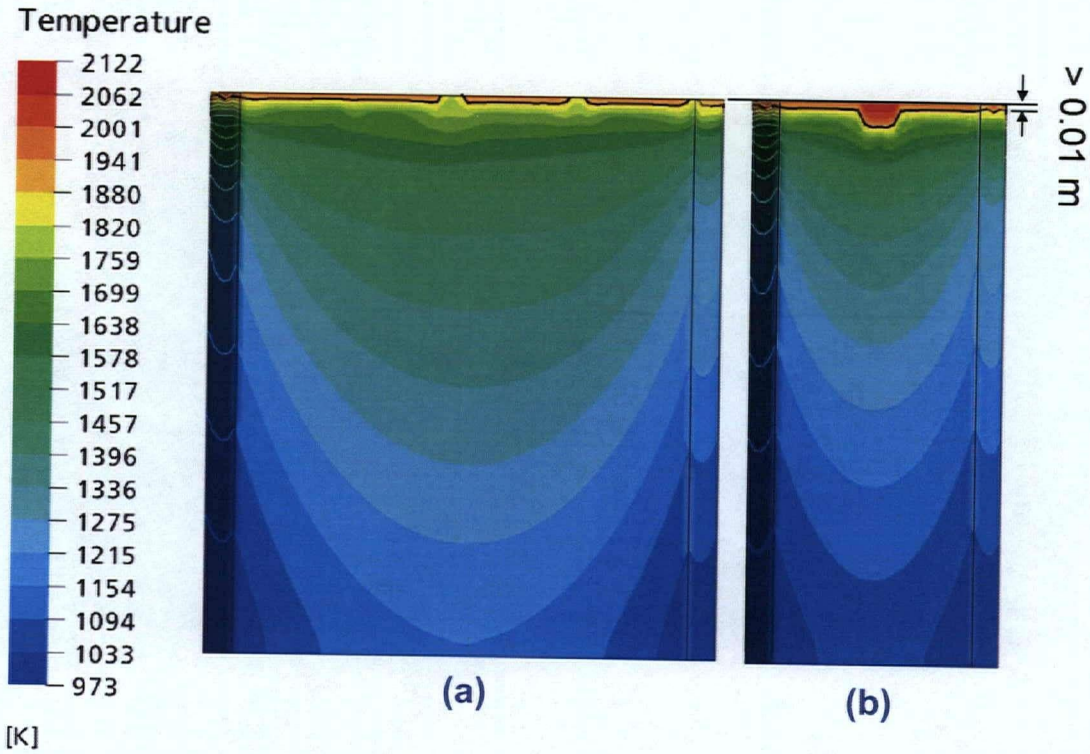

Figure 6.10 - The temperature contours on the rolling (a) and narrow (b) faces of the ingot model. The isotherm ($T_{solidus} - 50K$) representing the boundary between the contact and the gap-forming regions is indicated as a black line.

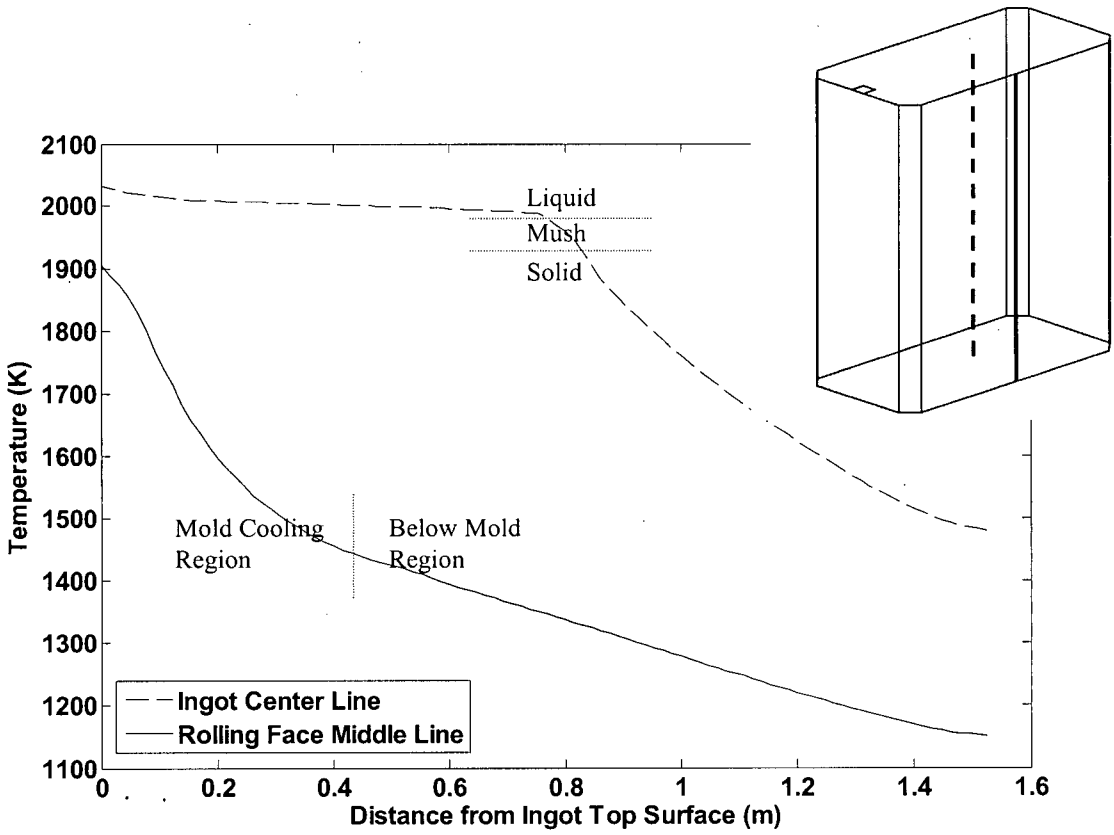

Figure 6.11 - The temperature profiles along two sampling lines.

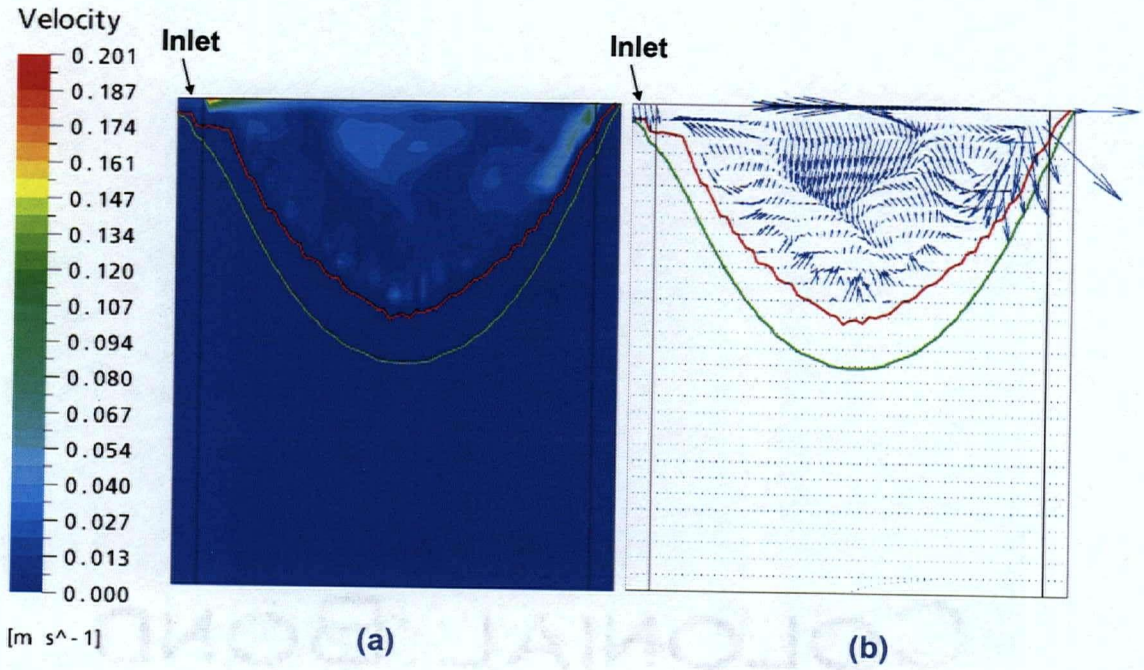

Figure 6.12 - The magnitude (a) and direction (b) of the velocity on the plane bisecting the narrow faces of the ingot.

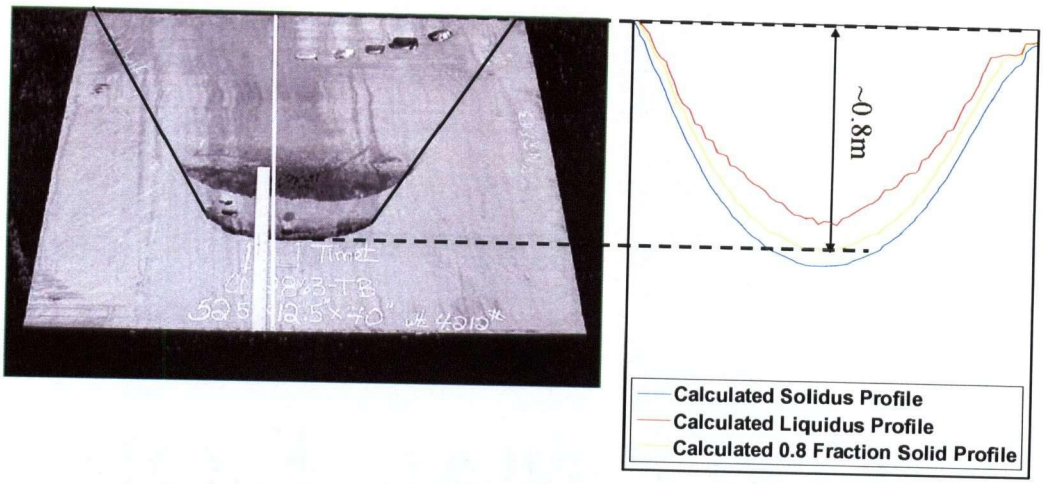

Figure 6.13 - The measured and calculated sump profiles of the ingot along the plane bisecting the narrow faces.

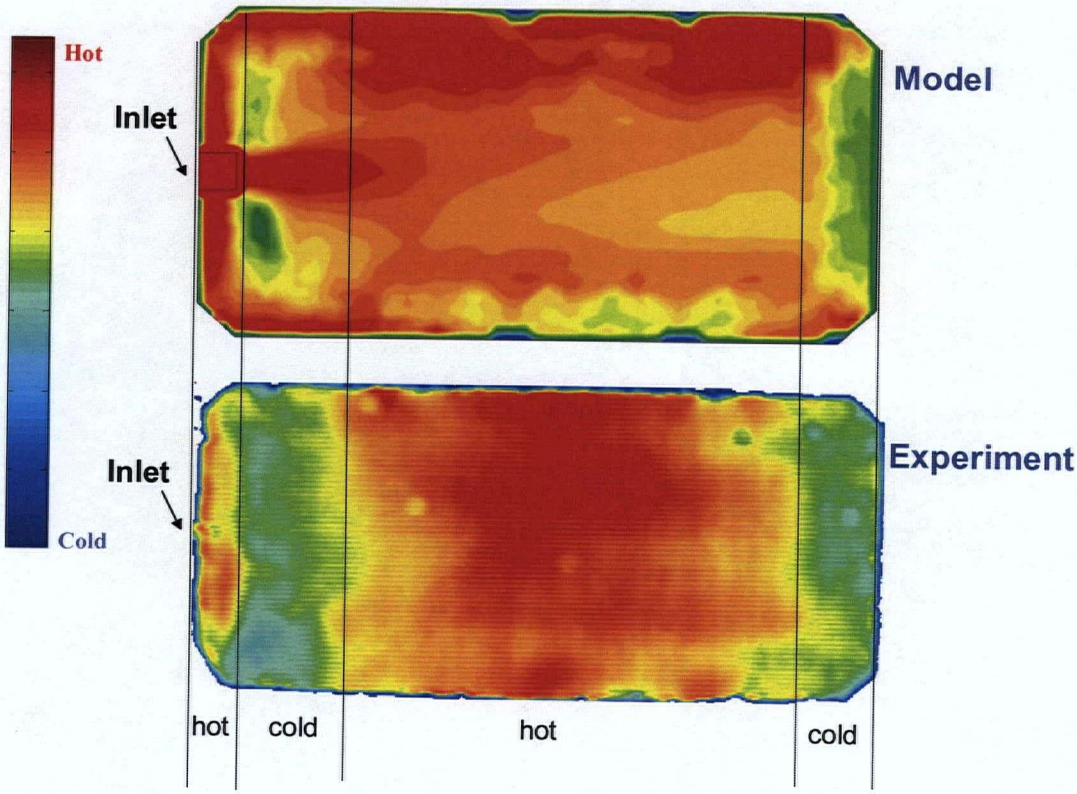

Figure 6.14 - The measured and calculated temperature contours on the top surface of the ingot.

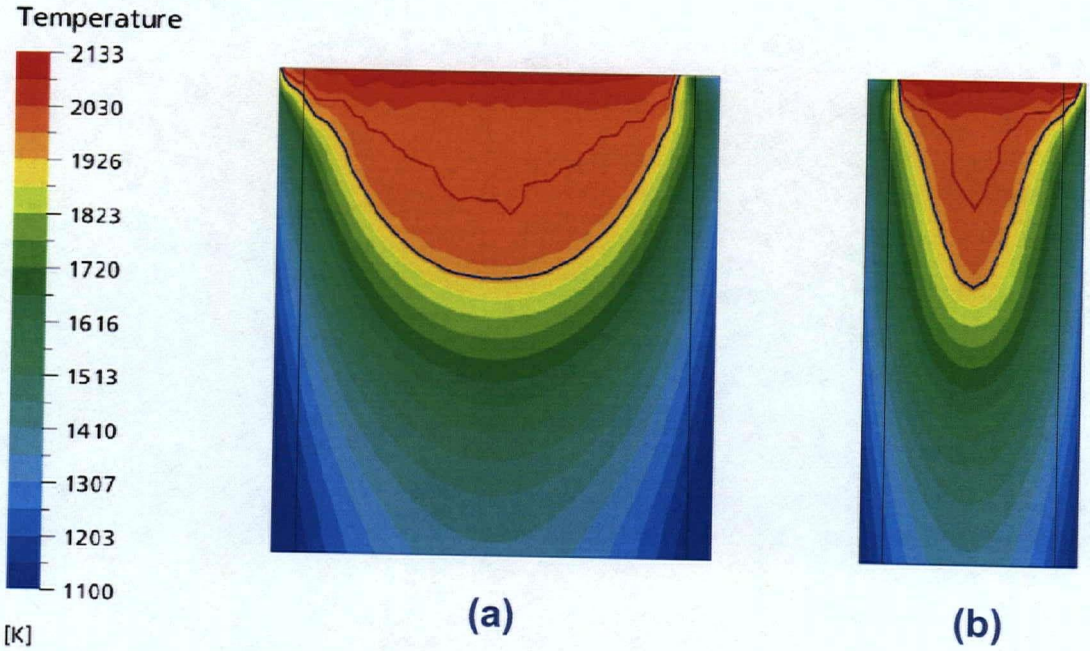

Figure 6.15 - The temperature contours on the planes bisecting the narrow (a) and rolling (b) faces of the ingot at 0s after the "hot top" period.

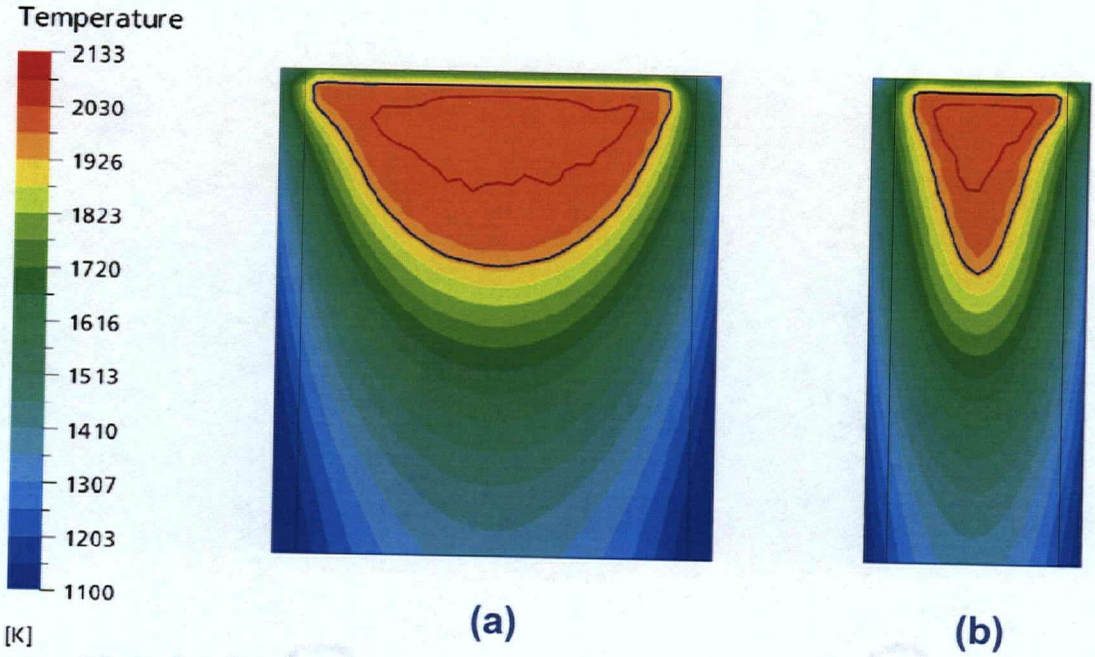

Figure 6.16 - The temperature contours on the planes bisecting the narrow (a) and rolling (b) faces of the ingot at 300s after the "hot top" period.

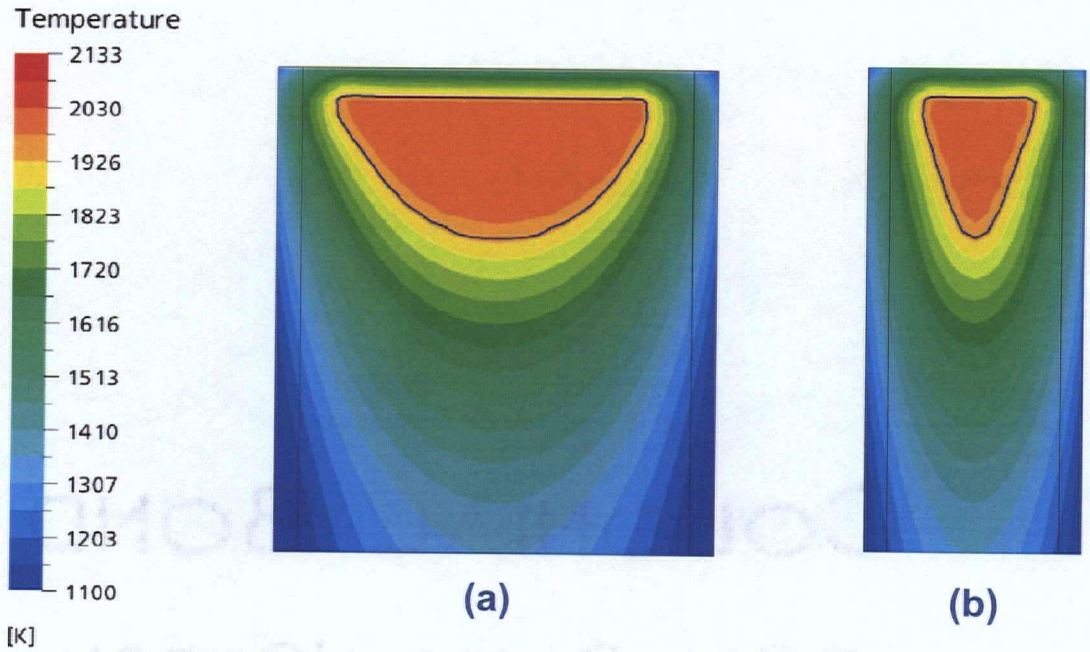

Figure 6.17 - The temperature contours on the planes bisecting the narrow (a) and rolling (b) faces of the ingot at 900s after the "hot top" period.

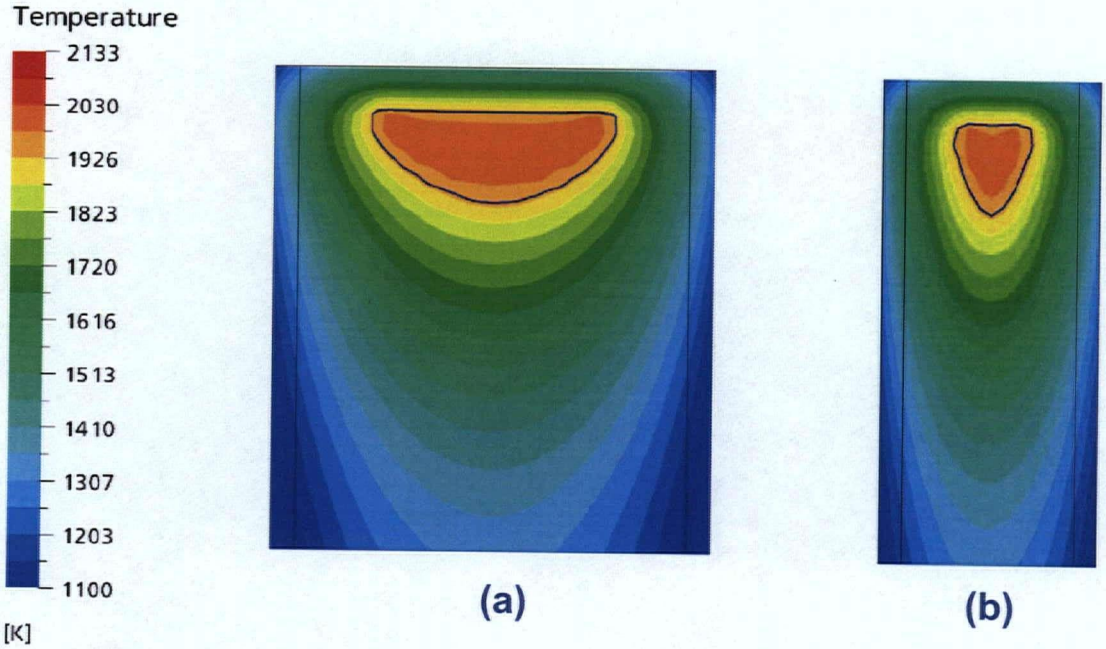

Figure 6.18 - The temperature contours on the planes bisecting the narrow (a) and rolling (b) faces of the ingot at 1800s after the "hot top" period.

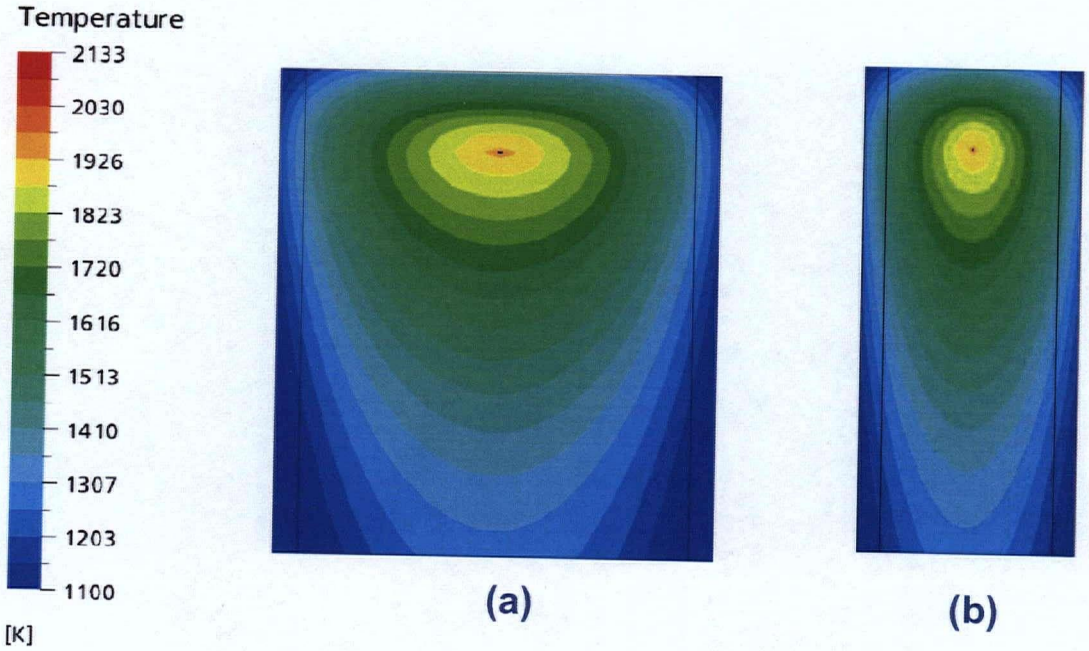

Figure 6.19 - The temperature contours on the planes bisecting the narrow (a) and rolling (b) faces of the ingot at 3050s after the "hot top" period.

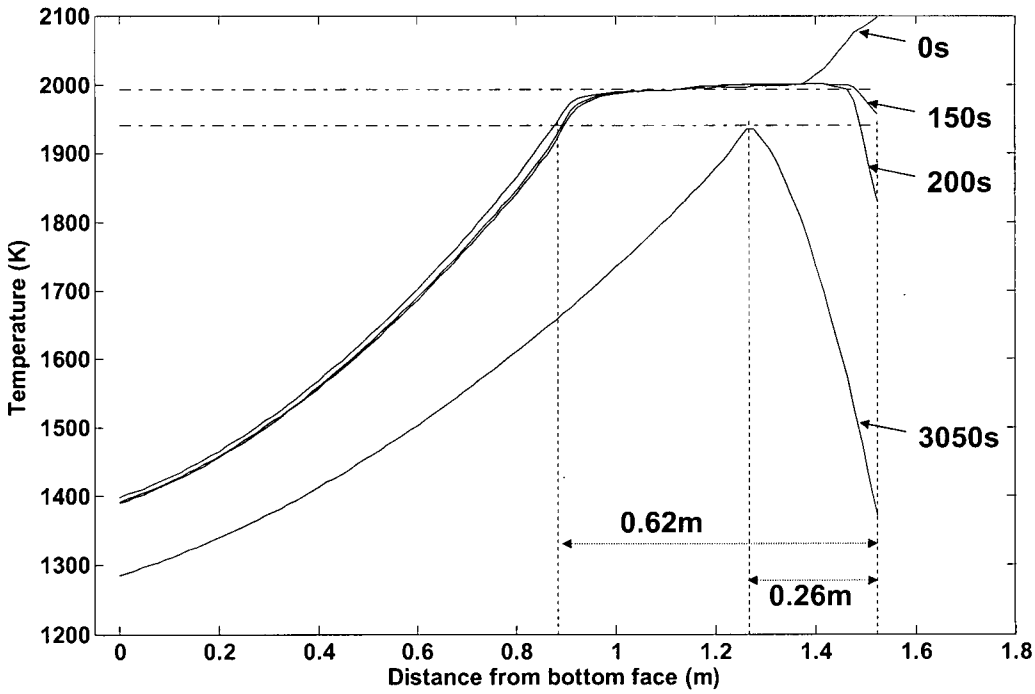

Figure 6.20 - The temperature profiles along the center line of the ingot.

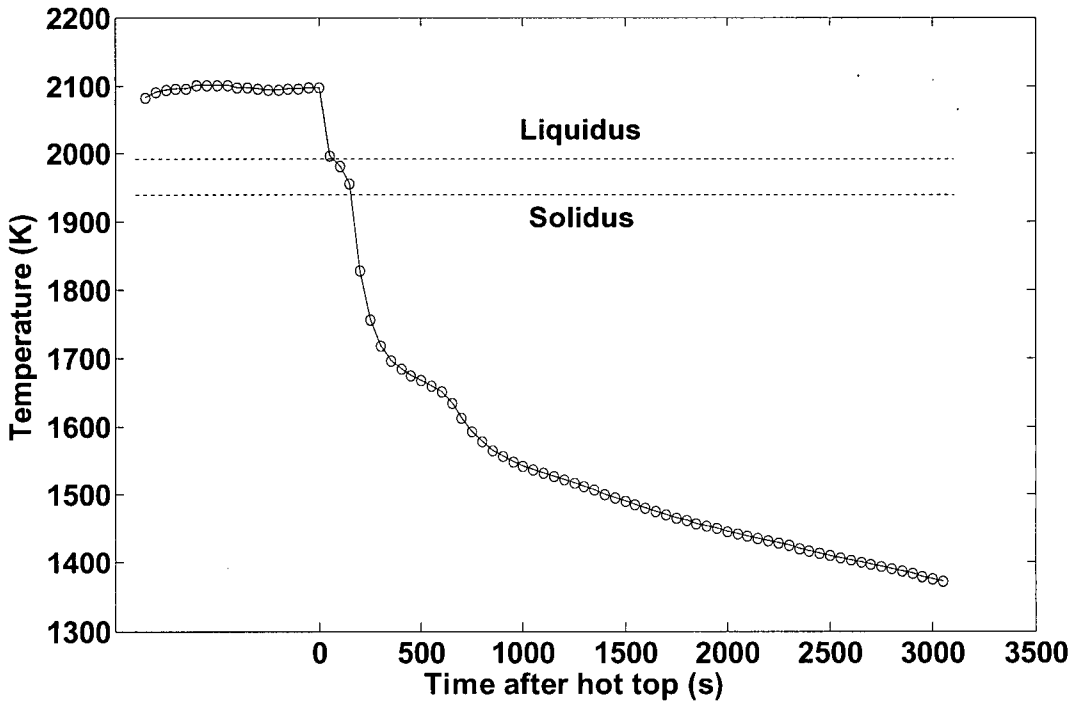

Figure 6.21 - Temperature evolution of the center point on the ingot top surface.

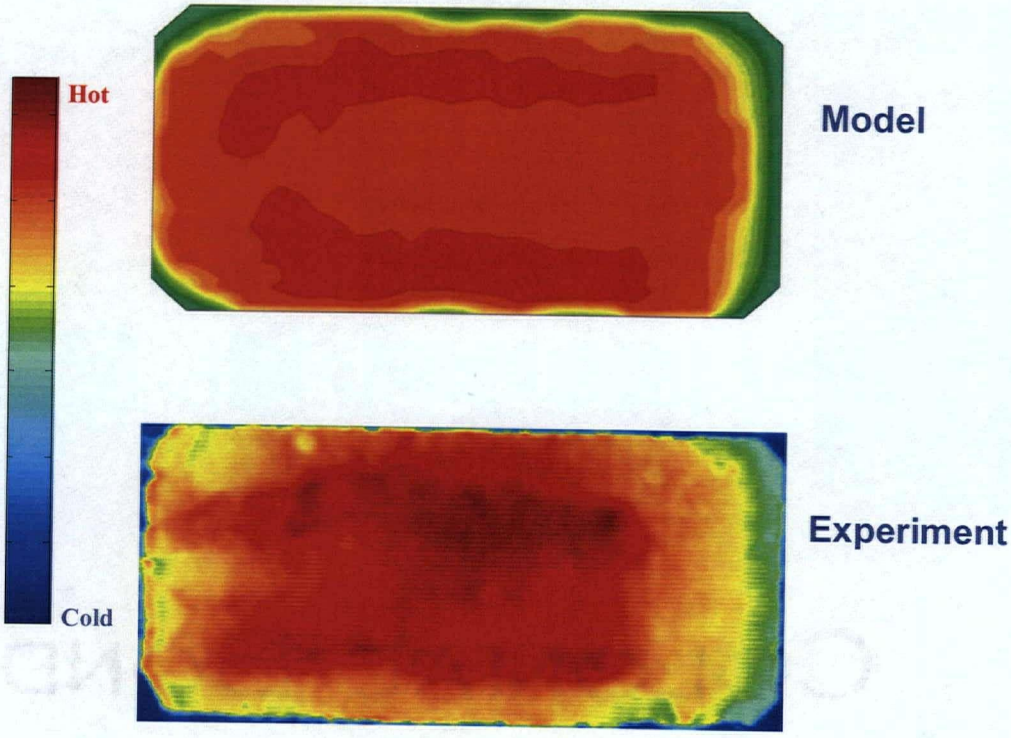

Figure 6.22 - The predicted and measured temperature distribution on the top surface of the ingot at 300s of the transient stage.

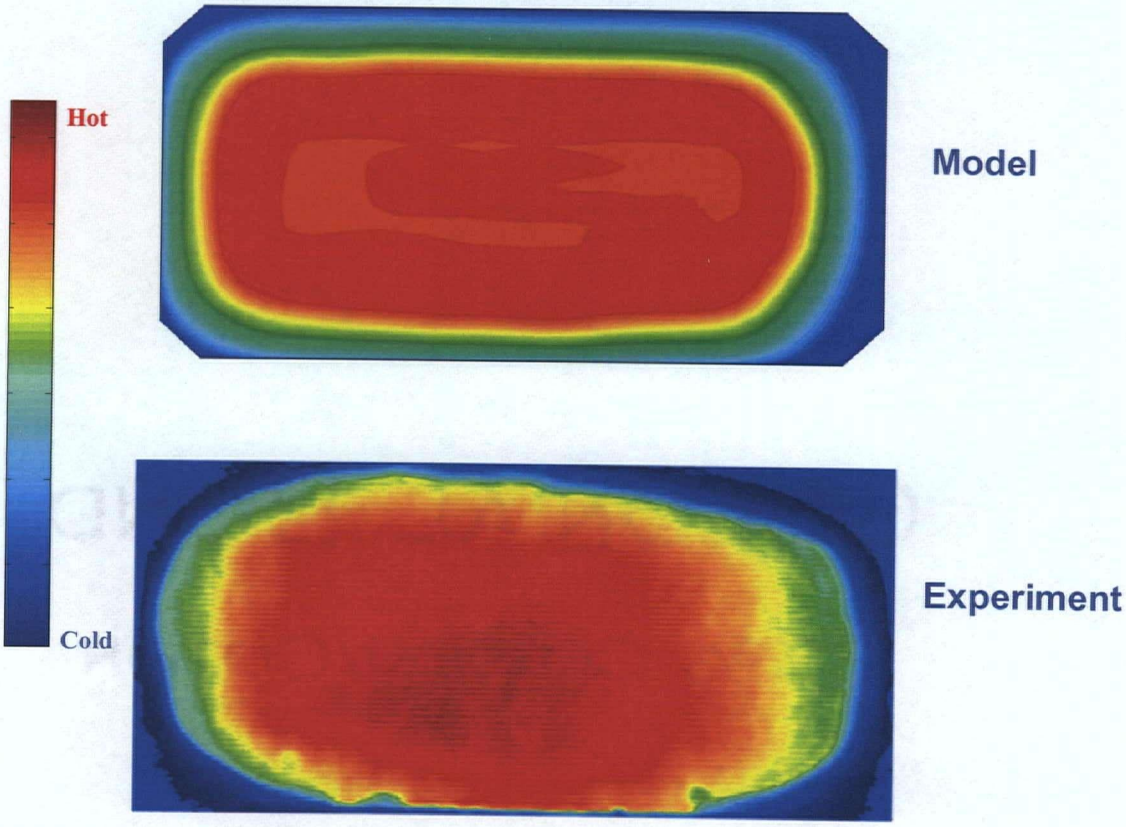

Figure 6.23 - The predicted and measured temperature distribution on the top surface of the ingot at 900s of the transient stage.

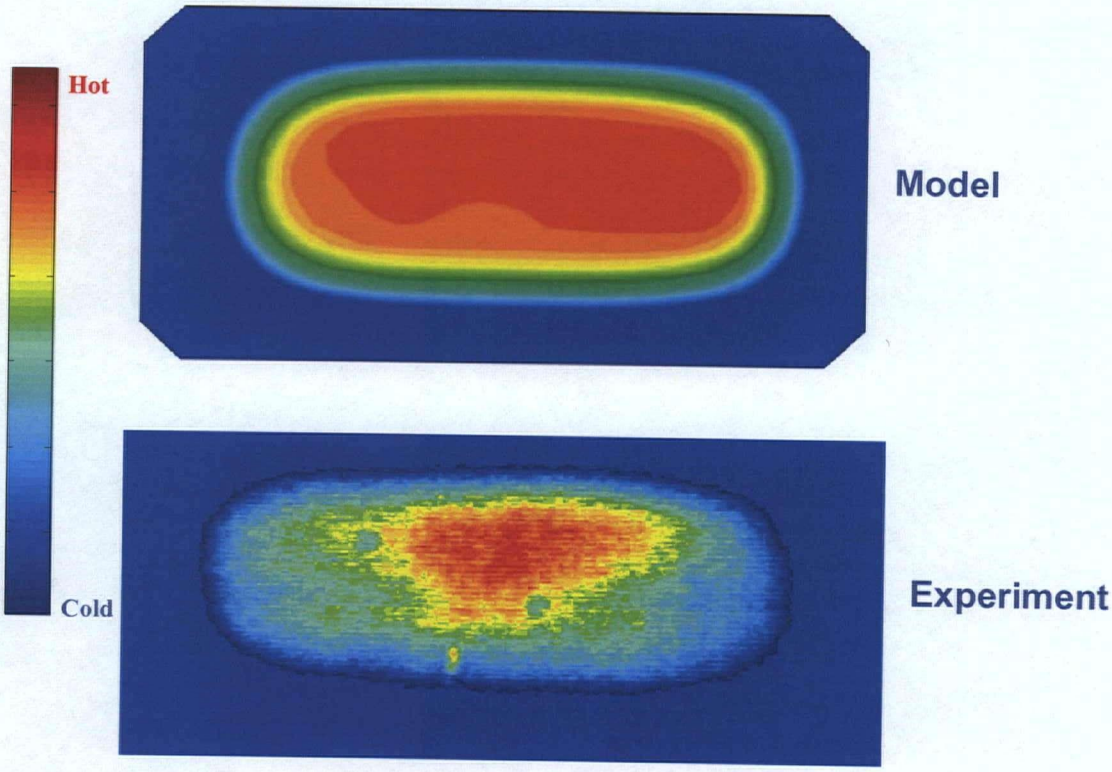

Figure 6.24 - The predicted and measured temperature distribution on the top surface of the ingot at 1800s of the transient stage.

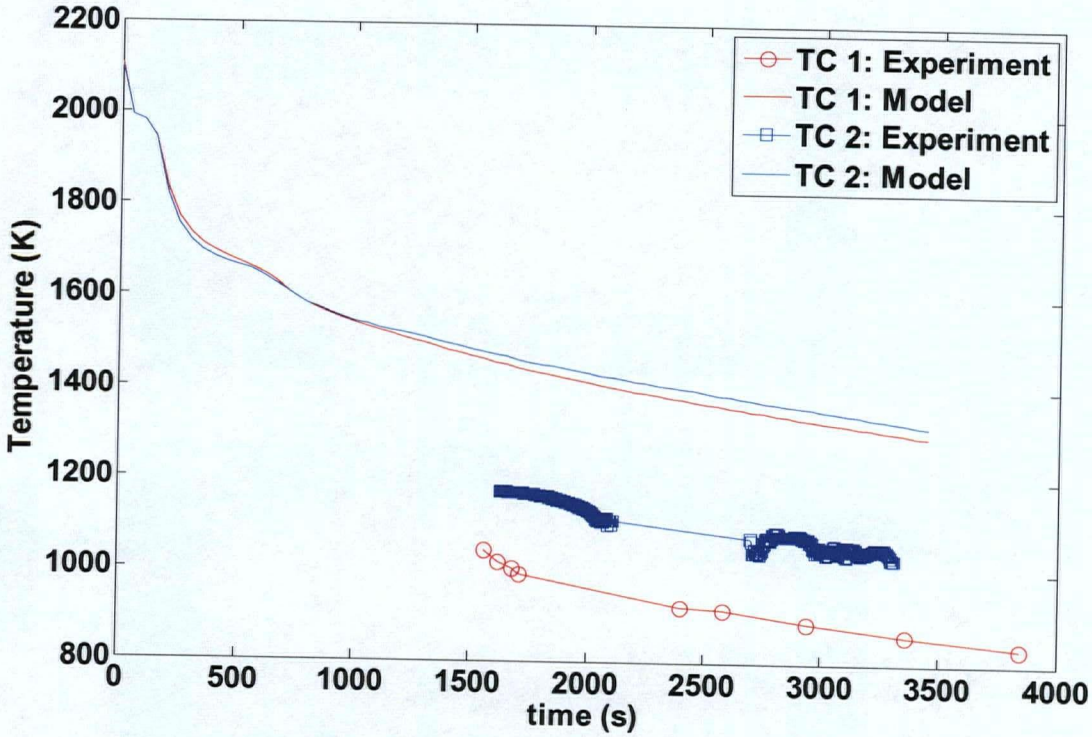

Figure 6.25 - The measured and calculated temperatures at thermocouple points on the ingot top surface during the transient stage.

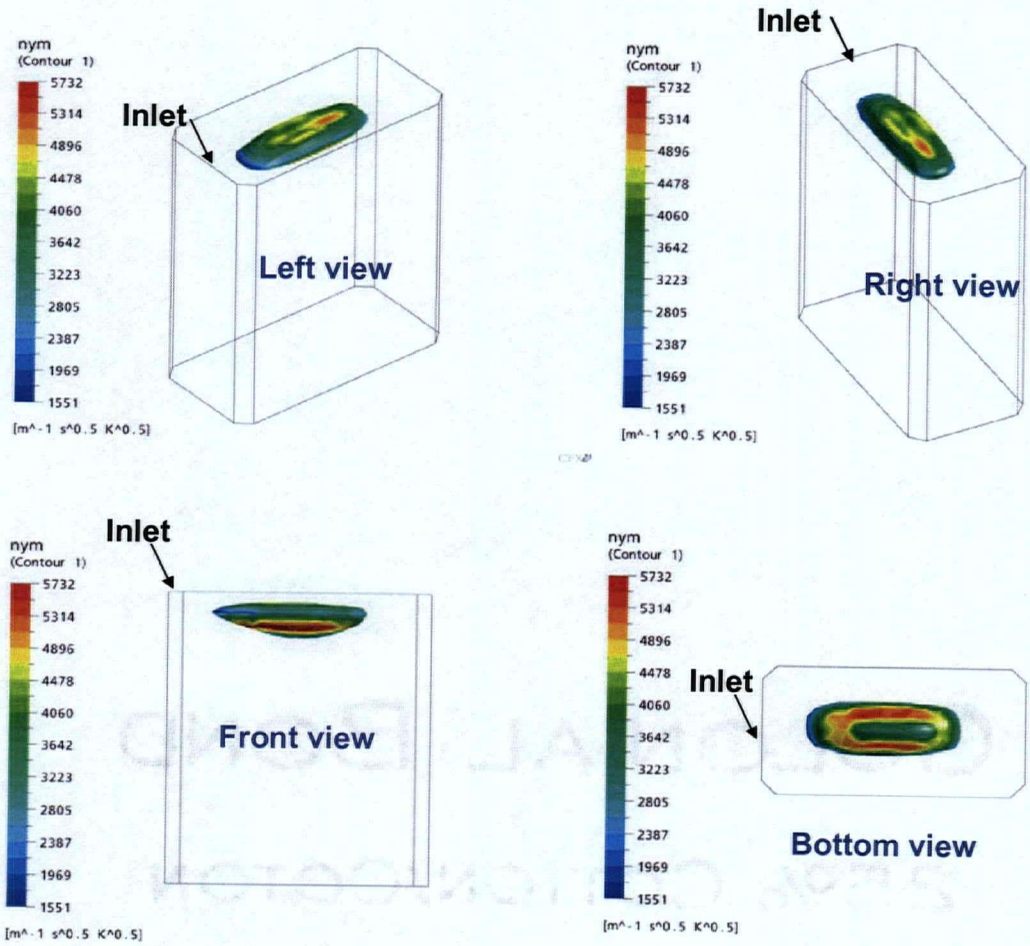

Figure 6.26 - The contours of Niyama number on the solidus isosurface at 3900s of the transient stage.

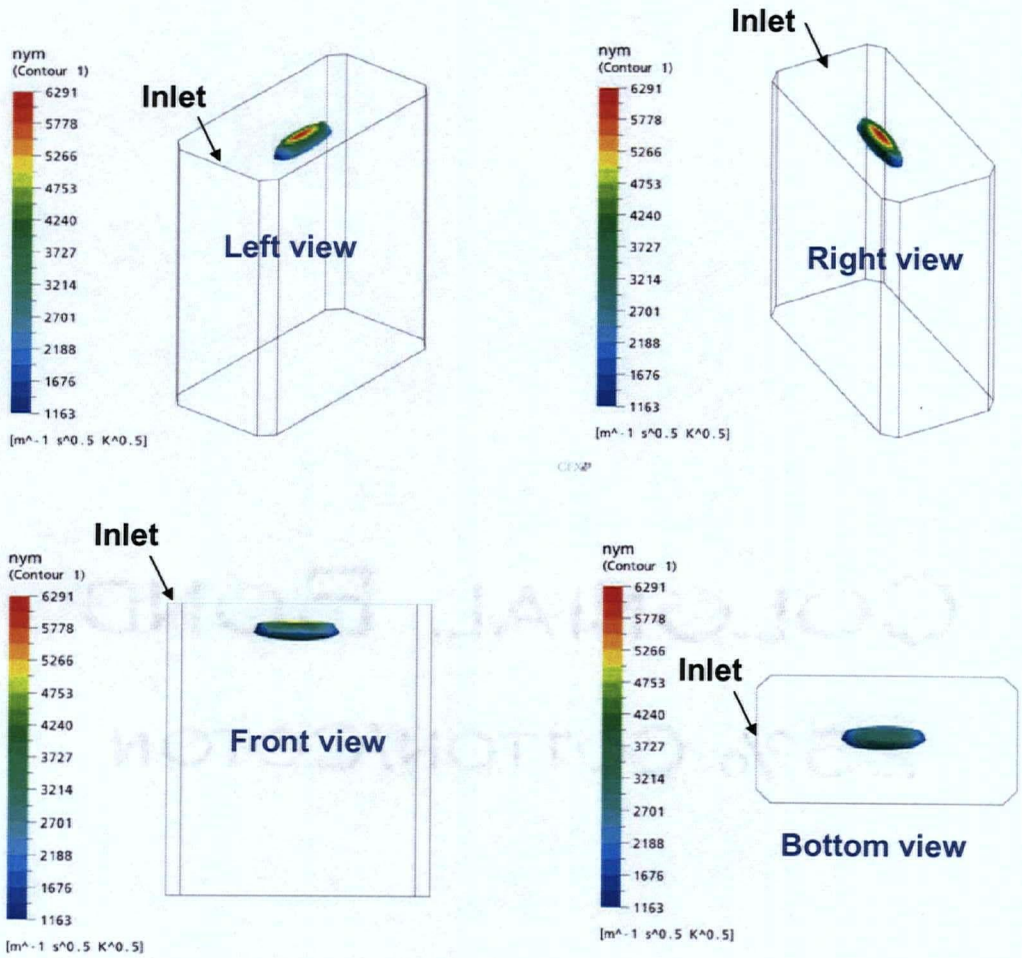

Figure 6.27 - The contours of Niyama number on the solidus isosurface at 4400s of the transient stage.

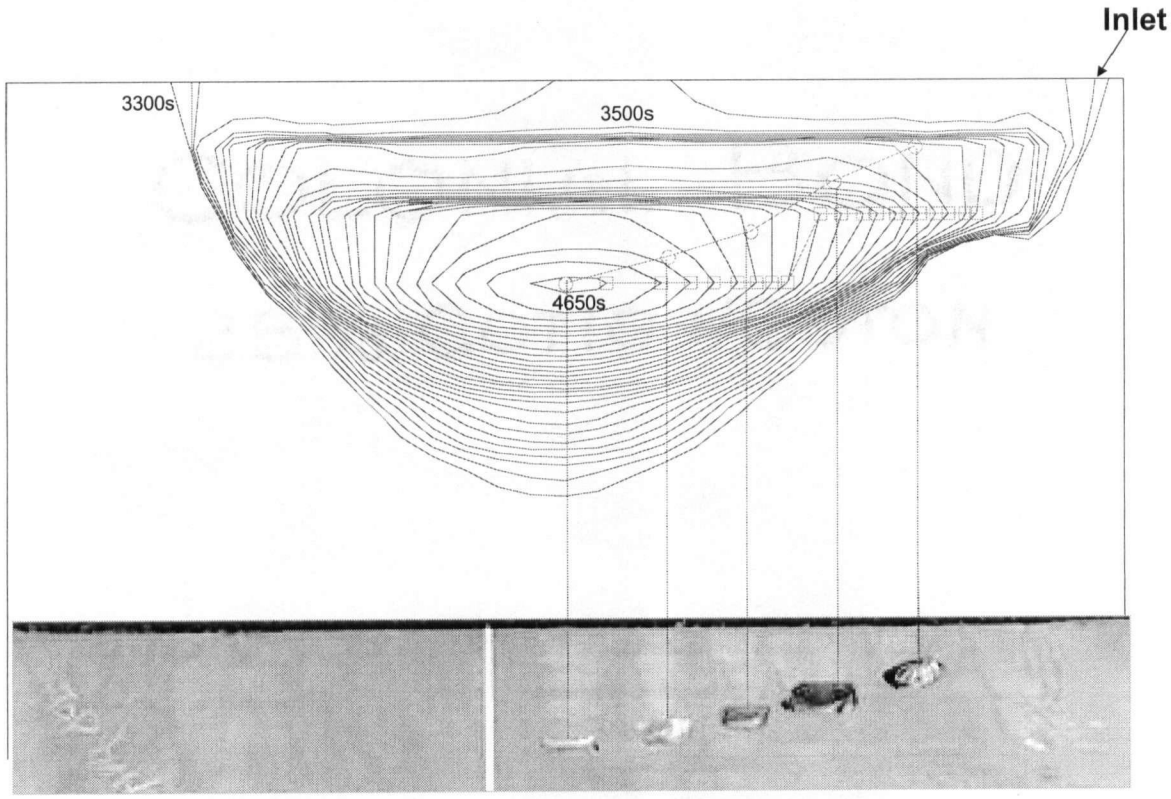

Figure 6.28 - The solidification curves from the transient-stage model and the comparison of the calculated and measured void positions.

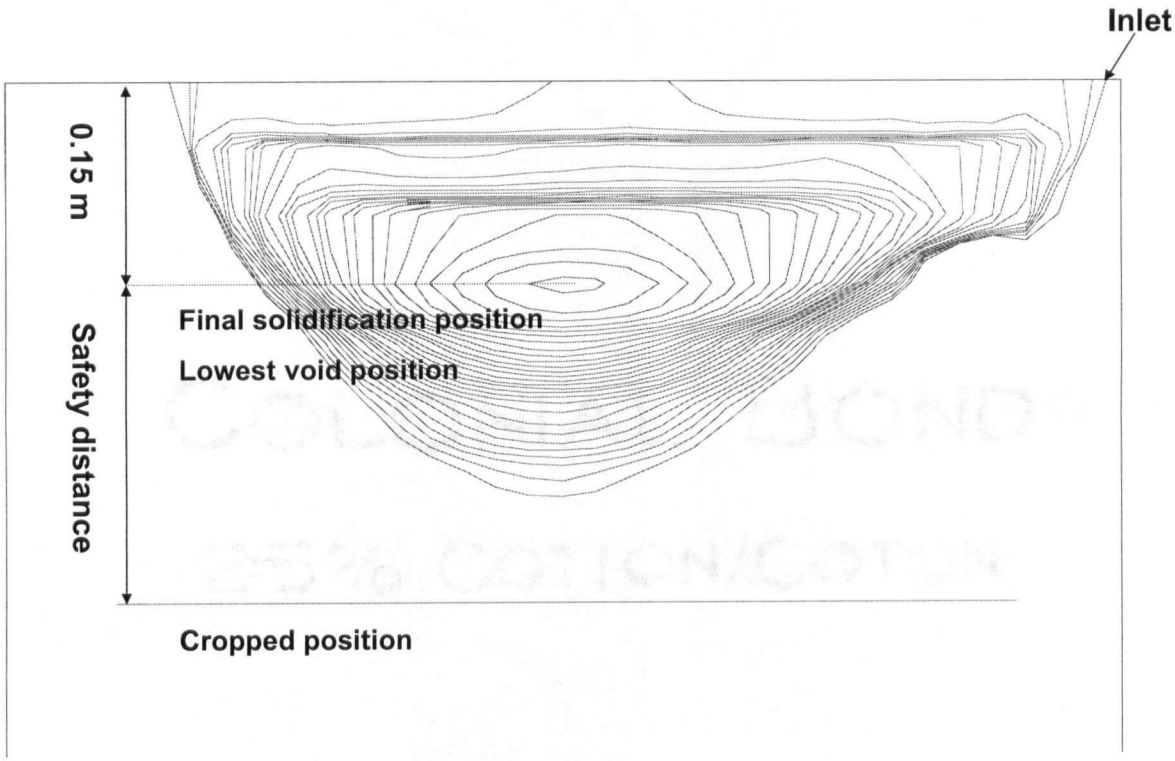

Figure 6.29 - Depth of the point of final solidification (lowest expected location of void) and the cropped position.

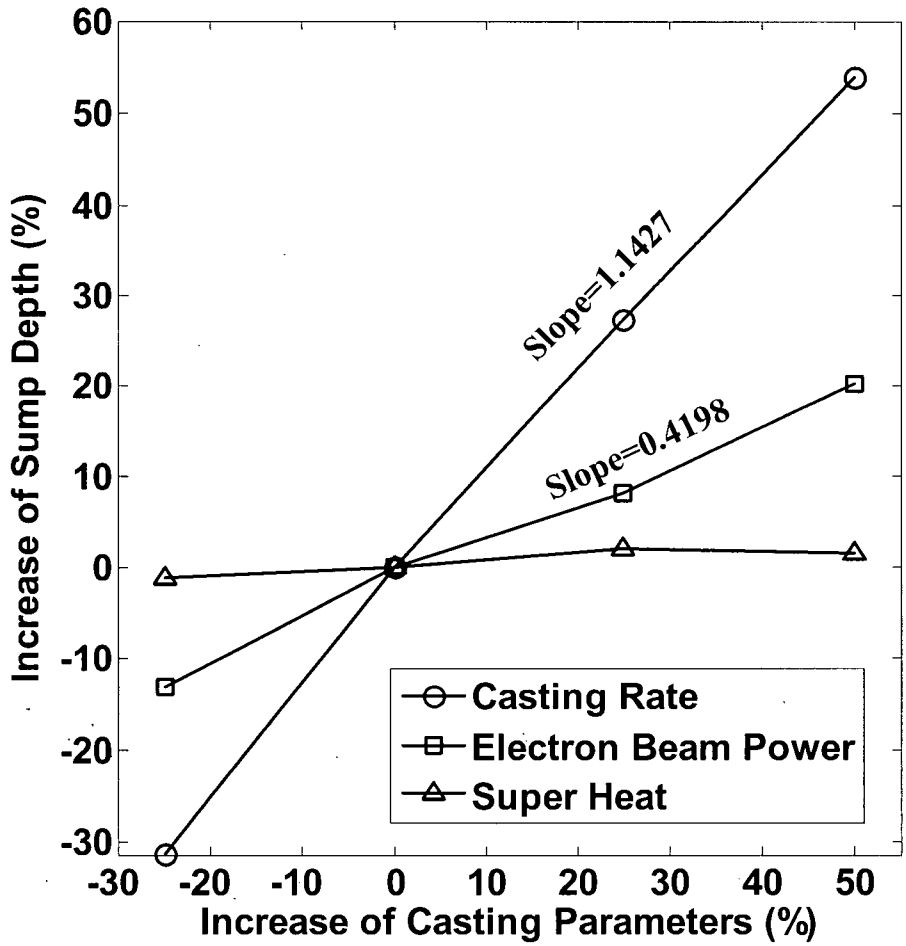

Figure 6.30 - The effect of casting parameters on the ingot sump depth.

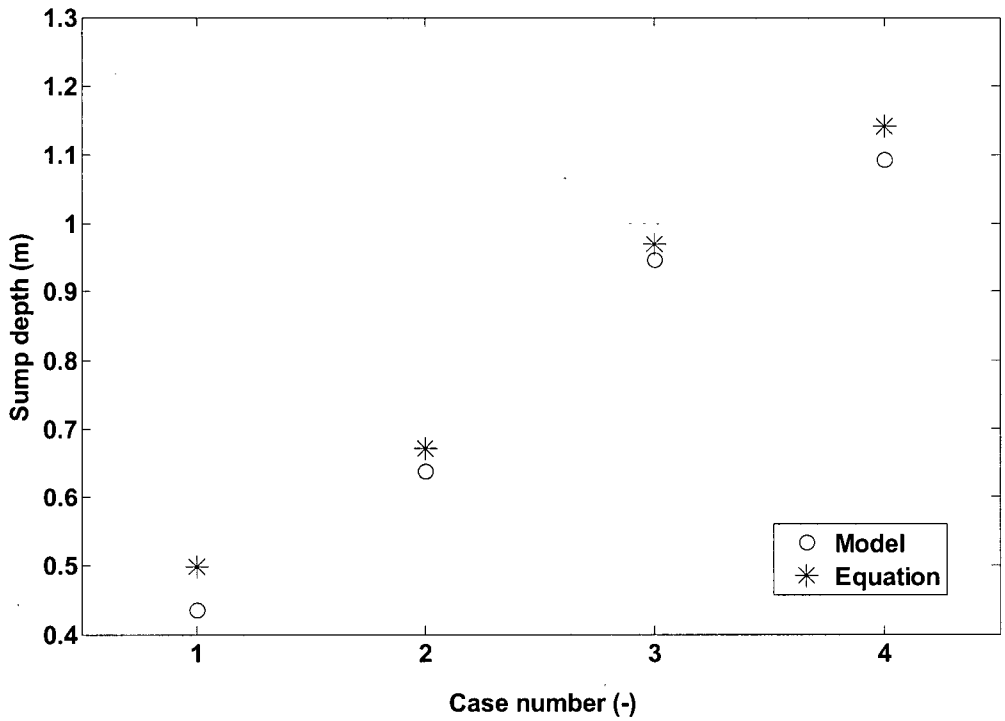

Figure 6.31 - Validation of Eq.(6.18) using models with different pairs of electron beam powers and casting rates: (1) 75% electron beam power and 75% casting rate, (2) 125% electron beam power and 75% casting rate, (3) 75% electron beam power and 125% casting rate, and (4) 125% electron beam power and 125% casting rate.

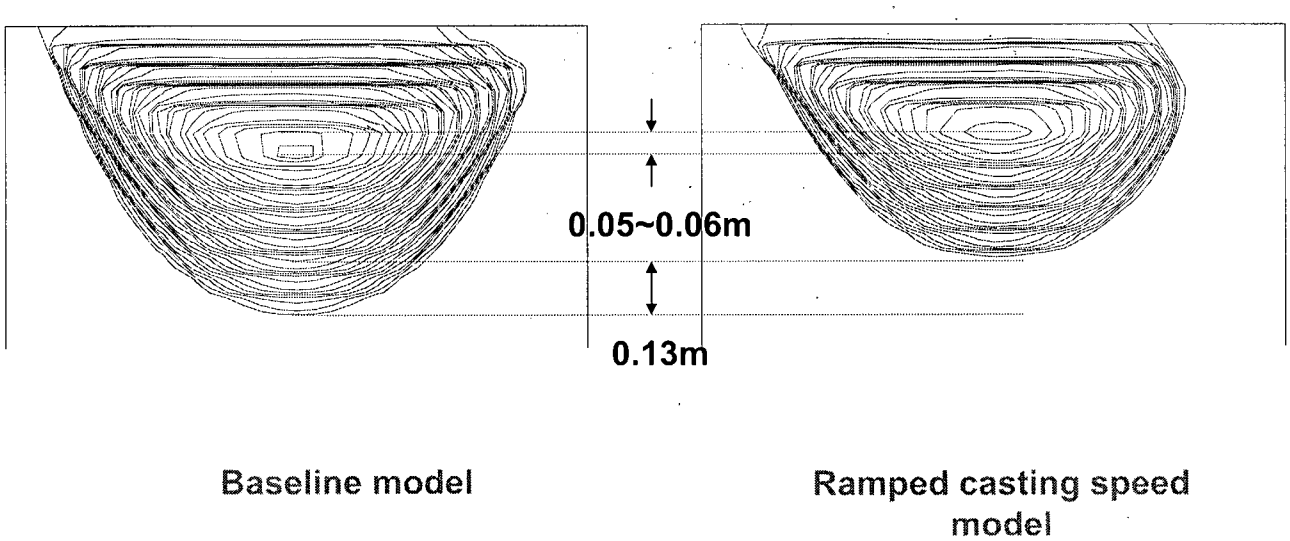

Figure 6.32 - Comparison of the solidification curves from the baseline model and the model with ramped casting speed.

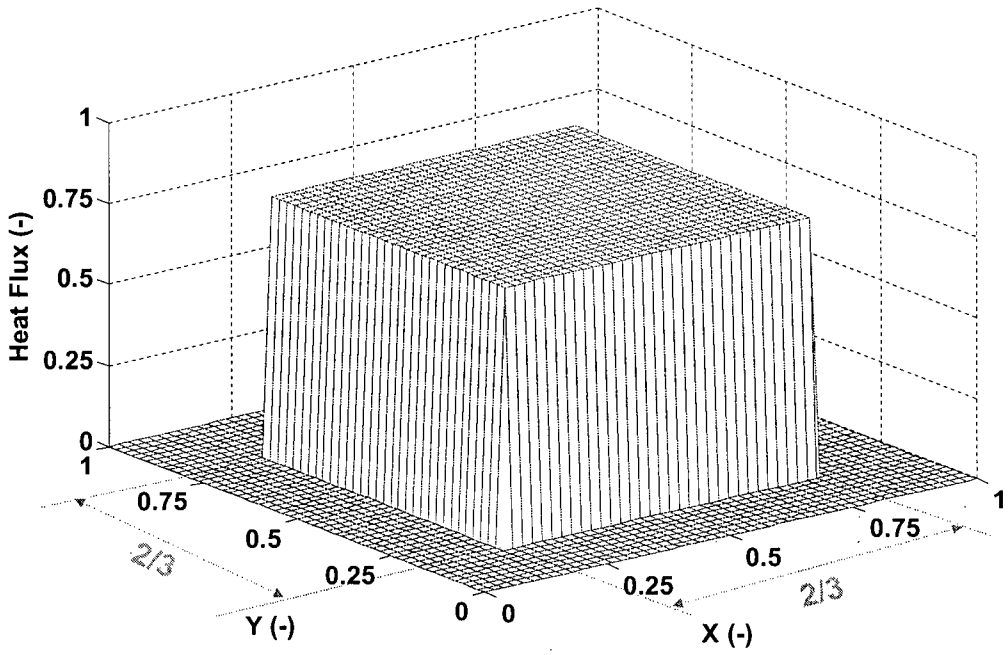

Figure 6.33 - The heat flux from electron beam applied on the transient-stage model.

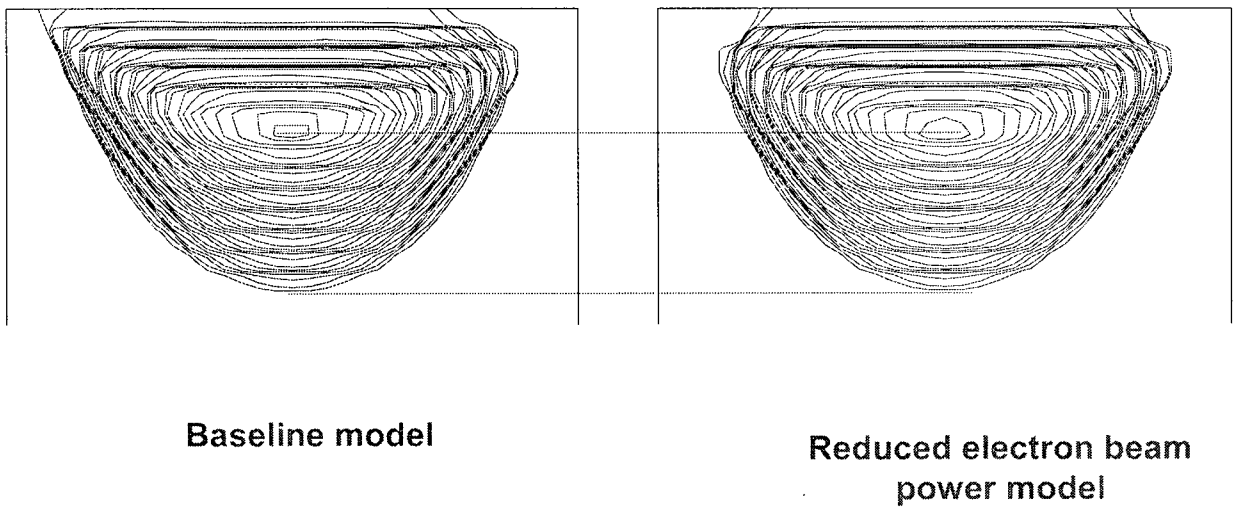

Figure 6.34 - Comparison of the solidification curves from the baseline model and the model with reduced electron beam power.

CHAPTER 7. CONCLUSIONS AND RECOMMENDATIONS

7.1. Conclusions

This research project has primarily focused on the development of a mathematical model capable of predicting the temperature distribution and flow field patterns inside a Ti-6Al-4V ingot produced during the EBCHR process. The model developed in the program is based on the commercial computational fluid dynamics (CFD) software ANSYS-CFX 10.0. The boundary conditions for the model are formulated with published data and the results from industrial measurements conducted at TIMET Corp. in Morgantown, Pennsylvania. The equations governing conservation of energy, mass and momentum have been solved in order to predict the thermal and fluid-flow fields.

During steady state of the EBCHR process, the primary energy input into the ingot is from the incoming liquid titanium, which is followed by the electron beams. On the other hand, the major energy loss from the ingot is via radiation to the roof and side walls of the EBCHR chamber, and the copper mould. The contact cooling between the ingot and the mould is insignificant, due to the very small contacting area. The energy input and output is in global balance at steady state, which proves the validity of the model. The steady-state model predicts the sump inside the ingot has a depth around 0.8m, which is very close to the value from industrial measurements. According to the model, some cold and hot regions are predicted to form on the top surface of the ingot at steady state. Similar patterns of temperature distribution are apparent in the images of the ingot top surface, taken by the near infrared camera.

During the final transient stage of the EBCHR process, the ingot becomes solidified due to the termination in liquid feeding and a reduction in the electron beam power input. The model and

industrial measurements show a similar evolution in the temperature distribution on ingot top surface during transient stage. The cooling rates from thermocouples embedded on the ingot top surface are also consistent with the model's predictions. The Niyama number has been calculated on solidus iso-surfaces of the transient-stage model, and the low Niyama number regions are deemed to be indicative of shrinkage voids. The predicted positions of shrinkage voids are approximately consistent with where the voids are found industrially. The model and experiments give the same depth of the lowest void, i.e. 0.15m. The lowest void also coincides with the final solidification point.

The casting process's sensitivity to industrial operational parameters have been evaluated by varying corresponding parameters of the model, i.e. casting rate, beam power, and superheat of inlet liquid. At steady state of EBCHR, the casting rate has the most significant effect on the ingot's sump depth, followed by the electron beam power. On the other hand, the effect of inlet superheat is negligible. In addition, the steady-state sump depth can be expressed as a linear function of the casting rate and electron beam power.

Two approaches to optimize the casting process have been evaluated for the EBCHR process: 1) ramping the casting rate to 0 during the final 1800s following the steady-state operation, and 2) reducing the area scanned by the "hot top" electron beam, while keeping the effective heat flux from electron beam at a constant level. The first approach was shown to raise the last point in the ingot to solidify. The second approach, although ineffective in void control, was found effective in reducing the liquid surface area during the "hot top" and therefore may be effective in minimizing evaporation losses.

7.2. Recommendations for Future Work

Further industrial measurements with more thermocouples embedded inside the mould and on the roof and side walls of the EBCHR chamber are desired, in order to more accurately formulate the boundary conditions.

The Niyama number as a criterion for the prediction of shrinkage voids can only give the voids' positions, but not their shapes or sizes. New criteria may be proposed for a more accurate and detailed description of the void formation.

One of the major challenges to the EBCHR process is the evaporation of alloy elements. The evaporation loss may be included in the model, in order to give a better understand of the control of the ingot's chemical composition.

The effects of more casting parameters on the EBCHR process can be studied, such as the scanning frequency of the electron beam, and the flow rate of water inside the copper mould.

The current optimization methods for the EBCHR process are supposed to be validated via industrial plant trials. In addition, based on the possible improvements of the model, more efficient strategies for optimization of the EBCHR process may be proposed.

REFERENCES

1. C. Leyens and M. Peters, *Titanium and Titanium Alloys*. 2003, Darmstadt: Wiley-VCH.
2. G. Lutjering and J.C. Williams, *Titanium*. 2003, New York: Springer.
3. J. M. J. Donachie, *Titanium: A Technical Guide*. 2nd ed. 2000, Materials Park: ASM International.
4. D.W. Tripp, *Modeling Power Transfer in Electron Beam Heating of Cylinders*, in *Metals and Materials Engineering*. 1994, The University of British Columbia: Vancouver.
5. J.P. Bellot, E. Hess, and D. Ablitzer, *Aluminum Volatilization and Inclusion Removal in the Electron Beam Cold Hearth Melting of Ti Alloys*. Metallurgical and Materials Transactions B, 2000. **31B**: p. 845-853.
6. K.C. Mills, *Recommended values of thermophysical properties for selected commercial alloys*. 2002, Materials Park: Woodhead Publishing Ltd and ASM International.
7. A.B. Lesnoj and V.F. Demchenko, *Modeling of hydrodynamics and mass exchange in electron beam remelting of titanium alloys*. Electron Beam Processes, 2003. **3**: p. 17-21.
8. C.H. Entrekin. *Removal of high density inclusions by the hearth refining process*. in *Proceedings of the Conference on Electron Beam Melting and Refining - State of the Art 1985: Part One*. 1985. Reno, NV, USA: Bakish Materials Corp.
9. C.H. Entrekin and D.S. Clarkson, *EB refining promises super clean metal production*. Metal Progress, 1986. **129**(7): p. 35-39.
10. J. Herbertson and R. Harris. *Inclusion removal by eb hearth refining*. in *Proceedings of the Conference on Electron Beam Melting and Refining - State of the Art 1985: Part Two*. 1985. Reno, NV, USA: Bakish Materials Corp.
11. R.N. Jarrett. *Removal of defects from titanium alloys with electron beam cold hearth refining*. in *Proceedings of the Conference on Electron Beam Melting and Refining - State of the Art 1986*. 1986. Reno, NV, USA: Bakish Materials Corp.
12. A. Mitchell. *Clean melting and the removal of defects from aero-engine materials*. in *Simultaneous Convening of the 3rd International SAMPE Metals Conference and the 24th International SAMPE Technical Conference. Part 2*. 1992. Toronto, Ont, Can SAMPE.
13. A. Mitchell, *Elimination of random defects in aerospace materials*. Chinese Journal of Lasers, 1999. **26**(7): p. 283-296.
14. T. Isawa, H. Nakamura, and K. Murakami, *Aluminum evaporation from titanium alloys in EB hearth melting process*. ISIJ International, 1992. **32**(5): p. 607-615.
15. A. Mitchell and K. Takagi. in *Vacuum Metallurgy Conference*. 1984: the Iron and Steel Society.
16. D. Tripp and A. Mitchell. *Thermal regime in an EB hearth*. in *Proceedings of the Conference on Electron Beam Melting and Refining - State of the Art 1985: Part Two*. 1985. Reno, NV, USA: Bakish Materials Corp.
17. H. Nakamura and A. Mitchell, *Effect of beam oscillation rate on Al evaporation from a Ti-6Al-4V alloy in the electron beam melting process*. ISIJ International, 1992. **32**(5): p. 583-592.
18. M.T. Ritchie, *EDX investigation of evaporative losses during the EB melting of SS316*, in *Metals and Materials Engineering*. 1997, The University of British Columbia: Vancouver.
19. M. Ritchie, et al., *X-Ray-Based Measurement of Composition during Electron Beam Melting of AISI 316 Stainless Steel: Part I. Experimental Setup and Processing of Spectra*. Metallurgical and Materials Transactions A, 2003. **34A**: p. 851-861.
20. M. Ritchie, et al., *X-Ray-Based Measurement of Composition during Electron Beam Melting of AISI 316 Stainless Steel: Part II. Evaporative Processes and Simulation*. Metallurgical and Materials Transactions A, 2003. **34A**: p. 863-877.

21. I. Langmuir, Physical Review, 1913. **5**: p. 329-342.
22. A. Powell, et al., *Analysis of multicomponent evaporation in electron beam melting and refining of titanium alloys.* Metallurgical and Materials Transactions B: Process Metallurgy and Materials Processing Science, 1997. **28**(6): p. 1227-1234.
23. S. Cockcroft, A. Mitchell, and D. Tripp. *Evaporation in the EBCHM process.* in *Proceedings of the Conference on Electron Beam Melting and Refining - State of the Art 1992.* 1992. Reno, NV, USA: Bakish Materials Corp.
24. S. Fukumoto, et al., *Composition control of refractory and reactive metals in electron beam melting.* ISIJ International, 1992. **32**(5): p. 664-672.
25. M. Ritchie and A. Mitchell. in *Proceedings of the Conference on Electron Beam Melting and Refining - State of the Art 1996.* 1996. Reno, NV, USA: Bakish Materials Corp.
26. V.G. Ivanchenko, O.M. Ivasishin, and S.L. Semiatin, *Evaluation of Evaporation Losses during Electron-Beam Melting of Ti-Ai-V Alloys.* Metallurgical and Materials Transactions B, 2003. **34**(4): p. 911-915.
27. S.V. Akhonin, et al., *Mathematical Modeling of Aluminum Evaporation During Electron-Beam Cold-Hearth Melting of Ti-6Al-4V Ingots.* Metallurgical and Materials Transactions B, 2002. **34B**: p. 447-454.
28. S.L. Semiatin, et al., *Diffusion Models for Evaporation Losses during Electron-Beam Melting of Alpha/Beta-Titanium Alloys.* Metallurgical and Materials Transactions B, 2003. **35B**: p. 235-245.
29. F. Carvajal and G.E. Geiger, *Analysis of the temperature distribution and the location of the solidus, mushy, and liquidus zones for binary alloys in remelting processes.* Met Trans, 1971. **2**(8): p. 2087-2092.
30. W.B. Eisen and C. A., *Computer simulation of consumable melted slabs.* Met Trans, 1970. **1**(4): p. 849-856.
31. A. Mitchell and S. Joshi, *Thermal characteristics of the electroslag process.* Metallurgical Transactions, 1970. **4**(3): p. 631-642.
32. D.N. Pocklington and B. Patrick, *Heat flow in 3-phase ESR slab production.* Metallurgical Transactions B, 1979. **10B**(3): p. 359-366.
33. A. Jardy and D. Ablitzer, *Behavior of the liquid pool in VAR ingots.* Memoires et Etudes Scientifiques Revue de Metallurgie, 1990. **87**: p. 421-427.
34. W. Shyy, et al., *Heat transfer and convection characteristics of a superheated turbulent jet interacting with a solid object.* International Journal of Heat and Mass Transfer, 1992. **35**: p. 2837-2847.
35. B. Jahne, *Digitale Bildverarbeitung,.* 1997, Heidelberg: Springer Verlag.
36. P. Haberacker, *Praxis der Digitalen Bildverarbeitung und Mustererkennung.* 1995, München/Wien: Hanser-Verlag
37. M.C. Flemings, *Solidification Processing.* 1974, New York: McGraw-Hill.
38. J. Kozeny, *Akad Wiss Wien.* Abt IIa, 1927. **136**: p. 271.
39. S.G.R. Brown, et al., *Numerical determination of liquid flow permeabilities for equiaxed dendritic structures.* Acta Materialia, 2002. **50**: p. 1559-1569.
40. **K.-I. Ahn**, et al., *Numerical Investigation on the Heat Transfer Characteristics of a Liquid-Metal Pool subjected to a Partial Solidification Process.* Progress in Nuclear Energy, 2004. **44**(4): p. 277-304.
41. J. Goldak, A. Chakravarti, and M. Bibby, Metall. Trans. B, 1984. **15B**: p. 299-305.
42. P.S. Wei and Y.T. Chow, Metall. Trans B, 1992. **23B**: p. 81-90.
43. S. Shiller, U. Heisig, and S. Panzer, *Electron Beam Technology.* 1982, New York, NY: Wiley & Sons.
44. P.A. Kobryn and S.L. Semiatin, *Determination of Interface Heat-Transfer Coefficients for Permanent-Mold Casting of Ti-6Al-4V.* Metall. Mater. Trans. B, 2001. **23B**: p. 685-695.
45. J.B. Wiskel and S.L. Cockcroft, *Heat-flow-based analysis of surface crack formation during the start-up of*

the direct chill casting process: Part I. Development of the inverse heat-transfer model. Metallurgical and Materials Transactions B, 1996. **27**: p. 119-127.

46. J.P. Holman, *Heat Transfer*. 2002, Boston: McGraw-Hill.
47. T.C. Papanastasiou, G.C. Georgiou, and A.N. Alexandrou, *Viscous fluid flow*. 1999, New York: CRC Press.
48. E. Niyama, et al., Am. Foundrymen's Soc. Int. Cast Met. J., 1982. **7**(3): p. 52-63.